

**Synthesis and characterization of
3d-transition metals doped ZnO thin films and
nanostructures for possible spintronic applications**

Thesis submitted to
COCHIN UNIVERSITY OF SCIENCE AND TECHNOLOGY
in partial fulfillment of the requirements
for the award of the degree of
DOCTOR OF PHILOSOPHY

Arun Aravind

Department of Physics
Cochin University of Science and Technology
Cochin - 682 022, Kerala, India

October 2012

Synthesis and characterization of 3d-transition metals doped ZnO thin films and nanostructures for possible spintronic applications

Ph.D. thesis in the field of Materials Science

Author:

Arun Aravind
Nanophotonic and Optoelectronic Devices Laboratory
Department of Physics
Cochin University of Science and Technology
Cochin - 682 022, Kerala, India.
Email: aruncusat@gmail.com

Supervisor:

Dr. M. K. Jayaraj
Professor
Nanophotonic and Optoelectronic Devices Laboratory
Department of Physics
Cochin University of Science and Technology
Cochin - 682 022, Kerala, India.
Email: mkj@cusat.ac.in

Front cover: Room temperature M-H loop of $\text{Zn}_{0.97}\text{Ni}_{0.03}\text{O}$ thin film

October 2012

Dedicated to my friends and family

Dr. M. K. Jayaraj
Professor
Department of Physics
Cochin University of Science and Technology
Cochin 682 022, India.

18th October 2012

Certificate

Certified that the work presented in this thesis entitled “Synthesis and characterization of 3d-transition metals doped ZnO thin films and nanostructures for possible spintronic applications” is based on the authentic record of research carried out by Aun Aravind under my guidance in the Department of Physics, Cochin University of Science and Technology, Cochin 682 022 and has not been included in any other thesis submitted for the award of any degree.

Dr. M. K. Jayaraj
(Supervising Guide)

Phone : +91 484 2577404 extn 33 Fax: 91 484 2577595 Email: mkj@cusat.ac.in

Declaration

I hereby declare that the work presented in this thesis entitled “Synthesis and characterization of 3d-transition metals doped ZnO thin films and nanostructures for possible spintronic applications” is based on the original research work carried out by me under the supervision and guidance of Dr. M. K. Jayaraj, Professor, Department of Physics, Cochin University of Science and Technology, Cochin-682 022 and has not been included in any other thesis submitted previously for the award of any degree.

Arun Aravind

Cochin-22
18th October 2012

Acknowledgments

I take this opportunity to place on record my profound sense of indebtedness and deep appreciation to my supervising guide, Prof. M. K. Jayaraj for his personal encouragement, patronly behaviour, stimulating discussions and able guidance right from the beginning to date as a consequence of which the present study reached fruition. My gratitude to him knows no bounds.

I express my sincere thanks to Prof. B. Pradeep, Head, Department of Physics and all the former Heads of the Department - Prof. V. C. Kuriakose and Prof. Godfrey Louis - for permitting me to use the research facilities in the Department. I gratefully acknowledge the help and inspiration from S. Jayalekshmi teacher who has inspired me in both academic and personal development. I would like to thank Dr. M. J. Bushiri for his suggestions and friendly discussions. I also greatly acknowledge the help and inspiration from all the faculty members of the Department of Physics.

I express my special gratitude to Prof. T. Ramesh Babu and Prof. M. R. Anantharaman for their personal care and attention.

With pleasure, I acknowledge Dr. Ramesh Chandra, Institute Instrumentation Center, IIT Roorkee for his encouragement and valuable suggestions throughout the research carrier.

I extend my sincere thanks to Prof. G. Mohan Rao and Dr. P. S. Anil Kumar, IISc Bangalore for the XPS measurements and valuable discussions during the research period. I thank Dr. Shibu M Eappen at SAIF STIC for SEM measurements.

I am grateful to - Mukehs Kumar, Rajan Walia, Goutam, Amith Chawla and Vipin Chawla for their technical support, encouragement and the friendly ambience provided to me during the visits to IIT Roorkee.

I am thankful to all the office and library staff of the Department of Physics for the help and cooperation.

I thank Department of Science Technology (DST) and University Grant Commission (UGC) for financially supporting me during this endeavor. I acknowledge the financial support of SPIE, Council of Scientific and Industrial Research (CSIR), European Union - to attend the international conferences and Summer schools during my research work.

My time at CUSAT was made enjoyable in large part by the many friends who have become a part of my life. It is my pleasure to acknowledge the advice and love received from my senior researchers in the Opto-electronic Devices Laboratory - Aldrin chettan, Manojettan, Nisha chechi, Rahana chechi, Asha chechi, Joshy sir, Mini chechi and Vanaja Madam. I express my special gratitude to Ajimshettan, Anoopettan, Sajiетtan and Anila Teacher for the utmost love and care in the entire academic life at CUSAT. I greatly acknowledge the helping hands provided by - Aneesh, Reshmi chehci, Krishnaprasad and James Sir in every patches of the research life. Its immense joy to work with - Satish bhai, Sasankan, Sreeja, Vikas, Hasna, Subha, Majeesh, Saritha chechi, Shijeesh, Vishnu and Rakhy. The funny discussions, driving, lab renovation works, conferences, swimming etc. have all bonded us as life time friends. I wish to express my sincere regards to Anooja and Anjala for the beautiful time in the lab.

I am especially grateful to my dear friends - Sanal, Nijo Varghese, Priyesh, Vinayaraj, Arun, Rajesh C. S, Bhavya and Tharanath for their patience, encouragement and moral support at each and every stage of my PhD work.

I owe a lot to my little sister, Athira for her selfless support and encouragement from my school days onwards.

I value my friendship with Ragitha, Jijin, Reshma, Anlin, Sudakshina, Jafar, Christie, Sarathlal, Jobina, Shitha, Shonima, Aebey and Jerrin whom I got acquainted with at OED.

I really enjoyed the wonderful company, support and constant encouragement of my little friends - Monisha Lal, Arya Moosad and Linda Francis.

I would like to thank all my colleagues at the department of Physics especially Rajesh mon, Senoyettan, Subin, Vivek, Naryanan, Poornima, Angel, Anu, Navaneeth, Sajan, Sajeesh, Vimalettan, Swapna chechi, Reena chechi, Veena chechi, Geetha and all other friends in CUSAT for their great moral and financial support during my academic period. I express my sincere thanks to my school mates and M.Sc friends - Anoop, Subodh, Pradip, Kalesh, Rajesh, Deepumon, Athulya (late), Gopikrishna, Syam, Haridas, Linthish for their affection and support.

Its my proud privilege to remember my parents, brother Surun and all relatives for their selfless support, motivation, encouragement, patience and tolerance throughout.

By God's grace, with extreme pleasure, let me thank once again all my friends and well wishers for their endless support to all my endeavors.

Arun Aravind

Preface

The II-VI group of binary compound semiconductors are having wurtzite and zinc blende crystalline structures. Oxide based novel thin films of homo and hetero structures are technologically attractive because of their exciting fundamental intrinsic and extrinsic optical, electrical, magneto-optical and piezoelectric properties. Nanotechnology brings the possibility of tuning the material properties by reducing any one of the dimension of the material to nanometer range without changing the chemical composition. The transition from micron sized particles to nanoparticles lead to a number of changes in their physical properties and optical properties due to quantum confinement effects. In the class of optoelectronic materials ZnO is emerging as a potential candidate due to its direct and wide optical band gap. The electronic, magnetic and optical properties can be tailored through doping, alloying and nanoengineering. ZnO is an efficient UV emitter and the exciton binding energy (60 meV) is more than twice that of GaN (25 meV). The radiative recombination of atoms in ZnO leads to narrow emission line width. Based on these properties it is envisioned that ZnO has a role in wide range of devices such as blue and UV light emitting hetero

junction diodes, diode lasers, visible and solar blind UV detectors, optical wave guides, spintronic devices based on diluted magnetic semiconductors.

Dilute Magnetic Semiconductors (DMS) in which magnetic ions substituted for cations of the host semiconducting material are ideal system for spintronics. DMS have wide applications in spintronics due to the combined properties of the magnetic and electric properties of the dopants and the host. Novel functions can be achieved, for example, in spin-field effect transistors (spin FET) or in spin light emitting diodes (spin LED), if the injection, transfer and detection of the carrier spin can be controlled electrically or optically. A large number of research groups synthesize and characterize the ZnO and transition metals (TM) doped ZnO thin films and nanostructures by various methods but most of them achieved room temperature ferromagnetism due to impurity phases or metallic clusters.

The objective of the present study is the formation of single phase $Zn_{1-x}TM_xO$ thin films by PLD and increase the solubility limit of TM dopants. The TM doped ZnO nanostructures were also grown by hydrothermal method. The structural and morphological variation of ZnO:TM thin films and nanostructures with TM doping concentration is also investigated. The origin and enhancement of ferromagnetism in single phase $Zn_{1-x}TM_xO$ thin films and nanostructures using spectroscopic techniques were also studied. The dependence of ablation parameters on the structural and optical properties of ZnO thin films were studied.

Chapter 1 gives an introduction to semiconductors and different properties of the ZnO based dilute magnetic semiconductors. The different theoretical approaches and practical applications of some of the spintronic devices are also discussed. The basic magnetic theories in dilute magnetic

semiconductors are also discussed. A brief review of oxide nanostructures is also presented.

Chapter 2 describes in detail the techniques for the growth of thin films, nanostructures and characterization tools employed in the present work. The thin films were prepared by pulsed laser ablation (PLD) technique. The nanostructures were grown by hydrothermal method. The basic principles and specifications of the instruments used for these investigations are discussed in this chapter. X-ray diffraction (XRD) and Raman spectra were used for the structural characterization. Surface morphology of the thin films were analyzed by atomic force microscopy (AFM) in non-contact mode and the nanostructures by scanning electron microscopy (SEM). Compositional analysis has been carried out by energy dispersive x-ray (EDX) analysis and valence of the dopants were confirmed by x-ray photoelectron spectroscopy (XPS). Thickness of the films was measured using stylus profiler. Band gap of the materials were estimated from the optical transmittance for thin films and diffuse reflectance spectroscopic studies for nanostructures using UV-Vis-NIR spectrophotometer. The room temperature photoluminescence (PL) emission were recorded using the LabRAM spectrophotometer with He-Cd laser (325 nm) as the excitation source. The magnetic studies of the bulk powders, nanostructures and thin films were carried out by vibrating sample magnetometer (VSM) and superconducting quantum interference device (SQUID).

Chapter 3 describes the growth of highly c-axis oriented ZnO thin films by pulsed laser deposition (PLD) technique on quartz, p-silicon(100) and c-Al₂O₃ (0001) substrates using KrF excimer laser (λ_{ab} = 248 nm) and Q-switched fourth harmonic Nd:YAG laser (λ_{ab} =266 nm). The crystalline nature, surface morphology and optical properties of the deposited films

depends on the oxygen ambient and substrate temperature. The band gap of the ZnO thin films increase with increase of substrate temperature. The strong UV photoluminescent emission without visible defect emission confirms the formation of highly stoichiometric and crystalline thin films.

The chapter 4 is divided into two sections, the first part describes the growth of Co and Mn doped ZnO thin films and second part deals with the growth of Ni and Cu doped ZnO thin films by PLD. The band gap of the $Zn_{1-x}Co_xO$ and $Zn_{1-x}Mn_xO$ thin film is blue shifted with increase of Co and Mn doping. But in the case of $Zn_{1-x}Ni_xO$ and $Zn_{1-x}Cu_xO$ thin films the band gap is red shifted with increase of Ni and Cu concentration. The phase purity and crystal structure were confirmed by x-ray diffraction studies. The surface morphology characterized by atomic force microscopy shows that ZnO:TM thin films have uniformly distributed smaller grains. The nature of the grains and its size changes at higher doping percentages. The broadening of absorption edge suggests an increase in the disorder in TM doped ZnO film with incorporation of transition metals. XPS spectra confirms the incorporation of TM^{2+} into the ZnO lattice. Room temperature ferromagnetism is observed at lower TM doping percentages without any secondary phases. The maximum coercivity of the $Zn_{0.97}Mn_{0.03}O$, $Zn_{0.95}Co_{0.05}O$, $Zn_{0.97}Ni_{0.03}O$ and $Zn_{0.97}Cu_{0.03}O$ thin films are 150 Oe, 440 Oe, 640 Oe and 190 Oe respectively. The saturation magnetization of $Zn_{1-x}TM_xO$ decreases with increase of TM doping due to secondary phase formation and the increased antiferromagnetic interaction between the TM dopants. Single phase $Zn_{1-x}TM_xO$ thin films were grown by PLD and the structural variation with doping concentration is also monitored.

Chapter 5 describes growth of ZnO and TM doped ZnO nanostructures for optoelectronic and possible spintronic applications. The dependance

on temperature, time of growth and precursor concentration on the structure, morphology, optical properties of ZnO:TM nanostructures were investigated in detail. These nanostructures were characterized by XRD and SEM. The electron paramagnetic resonance confirms the incorporation of TM²⁺ in the ZnO lattice. The magnetic properties investigated by VSM measurements shows room temperature ferromagnetism in TM doped ZnO nanostructures. The coercivity of the ZnO:TM nanostructures decreases with increase of TM doping due to possible formation of secondary phases. The room temperature hysteresis is not saturated at lower applied field indicating the traces of paramagnetic components in the nanostructures. The photoluminescent emission shows that TM doped ZnO nanostructures have visible defect emission. So the combined magnetic and photoluminescent properties have wide applications in the field of spintronics.

Chapter 6 summarizes the major contributions of the present investigations and recommends the scope for future works.

Part of the work presented in the thesis has been published in various journals

Journal Papers

1. Magnetic properties of Mn and Ni doped ZnO nanostructures grown by hydrothermal method, **Arun Aravind** and M. K. Jayaraj (Submitted to Journal of Physics D: Applied Physics)
2. Optical and magnetic properties of Zn_{1-x}Co_xO thin films grown by pulsed laser deposition, **Arun Aravind**, K. Hasna, M. K. Jayaraj, Mukesh Kumar and Ramesh Chandra, (Under review - Applied Surface Science)

3. Optical and magnetic properties of Copper doped ZnO nanorods prepared by hydrothermal method, **Arun Aravind**, M. K. Jayaraj, Mukesh Kumar and Ramesh Chandra, Journal of Material Science Materials in Electronics (DOI: 10.1007/s10854-012-0911-6)
4. Optical properties of Cu doped ZnO thin films grown by of pulsed laser deposition, **Arun Aravind** and M. K. Jayaraj, Phys. Express **3**, 7 (2013)
5. Structural, Optical and Magnetic Properties of Highly Oriented Transition Metal (Mn/Co/Ni/Cu) Doped ZnO Thin Films Prepared by PLD, **Arun Aravind**, M. K. Jayaraj, Mukesh Kumar and Ramesh Chandra, MRS Proceedings (DOI: 10.1557/opl.2012.1243)
6. Structural, Optical and Magnetic properties of Mn doped ZnO thin films prepared by of pulsed laser deposition, **Arun Aravind**, M. K. Jayaraj, Mukesh Kumar and Ramesh Chandra, Materials Science and Engineering B **177**, 1017 (2012)
7. Defect induced Raman active modes in Mn doped ZnO thin films, **Arun Aravind**, K. Hasna and M. K. Jayaraj, Proc. of SPIE **8100**, 81001L-1 (2011)

Conference Papers

1. The dependence of the structural and optical properties of PLD grown ZnO films on the ablation wavelength, **Arun Aravind**, Mukesh Kumar, Ramesh Chandra and M. K. Jayaraj, ICMAT 2011, Suntec, Singapore.

2. Linear and nonlinear optical properties of pulsed laser deposited $Zn_{1-x}Mn_xO$ thin films, R. Sreeja, **Arun Aravind**, E. K. Ragitha and M. K. Jayaraj, International Conference on Electroceramics (ICE-2009), Delhi, India.
3. ZnO based dilute magnetic semiconductors for Spintronics, **Arun Aravind**, P. M. Aneesh and M. K. Jayaraj, National Seminar on Recent Advances in Nano Science & Technology (NS NANO 2009), S N College, Kollam, India.
4. Structural and optical characterization of $Zn_{1-x}Co_xO$ thin films grown by pulsed laser deposition, **Arun Aravind**, K. Hasna and M. K. Jayaraj, DAE-BRNS 5th National Symposium on Pulsed Laser Deposition of Thin Films and Nanostructured Materials (PLD 2009), Chennai, India.
5. Structural and electrical characterization of $Zn_{1-x}Mn_xO$ thin films grown by pulsed laser deposition, **Arun Aravind**, E. K. Ragitha, P. S. Krishnaprasad and M. K. Jayaraj, International Seminar on Mathematical & Experimental Physics - 2008, PSGRK College, Coimbatore, India.

Other publication to which author has contributed

Journal Papers

1. Dependence of Size of Liquid Phase Pulsed Laser Ablated ZnO Nanoparticles on pH of the Medium, P. M. Aneesh, **Arun Aravind**, R. Reshmi, R. S. Ajimsha and M. K. Jayaraj, Transactions of Materials Research Society of Japan, **34**, 759 (2009)

2. Size dependent optical nonlinearity of Au nanocrystals, R. Sreeja, P. M. Aneesh, **Arun Aravind**, R. Reshmi, Reji Philip and M. K. Jayaraj, Journal of Electrochemical Society, **156(10)**, K167 (2009)
3. Luminescence from surfactant free ZnO quantum dots prepared by laser ablation in liquids, R. S. Ajimsha, G. Anoop, **Arun Aravind** and M. K. Jayaraj, Electrochemical and Solid State Letters, **11(2)**, K14 (2008)
4. Photoluminescence of SrS:Cu nanophosphor, E. I. Anila, **Arun Aravind** and M. K. Jayaraj, Nanotechnology **19**, 145604 (2008)

Conference Papers

1. Structural and Optical characterizations of ZnO and TiO₂ nanotubes, M. K. Jayaraj, P. P. Subha, L. S. Vikas, K. Hasna, P. M. Aneesh, **Arun Aravind**, K. Rajeev Kumar, K. N. Madhusoodanan and S. Jayalekshmi, National Review and Co-ordination Meeting 2011-DST, IIT Delhi, India.
2. Optical properties of ZnO and metal nanostructures, M. K. Jayaraj, P. M. Aneesh, R. Sreeja, **Arun Aravind**, R. Reshmi, K. Rajeev Kumar and S. Jayalekshmi, National Review and Co-ordination Meeting 2011-DST, IIT Delhi, India.
3. Growth of various nanostructures of ZnO by LP-PLA and hydrothermal method, P.M. Aneesh, **Arun Aravind** and M. K. Jayaraj, DAE-BRNS 5th National Symposium on Pulsed Laser Deposition of Thin Films and Nanostructured Materials (PLD 2009), Chennai, India.

4. SrS:Cu Nanophosphors for flat panel displays, **Arun Aravind**, E. I. Anila and M. K. Jayaraj, National Review and Co-ordination Meeting 2009-DST, SNBNCBS, Kolkata, India.
5. Synthesis of gold nanoparticles by laser ablation in liquid media, P. M. Aneesh, **Arun Aravind**, R. Sreeja, R. Reshmi and M. K. Jayaraj, Second International Conference on Frontiers in Nanoscience and Technology (Cochin Nano-2009), Kochi, India.
6. Gold nanoparticles by liquid phase pulsed laser ablation for biological and optical limiting applications, P. M. Aneesh, R. Sreeja, **Arun Aravind**, R. Reshmi and M. K. Jayaraj, 2nd International conference Bangalore Nano-08, Bangalore, India.
7. Various nanostructures of ZnO grown by LP-PLA and chemical methods, P. M. Aneesh, **Arun Aravind**, R. Reshmi and M. K. Jayaraj, 2nd International conference Bangalore Nano-08, Bangalore, India.
8. Size dependent optical absorptive nonlinearity of Au nano clusters in water, P. M. Aneesh, R. Sreeja, **Arun Aravind**, R. Reshmi, M. K. Jayaraj, Photonics 2008, Delhi, India.
9. Copper Doped Strontium Sulphide Nanoparticles for Display Applications, **Arun Aravind**, E. I. Anila and M. K. Jayaraj, Third Marie Curie Summer School on Partial Melt and Amorphous Solids-2007, Estremoz, Portugal.
10. Synthesis and optical characterization of copper doped SrS nano phosphor E. I. Anila, **Arun Aravind** and M. K. Jayaraj, NCSE 2007, Kottayam, Kerala, India.

11. Preparation and characterization of SrS:Cu,Cl nanophosphor, E. I. Anila, **Arun Aravind** and M. K. Jayaraj, MATCON 2007, Cochin, India.

Chapter 1

Introduction to dilute magnetic semiconductors

1.1 Introduction

Semiconductors played, and continue to play, an undeniably pivotal role in the explosive growth of our technical civilization over the last six decades. It is no secret that silicon devices dominate the semiconductor industry. But during the last decade the paradigm has shifted noticeably. The compound semiconductors composed of III-V and II-VI groups offers many of the desired properties for applications like optoelectronics, photovoltaics, spintronics etc and could be synthesized without much difficulty [1–6]. Among these compound semiconductors, GaN and ZnO have got attention of many researchers due to their outstanding properties. The band gap energy of GaN and ZnO are nearly the same (about 3.5 eV).

The III-V compounds such as GaN, GaAs, GaP, GaAsP, GaInP have increased demand in the field of red and green/yellow light emitting diodes.

Maruska *et al.* [7] prepared single crystals of GaN ($E_g = 3.39$ eV) by hydride vapor phase epitaxy (HVPE). Later Pankove *et al.* fabricated MIS-type blue LEDs [8]. These reports triggered a sudden increase in research on blue light emitting devices. The surface of GaN crystals was very rough with cracks and pits and p-type GaN was impossible to produce. The ZnSe has a direct band gap of 2.7 eV and shows bright CL and PL emission. In addition, lattice constant of ZnSe is similar to GaAs thus enabling epitaxial growth on GaAs substrates. The melting point and vapor pressure of GaN are much higher than that of ZnSe, making the crystal growth of GaN extremely difficult. So the research groups moved on to other materials such as ZnSe, which is II-VI compound and activities on nitride declined. Recently ZnO gained considerable interest than GaN and is a promising material for ultraviolet (UV) and blue light emitting diodes (LEDs) and laser diodes. The possibility of p-type doping of ZnO renewed interest in this material for applications in UV light emitters, transparent electronics, chemical and gas sensing, channel layers for thin film transistors and spintronics [2–6].

Oxide based novel thin films of homo and hetero structures are technologically attractive for future optoelectronic devices because of their exciting fundamental intrinsic and extrinsic optical, electrical, magneto optical and piezo electric properties [1–3]. In the class of optoelectronic materials ZnO is emerging as a potential candidate due to its direct and wide band gap and its ability to tailor electronic, magnetic and optical properties through doping and alloying [9]. The possible applications of oxide semiconductors are diodes, visible and solar blind detectors, transparent electronics based on thin film field effect transistors and spintronic devices. ZnO is a much more intense and efficient UV emitter. The free exciton

binding energy of ZnO (60 meV) is more than twice that of GaN (25 meV). The radiative recombination in ZnO is mediated by excitons which leads to narrow emission line width. Based on these properties it is envisioned that ZnO system has a role for a wide range of devices such as blue and UV light emitting hetero junction diodes, diode lasers, optical wave guides, spintronic devices based on diluted magnetic semiconductors, piezo-electric devices, surface acoustic wave based photo detector devices and resonant tunneling devices as well as transparent thin film transistor for display [1–6].

ZnO thin films and nanostructures can be prepared at low temperatures by deposition techniques such as RF sputtering, pulsed laser deposition, chemical vapor deposition, hydrothermal method and chemical method [10–14]. Another interesting feature of ZnO is its ionic nature that lends itself to ease in the micro fabrication process using both wet and dry etching techniques. In the past magnetic materials were considered primarily for storage and sensor applications, but in the emerging high tech scene they are needed to perform various other interesting tasks as well. Indeed such newly identified tasks generally focus on the property of spin polarization and its manipulation across interfaces in hetero structures and other modulated architectures by electric and magnetic fields as well as electro magnetic radiation. The efforts along these lines have come to be recognized and qualified as a new discipline of advanced magneto optoelectronics.

Conventional semiconductor devices rely on the transport of electrical charge carriers - electrons - in a semiconductor such as silicon. Nowadays physicists are trying to exploit the ‘spin’ of the electron rather than its charge to create a remarkable new generation of ‘spintronic’ devices which

will be smaller, more versatile and more robust than those of silicon chips and circuit elements. All spintronics devices [15, 16] act according to the simple scheme: (1) information is stored (written) into spins as a particular spin orientation (up or down), (2) the spins, being attached to mobile electrons, carry the information along a wire, and (3) the information is read at a terminal. Spin orientation of conduction electrons survives for a relatively long time (nanoseconds, compared to tens of femtosecond during which electron momentum decays), which makes spintronic devices particularly attractive for memory storage and magnetic sensors applications, and, potentially for quantum computing where electron spin would represent a bit (called qubit) of information.

The prototype device that is already in use in industry as a read head and a memory-storage cell is the giant-magneto resistive (GMR) [17] sandwich structure which consists of alternating ferromagnetic and nonmagnetic metal layers. Depending on the relative orientation of the magnetizations in the magnetic layers, the device resistance changes from small (parallel magnetizations) to large (antiparallel magnetizations). This change in resistance (also called magneto resistance [18]) is used to sense changes in magnetic fields. Current efforts in designing and manufacturing spintronic devices involve two different approaches. The first is perfecting the existing GMR-based technology by either developing new materials with larger spin polarization of electrons or making improvements or variations in the existing devices that allow for better spin filtering.

1.2 II-VI Semiconductors

The II-VI group semiconductors where each anion is surrounded by four cations at the corners of a tetrahedron or vice versa. This tetrahedral coordination is nature of the covalent bond having sp_3 hybridization. These materials shows substantial ionic character that tends to increase the band gap beyond the one expected from the covalent bonding. The co-ordinates of Zn^{2+} and O^{2-} are both four fold. Wurtzite structure is one of the most common crystal structures of semiconductors. Other semiconductors that crystallize in wurtzite include nitrides (GaN, AlN, BN), II-VI semiconductors (ZnS, CdS, ZnSe, CdSe, ZnTe, CdTe, SiC, InAs, etc.).

1.2.1 Structural properties

The various crystal structures of ZnO; wurtzite (B_4), zinc blende (B_3) and rocksalt (or Rochelle salt) (B_1) are schematically shown in figure 1.1. B_1 , B_3 and B_4 denote the designations for the three phases. Under ambient conditions, the thermodynamically stable phase is that of wurtzite symmetry. The zinc blende ZnO structure can be stabilized only by growth on cubic substrates but the rocksalt or Rochelle salt (NaCl) structure may be obtained at relatively high pressures irrespective of the substrate nature [19].

The wurtzite structure has a hexagonal unit cell with two lattice parameters, 'a' and 'c' in the ratio of $c/a = \sqrt{8/3} = 1.633$. A schematic representation of the wurtzite ZnO structure is shown in figure 1.2. The structure is composed of two interpenetrating hexagonal-close-packed (hcp) sublattices, each of which consists of one type of atom displaced with respect to each other along the threefold c-axis by the amount of $u = b/c = 0.375$,

where ‘ u ’ is the bond length or nearest neighbor distance [13]. Under the common preparation conditions, excess zinc is always found in ZnO. Due to this zinc excess, ZnO is a non-stoichiometric compound and an n-type semiconductor.

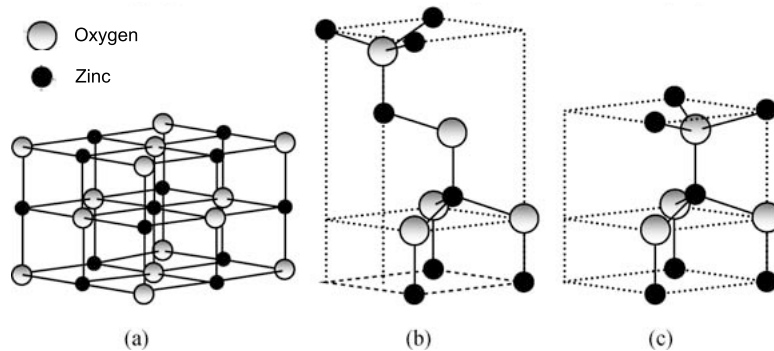


Figure 1.1: Crystal structures of ZnO (a) cubic rocksalt, (b) cubic zinc blend and (c) hexagonal wurtzite.

The point defects in ZnO can be zinc interstitials or oxygen vacancies. However, it is not clear yet that whether zinc interstitial or oxygen vacancy is the dominant defect [20]. In general, two types of thermally formed point defects can be distinguished in ionic crystals, i.e. Schottky defects and Frenkel defects. The dominant defect type can be predicted from the radii of cations and anions. Schottky defects are dominating in the crystals with nearly equal radii of cations and anions. These defects appear as pair-wise vacancies of cations and anions. Frenkel defects are dominating defects if one ion radius is distinctly smaller than the other one. These defects appear as pair-wise interstitials and vacancies of the smaller ions. At octahedral coordination the ionic radius of O^{2-} ion and Zn^{2+} ion are 1.32 Å and 0.74 Å respectively. If we consider ZnO as an ionic crystal,

Frenkel disorder in the zinc sub-lattice seems to be preferred since the radius of Zn^{2+} is much smaller than that of O^{2-} . However, the nearest neighbors in ZnO are tetrahedrally coordinated the covalent radii of zinc and oxygen are 1.31 Å and 0.60 Å respectively. So if ZnO is treated as a covalent compound, Frenkel disorder in the oxygen sublattices is preferred. The ionicity of ZnO was found to be about 50-60%, which corresponds to an effective ionic charge of 1 to 1.2. As a result, the dominating defects in ZnO can not be figured out from the consideration of ionic and covalent radii.

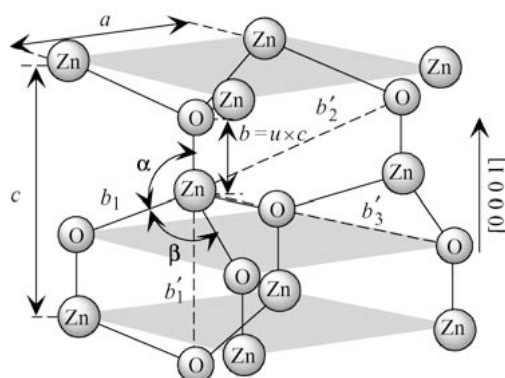


Figure 1.2: Schematic representation of a wurtzite ZnO structure having lattice constants a in the basal plane and c in the basal direction; $u = 0.375$ [21].

The O-Zn distance of the nearest neighbors is 1.992 Å in the direction parallel to the c -axis of the hexagonal unit cell and 1.973 Å in the other three directions of the tetrahedral arrangement (figure 1.2). The tetrahedral arrangement of the nearest neighbors indicates the covalent bond between the Zn and O atoms [21]. Like other II-VI semiconductors, wurtzite ZnO can be transformed to the rocksalt (NaCl) structure at relatively modest

external hydrostatic pressures. The reason for this is that the reduction of the lattice dimensions causes the interionic Coulomb interaction to favor the ionicity more over the covalent nature. However, the rocksalt structure cannot be stabilized by the epitaxial growth. In ZnO, the pressure-induced phase transition from the wurtzite to the rocksalt phase occurs at approximately 10 GPa and a large volume decrease of about 17%.

1.2.2 Optical properties

ZnO is a wide band gap semiconductor (3.37 eV) at room temperature with an exciton binding energy of 60 meV. ZnO normally shows near ultraviolet and the visible emissions. The band edge emission is centered at approximately 380 nm; and the visible deep level emission in the range of 450-730 nm. The UV emission is considered the near band edge emission which depends on the crystal quality of the film or nanostructures while the visible emissions are related to various intrinsic defects in ZnO crystal [20]. But both of them depend greatly on the preparation methods and conditions.

An ideal semiconductor is at its ground state at 0 K, if there is not any excitation source. In its ground state, the bands below the top of valence band are fully filled with electrons and the conduction band is completely empty. If an electron is excited from the valence band to the conduction band by a photon with energy equal to or more than band gap, the N electron system of the semiconductor is brought to an excited state from the ground. The quanta of these excitations are called "excitons" [22]. Although excitons can be described at various levels, the effective mass model is the most useful and simplest one. In this picture, exciton is considered as a pair of electron and hole that interacts each other through Coulomb field. Naturally exciton represents the interaction of a system with

N-1 electrons in the valence band and one electron in the conduction band. In the effective-mass approximation, the (N-1) electrons are represented by a hole with its effective mass determined by the valence band structure. The whole problem of exciton in this frame is, therefore to find a solution of a hydrogen-like electron-hole bound pair in the media of the semiconductor. The energy dispersion relation of excitons with wave vector, K can be written as [22]

$$E_{ex}(n_B K) = E_g - \frac{Ry^*}{n_B^2} + \frac{\hbar^2 K^2}{2M} \quad (1.1)$$

Where E_g is the band gap energy of the semiconductor; $n_B=1, 2, 3$. is the principle quantum number; $M=m_e+m_h$, $K=k_e+k_h$ are the translational mass and wave vector of the exciton. Ry^* is the exciton binding energy,

$$Ry^* = 13.6 \frac{\mu}{m_e} \frac{1}{\epsilon^2} (eV) \quad (1.2)$$

$$\mu = \frac{m_e m_h}{m_e + m_h} \quad (1.3)$$

Vibrational properties of ZnO probed by techniques such as Raman scattering and IR measurements. In the case of wurtzite ZnO the number of atoms per unit cell (s) is = 4, and there is a total of 12 phonon modes, namely, one longitudinal acoustic (LA), two transverse acoustic (TA), three longitudinal optical (LO) and six transverse optical (TO) branches. In the zinc blende polytypes with $s=2$, only six modes are present, three of which are acoustical (one LA and two TA) and the other three are optical (one LO and two TO) branches. In the hexagonal structures with C_{6v}^4 symmetry, group theory predicts eight sets of phonon normal modes, namely,

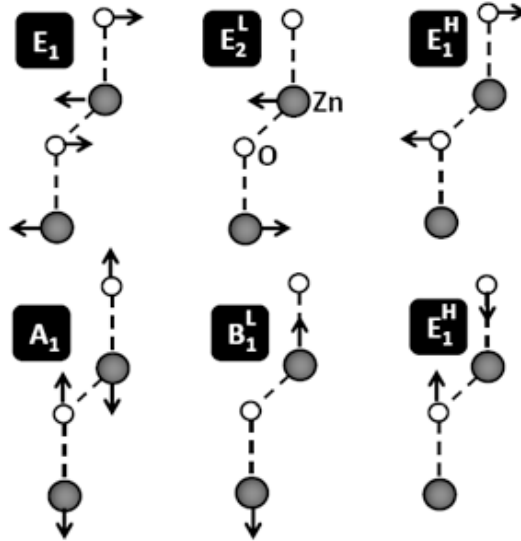


Figure 1.3: Schematic diagram of optical phonon modes and their vibrational directions in the ZnO.

$2A_1+2E_1+2B_1+2E_2$. Among them, one set of A_1 and E_1 modes are acoustic, while the remaining six modes, namely, $A_1+E_1+2B_1+2E_2$, are optical modes [21]. The optical phonon modes and their vibrational directions are shown in figure 1.3.

1.2.3 Band gap engineering

Oxide based thin-film hetero-structures are technologically attractive for future optoelectronic devices because of their exciting fundamental intrinsic and extrinsic optical, electrical, magneto-optical and piezoelectric properties. The difficulty in bipolar carrier doping both n and p types is a major obstacle as seen in other wide band gap semiconductors such as GaN and II-VI compound semiconductors including ZnS, ZnSe, and ZnTe. Unipolar

doping can be easily obtained in wide-band gap semiconductors: ZnO, GaN, ZnS, and ZnSe are easily doped to n-type, while p-type doping is difficult [13]. In the class of optoelectronic materials, the growth and characterization of II-VI semiconductor ZnO and ZnO-based alloys including ZnMgO, ZnCdO, and ZnMnO have become an active research field in recent years. These alloys are widely used for band gap engineering and spintronic applications [23]. Alloying ZnO with MgO or CdO potentially permits the band gap to be controlled between 2.8 eV and 4.2 eV without phase segregation, which facilitates band gap engineering. The research works have been encouraged by both scientific significance and the potential of various practical applications such as light-emitting diode (LEDs), ultraviolet photo detector, UV-blue semiconductor laser, flat panel displays, solar cell, gas sensor, surface acoustic wave devices and so on. Compact ultraviolet sources and detectors developed will find applications in monitoring or to catalyze certain chemical reactions or to excite fluorescence in various proteins.

Recently several near ultraviolet diode sources and detectors have been prepared through band gap engineering by alloying two or more semiconductors, like GaN, GaAs material systems. But the variation of band gap as a function of alloy composition is the largest for ZnO- based alloys than that found in well established semiconductor systems such as GaAs, AlGaIn and GaN. ZnO and its alloys can be deposited low deposition temperatures by low-cost deposition techniques, such as RF sputtering [10, 24], Pulsed laser deposition (PLD) [11, 25, 26] and Chemical vapor deposition (CVD) [12, 27]. Another interesting feature of ZnO is its ionic nature that lends itself to ease in the microfabrication process using both wet and dry etch technique. The crystalline structure of ZnO is hexagonal wurtzite and MgO

has a cubic structure of NaCl type. The band gap of MgO is 8.2 eV. Although MgO have different crystal structures, these two materials can still be alloyed with each other to form MgO-ZnO compounds.

1.3 Dilute Magnetic Semiconductors

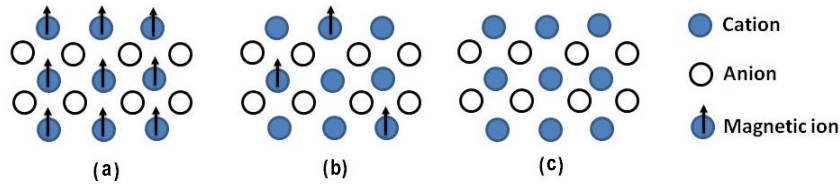


Figure 1.4: (a) Magnetic semiconductor, (b) Diluted magnetic semiconductor and (c) non-magnetic semiconductor

Diluted magnetic semiconductors (DMS) are compounds of alloy semiconductors (figure 1.4) containing a large fraction of magnetic ions. DMS are studied mainly on II-VI based materials such as CdTe and ZnSe etc. This is because magnetic ions with +2 valency are easily incorporated into the host II-VI crystals by replacing group II cations. In such II-VI based DMS such as (CdMn)Se, magneto-optic properties were extensively studied and optical isolators were recently fabricated using their large Faraday effect [28]. DMS based on p- and n- type CdTe and ZnSe are difficult to create, which make these materials less attractive for spintronic applications.

Recently ZnO has renewed interest since it was found that high quality epitaxial thin film shows ultra violet laser action at room temperature [29, 30]. In addition the energy gap of this compound can be extended up to 4 eV by synthesizing alloys of $Zn_{1-x}TM_xO$. Heavy electron doping

was readily achieved in ZnO in contrast to the other II-VI compound semiconductors. Furthermore the thermal equilibrium solubility of magnetic materials such as Mn is larger than 10 mol% and the electron mass is as large as $0.3 m_e$, where m_e free electron mass. According to Ruderman-Kittel-Kasuya-Yosida (RKKY) interaction, the above mentioned factors favour strong correlation between spin and carriers[21, 30, 34].

1.3.1 Spintronics - general idea

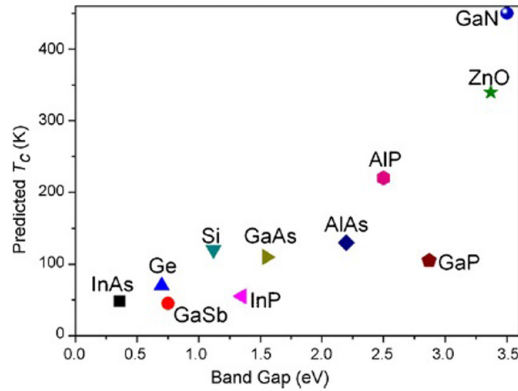


Figure 1.5: Theoretically predicted Curie temperatures for various DMS [6].

Spintronics is an emerging technology exploiting both the intrinsic spin of the electron and its associated magnetic moment, in addition to its fundamental electronic charge. Recent advances in the emerging technologies of spintronics and related devices have attracted widespread attention. Consequently, the quest for integrating the semiconducting properties with the magnetic properties in a material has become a prerequisite for successful fabrication of useful devices such as high performance read heads, non-

volatile memories and other state of the art storage devices. Dilute magnetic semiconductor (DMS), obtained by incorporating magnetic impurities in host semiconductors, serve this purpose. Dilute magnetic semiconductors have been of much interest and have been studied actively for the use of both charge and spin of electrons in semiconductors. There have been many advances in the recent past in this area, particularly in the wide band gap, III-V and II-VI based DMS material. Until now applications using such materials were possible only at low temperature owing to the low Curie temperature (T_C) of such DMS. *Dietl et al.* [6] theoretically predicted the possibility of room temperature ferromagnetism in III-V and II-VI based DMS materials. But only a few transition metal elements (Mn, Co, Ni, Fe, Cu etc.) doped ZnO [6, 31–33] exhibits T_C much above 300K (figure 1.5). ZnO:TM is interesting not only in terms of its room temperature ferromagnetism but also its transport properties.

Spintronics is becoming an area of active research because of the tremendous potential ahead both in terms of fundamental physics and technology. Since one exploits the spin degree of freedom of the electrons along with its charge, spintronics combines standard microelectronics with spin-dependent effects that arise from the interaction between electrons and a magnetic field. So one can expect a new generation of devices with completely different functionality. The advantages of magnetic devices would be non-volatility, increased data processing speed, less electric power consumption and increased integration densities compared to present semiconductor devices. The rapid miniaturization of the microelectronics is approaching its limit that the generated heat cannot dissipate fast enough to avoid the proper functioning of the devices.

Spintronics is a multidisciplinary in nature - the actual concept of the field is to incorporate and manipulate the spin of the electron in addition to its charge in the solid state systems. The band gap engineering can be applied to maximize the light output in spin LEDs [16, 17]. DMS in which magnetic ions substituted for cations of the host semiconducting material are ideal systems for spintronics. The combination of band gap engineering and the integration of magnetic degrees of freedom give birth to new generation of devices with completely different functionalities. The discovery of giant magneto resistance (GMR) [28] in magnetic multilayers has triggered intense experimental as well as theoretical studies to exploit the potential technological applications and to understand the underlying physical phenomena that cause this effect. The giant magneto resistance is realized in metallic multilayers where alternating layers of ferromagnetic and non-magnetic metallic layers are stacked together. The resistance of such a multilayer stack depends on the relative alignment of the magnetizations of the ferromagnetic layers due to spin dependant scattering at the interface or the bulk of the ferromagnetic layer. For the use as a magnetic field sensor or a magnetic read head one requires high sensitivity in accordance with the rapidly expanding data storage capabilities of the high density recording medium, so new concepts and technologies are emerging to cope with these technological demands.

1.3.2 Magnetic properties of materials

The magnetic materials are classified based on their response to external magnetic fields. The magnetism in a material arises due to the orbital and spin motions of electrons and how the electrons interact with one another. The main delineating factor is that in some materials there is no collective

long range interaction between atomic magnetic moments, whereas in other materials there is a very strong interaction. The magnetic behavior of materials can be classified into the following five major groups: diamagnetic, paramagnetic, ferromagnetic, antiferromagnetic, and ferrimagnetic.

(i) Diamagnetism

The diamagnetic materials includes all nonmagnetic semiconductors such as Si, Ge, GaAs, GaN, ZnO etc. Diamagnetism arises from the tendency of the electrical charge to partially screen the interior of the body from the applied magnetic field. Diamagnetic substances are composed of atoms that have no net magnetic moments. In the absence of a magnetic field, circulating current around the nucleus is zero, and the magnetic moment is zero. When applying an external magnetic field the motion is described by Lorentz force and Lenz's law dictates that when the magnetic flux changes in a circuit, a current is induced to oppose that change. The centrifugal and centripetal forces are rebalanced by the magnetic force causing the orbital frequency of an electron with orbital magnetic moment parallel to the field to slow down and the one that is antiparallel to the field to speed up. So a negative magnetization (M) is produced against the applied magnetic field (H) with a negative slope. The susceptibility is negative ($\chi < 0$) and small but it is temperature independent [21, 35, 36].

(ii) Paramagnetism

Paramagnetism arises due to unpaired electrons in the atoms or ions in the material. Examples include V^{2+} , Cr^{2+} , Mn^{2+} , Fe^{2+} , Co^{2+} and Ni^{2+} among

the transition elements and Gd^{3+} among the rare earths. The magnetization (M) versus magnetic field (H) curve in these materials follow a linear relationship with a positive slope and positive susceptibility ($\chi > 0$). The magnetization would eventually saturate, as all the magnetic ions would have their magnetic moments aligned [21, 35, 36]. As the temperature increases, the thermal agitations increases and alignment becomes harder, thus the susceptibility decreases. This behavior is known as the Curie law. It should in fact be recognized that the Curie law is a special case of the more general CurieWeiss law ($\chi = C/[T - \theta]$), which incorporates a temperature constant (θ) and derives from the Weiss theory proposed for ferromagnetic materials that incorporates the interaction between magnetic moments.

(iii) Ferromagnetism

Ferromagnetic materials are the most magnetically active substances having very high magnetic susceptibilities ($\chi \sim 1,000 - 1,00,000$). These materials are made of atoms with permanent dipole moments. Weiss postulated the existence of magnetic domains within which the atomic magnetic moments are aligned. The movement of these domains determines how the material responds to an applied magnetic field and as a result, the susceptibility is a function of the applied magnetic field [21, 35, 36]. Therefore, ferromagnetic materials are usually compared in terms of saturation magnetization rather than susceptibility. If a ferromagnetic sample is placed in a strong magnetic field, the domains can be forced to coalesce into large domains aligned with the external field. When the external field is removed, the electrons in the bonds maintain the alignment and the magnetism remains. If a ferromagnetic material is heated to too high a temperature, it ceases to

be ferromagnetic. The reason is that above a certain critical temperature, called the Curie temperature [21, 35], the thermal motion of the atoms is so violent that the electrons in the bonds are no longer able to keep the dipole moments aligned. When this happens, the ferromagnetic material changes into a paramagnetic material with the usual weak magnetism.

(iv) Antiferromagnetism

In materials exhibiting antiferromagnetism, the neighboring spins are aligned in a regular fashion as in the ferromagnetic materials, but pointing in the opposite directions. In the simplest case, the material can be assumed to be composed of two sublattices, where the spins associated with sublattice A and sublattice B are completely antialigned so as to have zero net magnetization, despite the magnetic ordering. All of these antialignment effects only take place at temperatures below the Neel temperature, T_N . Above the Neel temperature, the material is typically paramagnetic [21, 35, 36]. The only element exhibiting antiferromagnetism at room temperature is chromium with a Neel temperature of 37°C . Cr has a body centered cubic lattice with the body center atomic spins are directed opposite to those at the cube corners, which are both equal in number. The clue to antiferromagnetism is the behavior of susceptibility above the Neel temperature, where the susceptibility obeys the CurieWeiss law for paramagnetism but with a negative intercept indicating negative exchange interaction energy. Antiferromagnetic materials, such as Cr and Mn, possess small but positive susceptibility ($\chi > 0$).

(v) Ferrimagnetism

As alluded earlier, a material is ferromagnetic only if all of its magnetic ions are aligned and add a positive contribution to the net magnetization. If some of the magnetic ions subtract from the net magnetization (if they are partially antialigned), then the magnetic behavior is called ferrimagnetism. Ferrimagnetic materials such as ferrites that utilize transition element Fe as in Fe_2O_3 exhibit magnetism similar to ferromagnetic materials below the Curie temperature, T_C . Above this temperature, they become paramagnetic as in the case of ferromagnetic materials. Ferrimagnetism is observed only in compounds with complex crystal structures. In these materials, the exchange interactions lead to parallel alignment of atoms in some of the crystal sites, sublattice A, and antiparallel alignment of others, those in sublattice B. The material breaks down into magnetic domains, as in antiferromagnetic materials. The main difference between ferrimagnetic and antiferromagnetic materials is that the magnetic moment associated with sublattice A atoms is larger than, as opposed to being equal to that of sublattice B atoms so they do not null each other. The magnetic behavior in ferromagnetic and ferrimagnetic materials is also very similar [21, 35, 36]. However, ferrimagnetic materials generally have lower saturation magnetizations.

1.3.3 Magnetism in nanostructures

The magnetic properties of the nanomaterials changes from that of the bulk [35, 36]. The features are listed below

(i) Coercivity of fine particles

As the size of the nanoparticles reduces the coercivity increases, goes through a maximum and then tends towards zero as shown in figure 1.6.

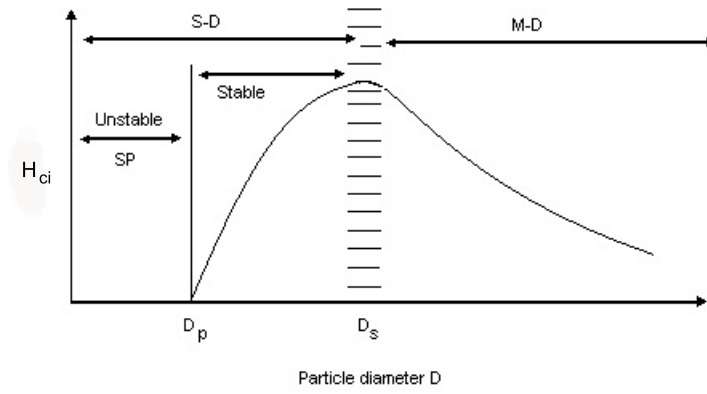


Figure 1.6: Schematic diagram of the variation of coercivity with particle diameter

Beginning at large sizes, we can distinguish the following regions:

1. Multidomain (M-D): magnetization changes by domain wall motion. For most materials the size dependence of the coercivity (H_{ci}) is experimentally found to be given approximately by

$$H_{ci} = a + \frac{b}{D} \quad (1.4)$$

where a and b are constants.

2. Single-domain (S-D): Below a critical diameter D_S , which is not well defined, the particles become single domains and in this size range

the coercivity reaches a maximum. Particle of size D_S change their magnetization by spin rotation.

a) As particle size decreases below D_S the coercivity decreases, because of thermal effects, according to

$$H_{ci} = g - \frac{b}{D^{3/2}} \quad (1.5)$$

where g and h are constants

b) Below a critical diameter D_P the coercivity is zero, again because of thermal effects, which are now strong enough to spontaneously demagnetize a previously saturated assembly of particles. Such particles are called superparamagnetic (SP).

(ii) Superparamagnetism

In ferromagnetic materials there is spontaneous magnetization, which arises due to the interaction between the neighbouring atomic magnetic dipoles. It is called spin exchange interaction and is present in the absence of external magnetic field. The exchange interaction aligns the neighbouring magnetic dipole moments parallel to one another and this spreads over a finite volume of the bulk. This small volume is called the domain. Each domain is spontaneously magnetized, the magnetization being appropriate to temperature T . In an unmagnetised piece of ferromagnet the domains are not aligned. When external field is applied magnetization of the specimen may occur either by the growth of one domain at the expense of another i.e., by the motion of domain walls. If the size of the ferromagnetic particle is reduced below a critical particle size it would consist of single magnetic domain. This single domain particle is in a state of uniform magnetization

at any field. Let us consider such a particle whose total magnetic moment is directed at an angle θ to an applied field H . For the sake of simplicity let us consider only one preferential direction (direction of easy magnetization) and let us call V the particle volume and the angle between the easy axis and the magnetic moment directions. The anisotropy energy,

$$E = KV \sin^2 \theta \quad (1.6)$$

K is also sometimes called anisotropy constant but one must keep in mind K may depend drastically on temperature.

Consider an assembly of aligned uniaxial particles that are fully magnetized along the easy symmetry axis. After the field is removed the resulting remanence will vanish as

$$M_r = M_s \exp\left(-\frac{t}{\tau}\right) \quad (1.7)$$

M_s is the full magnetization t is the time after the removal of field τ is the relaxation time for the process

The relaxation time is given by

$$\frac{1}{\tau} = f_0 \exp\left(-\frac{KV}{kT}\right) \quad (1.8)$$

As the particle volume V becomes smaller, the relaxation rate increases. Hence let us consider an observation time τ_m , characteristic of the measurement technique (measuring time for magnetometers, Larmor precession period for Mossbauer spectroscopy etc.). If $\tau_m \gg \tau$, the measurement result is averaged over a great number of reversals. For example under zero fields the magnetic moment of a particle is averaged to zero. This is the superparamagnetic state [36, 37]. If $\tau_m \ll \tau$ the magnetic moment appears

blocked in one of the two directions of the easy axis. This is the blocked state. Hence, depending on the values of the anisotropy constant, the particle volume and the characteristic measurement time, it may be possible to evidence the transition from the superparamagnetic to the blocked regime by decreasing the temperature. The temperature at which this transition occurs is called the blocking temperature. For uniaxial particles, the T_b is given by

$$T_b = \left(\frac{KV}{25k}\right) \quad (1.9)$$

The blocking temperature in a superparamagnetic system decreases with increasing measuring field, being proportional to $H^{2/3}$ at larger magnetic fields and proportional to H^2 at low fields.

However the two main aspects of superparamagnetism are

1. Magnetization curves measured at different temperatures superimpose when M is plotted as a function of H/T .
2. There is no hysteresis, i.e., both the retentivity and coercivity are zero.

(iii) Surface magnetism

Fine particles provide an attractive avenue for the study of the magnetic properties of surfaces. Fine particles possess many advantages over the thin films namely

1. Surface area relative to the volume can be varied over a relatively wide range. It may be possible to distinguish between the surface, close to surface and bulk properties.

2. Fine particles have only one interface. By contrast thin films have two and at least one of these, is in intimate, perhaps paraxial, contact with the substrate. The fine particles interface may be vacuum, gas, liquid or solid surfactant or the contact with a binder.
3. Fine particles may be superparamagnetic, a phenomenon that depends on both the volume and the anisotropy. Any change in the surface anisotropy can be monitored by superparamagnetism measurements.

1.3.4 Magnetic Interactions in DMS

In DMS we have two systems, one comprising of the host semiconductor and the other of the magnetic ion. The host semiconductor have extended states made by delocalized band electrons. The magnetic ions have localized 3d or 4f shell. The electrical and optical properties of DMS are described by the effective mass of the carriers. The localized magnetic moments of the magnetic ions and their interaction with the host semiconductor determine the magnetic properties. The commonly occurring interactions are sp-d and sp-f for transition metal ions and rare earth magnetic ions. The spin-spin interaction between magnetic ions can be classified into four major types. Ruderman-Kittel-Kasuya-Yoshida (RKKY) mechanism leads to spin polarization of the conduction electrons. The band polarization is occurred by Blombergen-Rowland (BR) interaction [21, 36]. The superexchange and double exchange is possible by the virtual transition between the magnetic ions and neighboring anions.

(i) Carrier-single magnetic interaction

The interaction between the ionic magnetic impurity and the host involving conduction and valence band electrons is described by direct Coulomb exchange, which is a first-order perturbation effect. The direct Coulomb exchange is represented by the ferromagnetic Kondo Hamiltonian [6, 21, 34, 36].

$$H_{ex} = -xN_0\alpha\langle S_{//} \rangle s_{//} \quad (1.10)$$

xN_0 is the concentration of magnetic ions with mole fraction x , α is the exchange constant for s electrons and $\langle S_{//} \rangle$ is the average magnetic moment along the field direction.

$N_0\alpha$ is the spin exchange integral for conduction band. In II-VI DMS materials α is of the order of about 0.2 eV.

The spin-dependent part of the exchange Hamiltonian for interaction between the Γ_8 valence band p-like electrons and all the three t_{2g} d-orbitals occupied by one electron can be described as

$$H_{ex} = -\frac{1}{3}xN_0\beta\langle S_{//} \rangle J_{//} \quad (1.11)$$

where β is the exchange constant, $J_{//}$ component of the total angular momentum of the p orbital parallel to the applied field.

II-VI DMSs indicated that β and α have opposite signs and β is larger by a factor 510 or even more depending on the host material.

(ii) Superexchange interaction

Superexchange mechanism arises due to the spin dependent kinetic exchange interaction between each of the two magnetic ions and the valence

bands [21, 36]. The four virtual transitions from p-like valance band state to the ions and back to the valance band are schematically represented in the figure 1.7. When a band electron is transferred to one of the ions, leading hole in the valance band. So the intermediate state is having one magnetic ion with N and second with $N+1$ electrons. Second transition arises another possibility with $N+1$ electrons on both ions and two holes in the valance band or one with $N+1$ and $N-1$ electrons and no holes in the valance band.

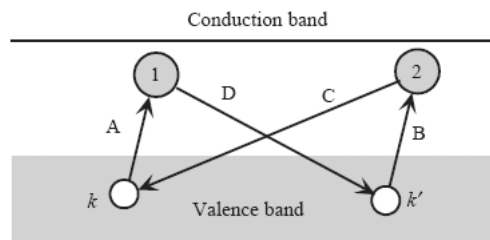


Figure 1.7: Schematic representation of four virtual transitions of the superexchange ion-ion interactions. The electron transitions are shown by the path ABCD or CADB [21].

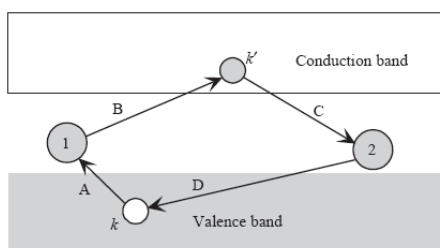
(iii) Blombergen-Rowland (BR) exchange mechanism

Figure 1.8: Schematic representation indicating virtual B-R exchange interactions. The electron transitions are possible by the transfer of electron either from the valence band to one of these ions [21].

BR exchange mechanism is a process wherein the spins of two ions are correlated owing to the spin-dependent kinetic exchange interaction between each of the two ions and the valence band (p-type) and conduction band (s-type). BR exchange process differs from the superexchange mechanism only by the specifics of the intermediate states and also allows for virtual transitions to the empty conduction band as illustrated in Figure 1.8. Naturally, this mechanism is less likely than the superexchange mechanism, particularly, in large bandgap semiconductors, as the path is more complex [21, 36].

(iv) Double exchange interaction

According to Zener the double exchange mechanism is the coupling between the magnetic ions in the different charge states by virtual hopping of the extra electron from one ion to another [6, 21, 34, 36]. In $\text{Mn}^{2+} - \text{Mn}^{3+}$ system the d-electron will hop between these ions through the p-orbitals

of neighboring anions. But this mechanism is not responsible for the long range order in DMS because the electrons remains localized at the magnetic ion and not contribute to the charge transport. If the neighboring magnetic moments are in the same direction, widening of the d band occurs due to hybridization and the band energy is lowered by introducing carriers in the d band. The theoretical investigations is not much progressed because of the fact that both disorder and interactions are strong and it can be treated non-perturbatively.

(v) RKKY interaction

The Ruderman-Kittel-Kasuya-Yoshida (RKKY) mechanism describes the exchange coupling between the magnetic ion and the band electrons. In a degenerate DMS the interaction is described by s-d Kondo Hamiltonian - first order perturbation effect [21, 34, 36]. The conduction electron gas is magnetized by the magnetic ion, the degree of polarization decreases with distance from the magnetic ion in an oscillatory fashion. These kind of indirect exchange coupling between the magnetic ions may lead to ferromagnetic or antiferromagnetic interaction depending upon the distance of separation of the interacting atoms. The coupling at a distance 'r' having fermi surface (k_F) is

$$J_{RKKY}(r) \propto \frac{\cos 2k_F r}{r^3} \quad (1.12)$$

(vi) Bound magnetic polarons

Ferromagnetism in DMS arises due to percolation of bound magnetic polarons (figure 1.9). The localized holes of the polarons act on the transition

metal producing an effective magnetic field hence align the spins. Below the Curie temperature the neighboring polarons overlap and forming clusters of polarons [21, 33, 34, 36]. Ferromagnetic transition is possible when the size of the cluster is equal to the size of the sample. The low carrier density is a feature of the bound magnetic polarons and the model is applicable to both n-type and p-type host materials.

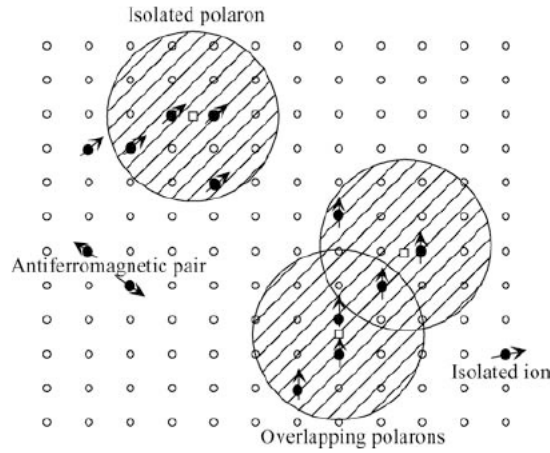


Figure 1.9: Schematic representation of magnetic polarons with magnetic cation concentration $x=0$. Cation sites are represented by small circles.

1.4 Applications of ZnO

1.4.1 Importance of ZnO in optoelectronics

ZnO is a wide band gap semiconductor ($E_g = 3.37$ eV) with large exciton binding energy of 60 meV that displays luminescent properties in the near ultra violet and the visible regions. The UV emission is at ~ 380 nm and the visible deep level emission is in the range of 450-730 nm. The UV emission is

considered to be the near band edge emission which depends on the crystal quality of the film, while the visible emissions are related to various intrinsic defects. But both of them depend greatly on the preparation methods and conditions. ZnO has a strong potential for various short-wavelength optoelectronic device applications and for that both high quality n- and p-type ZnO are indispensable.

The structural and optical properties of the ZnO bulk, thin films and nanostructures were elucidated by various groups in the past decades. The ZnO and its alloys can be deposited at low deposition temperatures by low-cost deposition techniques, such as RF sputtering [10, 24], Pulsed laser deposition [11, 25, 26] Chemical vapor deposition (CVD) [12, 27] and hydrothermal method [13]. Another interesting feature of ZnO is its ionic nature that lends itself to ease in the microfabrication process using both wet and dry etch technique. By controlled doping we can tune the electrical property from that of insulator to semi metal without diminishing the optical transparency. The theoretical prediction of RTFM followed by experimental confirmations pave way to the wide usage of ZnO in spintronics.

1.4.2 TM doped ZnO for spintronics

Transition metal ions with partially filled d orbitals (Mn, Co, Ni, Cu etc.) are widely used in DMS as magnetic elements. The electronic structure of the host ZnO lattice is influenced by the strong hybridization of 3d orbitals of transition metals with s and p orbitals of the anions. The 3d-TM doped ZnO gained much attention after the prediction of room temperature ferromagnetism by Diet *et al.*. ZnO is having wurtzite structure formed by tetrahedral bonding and the TM elements have valance electrons in the partially filled d orbitals and in 4s orbitals. During doping the TM ions

substitute the Zn^{2+} in the ZnO host lattice contributing 4s electron to the s-p₃ bonding to give a TM^{2+} state. The electronic states of the TM dopants are show in figure 1.10.

Orbital	V 4s ² 3d ³	Cr 4s ¹ 3d ⁵	Mn 4s ² 3d ⁵	Fe 4s ² 3d ⁶	Co 4s ² 3d ⁷	Ni 4s ² 3d ⁸	Cu 4s ¹ 3d ¹⁰
4s	↑↓	↑	↑↓	↑↓	↑↓	↑↓	↑
3d	↑↑↑	↑↑↑↑↑	↑↑↑↑↑	↑↓↑↑↑	↑↓↑↓↑↑	↑↓↑↓↑↑	↑↓↑↓↑↓↑↓
3p ⁶	↑↓↑↓↑↓	↑↓↑↓↑↓	↑↓↑↓↑↓	↑↓↑↓↑↓	↑↓↑↓↑↓	↑↓↑↓↑↓	↑↓↑↓↑↓
3s ²	↑↓	↑↓	↑↓	↑↓	↑↓	↑↓	↑↓
2p ⁶	↑↓↑↓↑↓	↑↓↑↓↑↓	↑↓↑↓↑↓	↑↓↑↓↑↓	↑↓↑↓↑↓	↑↓↑↓↑↓	↑↓↑↓↑↓
2s ²	↑↓	↑↓	↑↓	↑↓	↑↓	↑↓	↑↓
1s ²	↑↓	↑↓	↑↓	↑↓	↑↓	↑↓	↑↓

Figure 1.10: Electronic configuration of 3d and 4s states of the transition metal elements.

Theoretical calculations by Sato *et al.* [38] and Yoshida *et al.* [39] predict that ZnO show ferromagnetism for lower Mn doping concentration (5%) without any additional dopants for increasing the free electron concentration. Low temperature processing has been found to be essential for controlling the electron carrier concentration in Mn doped ZnO [40]. Various groups have demonstrated the room temperature ferromagnetism in Mn doped ZnO [41, 42] but there are some contradictory reports also [43, 44]. The origin and reproducibility of the ferromagnetism are still controversial and the magnetic properties are very sensitive to thin film preparation methods and conditions. Pulsed laser deposition (PLD) offers the advantages such as deposition at relatively high oxygen pressure, high deposition

rate and growth of highly oriented crystalline films at low substrate temperature. ZnO nanostructures have been prepared by chemical methods and hydrothermal methods. The hydrothermal process have several advantages over other growth processes such as use of simple equipment, catalyst-free growth, low cost, large area uniform production, environmental friendliness and less hazardous.

The phase diagram analysis shows that significant amount of Mn^{2+} can be incorporated into hexagonal ZnO lattice even at relatively low temperatures. The solubility of Mn^{2+} in ZnO is 13 per cent. It was found that the lattice constants of ZnO change considerably with increasing Mn content. There is also a good agreement between the solubility determined by the change in lattice constant and that measured by the electron probe. However the solubility of Zn^{2+} in cubic MnO is relatively low at lower temperatures. At temperatures below 500°C , Zn ions cannot be incorporated into MnO. The solubility of Zn^{2+} in MnO is about 10 percent at 800°C . Several groups have reported the growth of ZnMnO alloy thin films [45, 46]. Epitaxial growth of ZnMnO thin films can be realized at substrate temperatures in the range from 600 to 750°C on sapphire substrates. The maximum solubility of Mn in ZnMnO alloy films are about 35%, which is much higher than the solubility limit for the bulk material.

The structural and magnetic properties of Co doped ZnO films are related to cobalt concentration and growth conditions. Films doped with cobalt concentrations of a few percent appeared to be composed of two magnetic components: a paramagnetic component and a low field ferromagnetic component. Only the oxygen depleted samples of Co doped ZnO samples exhibit ferromagnetism. Lower growth pressures results in more oxygen vacancies inducing free electron which mediate the ferromagnetic

exchange interaction. Some exhibit Curie temperature higher than room temperature. Ferromagnetism is found only in inhomogeneous film supporting the formation of cobalt clusters during the growth process. The magnitude of the observed magnetism is too large to be attributed to the weak magnetization of cobalt oxide [48]. A metal insulator transition occurs in such samples. There is variation of lattice constant with concentration of cobalt. The sequential increase in cobalt concentration increases band gap. In the film cobalt ions substitute for the zinc ion without changing the wurtzite structure. It shows three well-defined absorption peaks at 660 nm, 615 nm and 568 nm. Diffuse reflectance decreases with increase in cobalt concentration. As the cobalt concentration increased, band tailing become evident in the data with the onset of absorption at lower energy, and the doping smears out the linear region making a more rounded shape. There is a variation in the band gap (blue shift or red shift) when cobalt is doped. ZnO films are colour less, but $\text{Zn}_{1-x}\text{Co}_x\text{O}$ films are green in colour.

$\text{Zn}_{1-x}\text{Ni}_x\text{O}$ films shows ferromagnetism at lower doping percentages. Lower growth pressures results in more oxygen vacancies inducing free electron which mediate the ferromagnetic exchange interaction [47], some exhibit Curie temperature higher than room temperature. Ferromagnetism is found only in inhomogeneous films supporting the attribution of the observation to the presence of nickel clusters. The magnitude of the observed magnetism is too large to be attributed to the weak magnetization of nickel oxide. Wakano *et al.* reported the observation of ferromagnetism at 2 K for the Ni-doped ZnO films, which become superparamagnetism at 30 K and maintain it up to 300 K [49]. Yin *et al.* reported the paramagnetism in the Ni-doped ZnO films [50]. On the other hand, ferromagnetism is observed

at room temperature in Ni doped ZnO nanorods [51] and Ni-doped ZnO films [52].

Initial studies of ZnO doped with Cu by various groups showed contradiction with each other showing non-magnetic and magnetic nature of ZnO:Cu system. Some initial theoretical studies of 25% Cu doped ZnO system showed nonmagnetic behavior. Later theoretical studies at lower doping levels indicated ZnO doped with 6.25% and 3.125% Cu should be ferromagnetic. This variation was reconciled by noting the proximity of the copper dopant atoms with respect to each other in the different studies. Spin polarized density functional calculations predict certain ZnO:Cu structures should be ferromagnetic [6]. When deposited under the appropriate growth conditions, ZnO:Cu films grown by pulsed-laser deposition (PLD) show evidence of ferromagnetism [56]. Jin *et al.* [57] reported that ferromagnetism was not observed in Cu-doped ZnO thin films prepared by combinatorial laser molecular-beam epitaxy method. However, recently Buchholz *et al.* [58] reported RT FM in p-type Cu-doped ZnO thin films but nonferromagnetic behavior in n-type Cu doped ZnO at RT.

Very recently, theoretical studies by Ye *et al.* [59] indicated that in Cu-doped ZnO whether n type or p type the energy of the ferromagnetic state is lower than that of the antiferromagnetic state, thus Cu-doped ZnO would be expected to achieve RTFM. Theoretical modeling of the ZnO:Cu system indicates that the location of the copper atoms relative to each other can strongly affect the magnetic properties of the system. Some reports shows that the stability of ferromagnetism in ZnCuO system depends on the copper atom separation. For the case where the copper atoms were separated by 5.20 Å along the c-axis the ferromagnetic state was favored, but for the case where the copper atoms were separated by 3.25 Å within the basal

plane the antiferromagnetic state was favored. Sato's work looked consistent with the other theoretical calculations and together establishing the importance of copper-atom placement in the doping process [38]. ZnO:Cu has the possibility of being free of ferromagnetic precipitates because metallic copper is not magnetic, and neither Cu_2O nor CuO is ferromagnetic, and hence form an unambiguous DMS.

Ueda *et al.* [46] also investigated $\text{Zn}_{1-x}\text{TM}_x\text{O}$ films [n-type ($x=0.05-0.25$): TM = Co, Mn, Cr, Ni] grown by PLD. The Co-doped ZnO films showed the maximum solubility limit of 30%. In $\text{Zn}_{1-x}\text{Co}_x\text{O}$, only a few films showed ferromagnetic features, while the others showed spin-glass-like behaviors. Some of them exhibited ferromagnetic behaviors with a Curie temperature higher than room temperature. The reproducibility of the method was poor (less than 10%). The observed ferromagnetism is directly related to the presence of oxygen vacancies. Because of the lack of detailed micro structural characterization in the reports mentioned [47, 53–55], there is still a good deal of controversy over the fate of these magnetic impurities (nanosized clusters/precipitates and/or individual atoms in substitutional sites) and whether the magnetic behavior is an intrinsic property of the films. Most experimental reports concerning room temperature ferromagnetism in DMS employ x-ray diffraction, selected-area diffraction patterns, transmission electron microscopy, photoemission or x-ray absorption to determine whether the magnetic atoms are substituting for one of the lattice constituents to form an alloy. Given the level of dilution of the magnetic atoms, it is often very difficult to categorically determine the origin of the ferromagnetism. In addition, there are still extreme variations in the reported magnetic behavior with some films exhibiting only Para magnetism and even those with ferromagnetism showing a wide range of apparent

Curie temperatures. In short, the origin of this ferromagnetism is not yet clear and need further analysis.

1.4.3 Spintronic Devices

The successful realization of most spintronics application depends critically on the ability to create spin-polarized charge carriers in a conventional semiconductor device. This can be accomplished under ambient conditions via optical pumping with appropriately polarized laser light. However ultimate device integration will require electrical spin injection. Electrical spin injection can be accomplished either by injecting from a spin-polarized source or by spin-filtering unpolarized carriers at the interface. Despite persistent efforts by many groups, spin injection from a conventional ferromagnetic metal into a semiconductor has proved highly inefficient. In contrast, efficient spin injection has recently been successfully demonstrated in all semiconductor tunnel diode structures either by using a spin polarized dilute magnetic semiconductor as the injector or by using a paramagnetic semiconductor under high magnetic field as a spin filter.

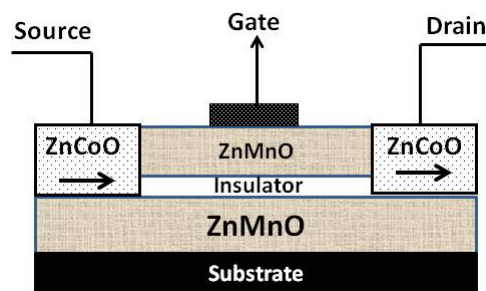


Figure 1.11: Spin FET- Single transistor non volatile memory.

The most effective measurement of the quality of the oxide-based ferromagnetic materials will be in the operation of device structures, such as spin-FETs (figure 1.11), or photo-induced ferromagnets. The use of ferromagnetic semiconductors as the injection source in device structures should allow a more direct measurement of the efficiency and length scale of spin transport. The test structures based on ZnO that will demonstrate how the novel aspects of ferromagnetism that can be exploited in devices. The structure takes advantage of the fact that (Zn, Mn)O can be grown as anti-ferromagnetic spin glass insulator, while Mn-codoped ZnO can be a half metallic ferromagnet. The application of negative gate bias brings holes into the (Zn, Mn)O and converts it to the half-metallic ferromagnetic state. Using ferromagnetic (Zn, Co)O as the source and drain contact material, it should be possible to have a 100% spin polarized electron flow in the (Zn, Mn)O channel. The device can be fabricated by growing the source/drain materials on top of the (Zn, Mn)O and then etching away in the gate region for selective growth of the gate oxide and deposition of the gate metal.

1.5 Statement of research problems

The literature review point out the current status of the ZnO and TM doped ZnO in optoelectronics and spintronics. A large number of groups synthesize and characterize the ZnO and ZnO:TM thin films and nanostructures by various methods. The single phase of the DMS material without impurity or secondary phases is confirmed by material characterization techniques. In the magnetic point of view we can incorporate few atomic percentages of TM but exceeding the solubility limit produce secondary

phases. So the realization of room temperature spintronic devices need single phase TM doped ZnO thin films and nanostructures.

The main objective of the present study is the growth of single phase $\text{Zn}_{1-x}\text{TM}_x\text{O}$ thin films by PLD and increase the solubility limit of TM dopants. The TM doped ZnO nanostructures were also grown by hydrothermal method. The structural and morphological variation of ZnO:TM thin films and nanostructures with TM doping concentration is also investigated. The origin and enhancement of ferromagnetism in single phase $\text{Zn}_{1-x}\text{TM}_x\text{O}$ thin films and nanostructures using spectroscopic techniques were also studied. The dependence of ablation parameters on the structural and optical properties of ZnO thin films were also studied.

Chapter 2

Experimental techniques and characterization tools

2.1 Introduction

Ferromagnetic materials show a complex hierarchy of microstructures over several length scales, which range from a few nanometers to the sample size. Understanding of the formation of such structures and their interaction with external fields has a large technological relevance. The discovery of ferromagnetic ordering at temperature as high as 110 K in the diluted magnetic semiconductor (DMS) (Ga, Mn)As [31] has inspired intensive research on the room temperature ferromagnetic DMSs [60], which are expected to play an important role in spintronics [61]. In addition to the III-V based DMSs, oxide semiconductors such as ZnO [34] and TiO₂ [62], have also been intensively studied due to their unique properties. Transparent magnets may be obtained by doping these wide-gap oxide semiconductors. The quality of the samples depends sensitively on the preparation methods

and the growth conditions.

Understanding the different mechanisms affecting the growth mode is therefore necessary to control the surface morphology during thin film growth. A variety of deposition techniques have been employed to deposit transparent conducting oxides. The electrical and optical properties of these films depend strongly on their microstructure and stoichiometry and the nature of the impurities present. Each deposition technique with its associated parameters yields films of different properties. Different thin film technologies like chemical vapor deposition (CVD) [54], pulsed laser deposition (PLD) [25, 63], sputtering [64], sol-gel [27], chemical bath deposition and molecular beam epitaxy [65, 66] can be used for the preparation of transparent conducting oxides. Because of its versatility and ability to provide epitaxial and stoichiometric films, pulsed laser deposition (PLD) technique is one of the most suitable thin film technologies for the deposition of transparent conducting oxides like ZnO and its alloys. In the present work TM doped ZnO films were prepared using pulsed laser deposition technique. The targets used for the laser ablation were prepared by solid state reaction of the constituent powders at high temperature. The thin films of $\text{Zn}_{1-x}\text{TM}_x\text{O}$ grown on quartz, *c*- Al_2O_3 (0001) substrate by the PLD technique were used for optical and magnetic studies.

The nanostructures can be prepared by numerous physical and chemical techniques however the final product is dictated by the kinetics of thermodynamics of systems. There are basically two broad areas of synthesis techniques for nanostructured materials namely physical methods and chemical methods. The hydrothermal processing is a non conversional method to obtain nanocrystalline inorganic materials. The hydrothermal

technique is becoming one of the cost effective tools for advanced materials processing, particularly owing to its advantages in the processing of nanostructure materials for a wide variety of technological applications such as electronics, optoelectronics, catalysis, ceramics, magnetic data storage, biomedical, biophotonics, etc. The hydrothermal technique not only helps in processing monodispersed and highly homogeneous nanoparticles, but also acts as one of the most attractive techniques for processing nanohybrid and nanocomposite materials.

2.2 Experimental techniques for the growth of thin films and nanostructures

2.2.1 Pulsed laser deposition (PLD)

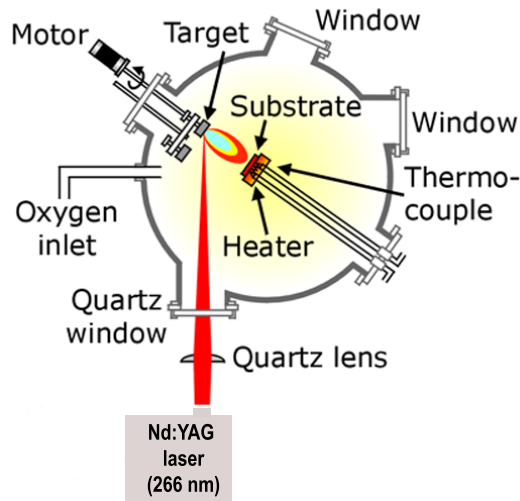


Figure 2.1: Schematic diagram of the PLD setup used for the present investigation.

PLD systems have three main components: laser, deposition system, and the optics between the two. Usually any type of laser can be used in a PLD system if the power of the output laser beam is high enough. In the present study, the fourth (266 nm) harmonic of an Nd:YAG laser (Spectra Physics - Quanta Ray) and a (248 nm) KrF excimer laser (Laser Physik - Compax Pro) are used for ablation. Figure 2.1 shows a schematic diagram of a pulsed laser deposition system. In a PLD system, thin films are grown under high vacuum. Usually a vacuum of the order of 0.5 to 10^{-6} mbar is used during

the deposition of the thin film. One of the advantages of PLD is that it requires very simple and relatively economical pump and gas flow systems. The basic elements inside the vacuum chamber include substrate holder, targets holder, vacuum gauges, etc. Compared to other thin film growth methods, crystalline films can be grown at lower substrate temperature in PLD technique. For all the PLD system, the optical elements are needed to be direct and focus the beam for ablating the target material. These optical elements, such as mirror, beam splitter, and lens are placed between the output port of the laser and the laser window of the vacuum chamber.

While the basic set up is simple relative to many other deposition technique, the physical phenomena of laser target interaction and film growth are quite complex . When the laser pulse is absorbed by the target, energy is first converted into electronic excitation and then into thermal, chemical and mechanical energy resulting in evaporation, ablation, plasma formation and even exfoliation. The ejected species expand into the surrounding vacuum in the form of a plume containing many energetic species including atoms, molecules, electrons, ions, clusters, particulates and molten globules before depositing on the hot substrates placed at a short distance from the targets. Unlike thermal evaporation, which produces a vapor composition dependent on the vapor pressure of the elements in the target material, the laser induced expulsion produces a plume of the material with a stoichiometry similar to the target. During the ablation process, within a few picoseconds, the energy from the laser pulse is transferred to the crystal lattice and a thermal equilibrium is attained in the system. Typical transient plasma temperature measured by emission spectroscopy during the initial expansion from the small region is $\sim 10,000\text{K}$, which is well above

the boiling point of most of the materials. This high temperature is sufficient to evaporate the surface layer of the target thereby producing exact composition on the thin films.

Mechanism of PLD

The mechanism of pulsed laser deposition, in contrast to the simplicity of the set up, is very complex physical phenomenon. In PLD technique, the target materials are ablated into a plasma plume by a focused intense laser beam. The focused laser pulses are absorbed in the target surface in a small volume. The absorbed energy density is sufficient to break any chemical bonds of the molecules within the volume. What essentially happens is that high-pressure gas is produced in the surface layer. As a result of the pressure gradient, a supersonic jet of particles is ejected normal to the target surface. In practice, the process is far more complicated. The particle cloud absorbs a large amount of energy from the laser beam producing an expansion of hot plasma (plume). The ablated species condense on the substrate placed opposite to the target forming a thin film after some hundreds or thousands of laser pulses. Momentum is conserved in the impact event and the plasma and debris must have an overall azimuthal momentum that is sensitive to the original momentum, which, for light, is essentially insignificant. Thus, there is no reason why the debris from the impact should have an overall 'direction' that is co-linear with the direction of the inbound laser pulse. Therefore, the interaction of intense laser with matter plays an important role in PLD process. The plume behaves in a different manner in vacuum and in the presence of an ambient background gas. In vacuum, the plume does not expand unidirectionally but backward velocity components appear as well because of the high density of the plasma. The

ejected species diffuse in the plume and collide with each other, which leads to a rapid thermalization of the particle cloud. Moreover, the plume in vacuum is visible only in the immediate vicinity of the target. Ambient oxygen scatters and attenuates the plume, changing its spatial distribution, the deposition rate, and the kinetic energy distribution of the different species. In addition, reactive scattering results in the formation of molecules or clusters which are essential for the proper stoichiometry and oxygen content of the film.

The sputtering mechanisms responsible for the PLD processes can be classified as primary sputtering mechanisms and secondary sputtering mechanisms [40, 53]. The primary sputtering includes collision sputtering, thermal sputtering, electronic sputtering, exfoliation sputtering, and hydrodynamic sputtering. The secondary sputtering can be distinguished as outflow with reflection, outflow with recondensation, effusion with reflection, and effusion with recondensation.

Primary Sputtering:

Primary sputtering results in particle emission which occurs when the solid surface is bombarded with pulsed photons.

1. **Collision sputtering:** In collision sputtering, the target material is removed as particles from the target surface through momentum transformation from the incident particles to the particles that are removed. The direct collision effect can not happen in PLD process because of the small momentum of photons. However, indirect collision effect does exist in PLD process, in which the particles of target material are removed through the collision effect between laser-induced

plasma and the target material. Ions in the plasma are accelerated to as much as 100-1000 eV.

2. **Thermal sputtering:** Thermal sputtering is the vaporization from a transiently heated target, which requires a temperature well above the melting or boiling points. This occurs as a result of intense laser absorption.
3. **Electronic sputtering:** Electronic sputtering is not a unique process but rather a group of processes that have the common feature of excitation. It occurs due to the events such as ion explosions, the hole-pair mechanism or surface plasmon excitation. For high laser-pulse energy, high density of electrons is excited, $n_e \approx 10^{22} \text{ cm}^{-3}$. These dense electrons will increase the total energy of each atom by an amount of $\sim n_e E_{gap} / n_c$, E_{gap} is band gap, n_c is the number of atoms per unit volume. So the energy of each atom increases by $\sim 2\text{eV}$ and it will raise the vapor pressure or breaks the lattice bond. Thus the system makes a transition from a tightly bound solid to a densely packed, repulsive gas, and particles are expelled energetically.
4. **Exfoliation sputtering:** Exfoliation sputtering occurs when the target is subjected to repeated thermal shocks, then the flakes of the target materials detach from the target. This effect is expected to occur when the target has a high linear thermal expansion or a high Young's modulus.

Secondary Sputtering:

The secondary mechanisms include various types of pulsed flow processes that differ both depending on whether the release is from the surface or from a reservoir, and also depending on whether the particles that are backscattered toward the surface are reflected or absorbed. When the density of the emitted particles is small enough, the particles escape without interaction. These particles go into free flight with velocity distribution that is appropriate to the primary sputtering mechanisms. As the density becomes large enough, the emitted particles exhibit prominent gas-dynamic effects due to the gas-phase collisions. First of all, an unsteady adiabatic expansion may occur, which is similar to the case where wall is removed from a gas reservoir. This was termed as outflow model. Whether the particles backscattered toward the target surface are reflected or absorbed leads to two types of outflows, outflow with reflection and outflow with recondensation. If collisions among the emitted particles are sufficient, equilibrium can be achieved within a few mean free paths in a thin region that is called Knudsen layer (KL). An unsteady adiabatic expansion process coupled with Knudsen layer leads to another possible expansion model, which is called effusion. The backscattering of the particles toward to the target surface leads two types of effusion, the one with reflection and the one recondensation [54].

The nucleation process depends on the interfacial energies between the three phases present - substrate, the condensing material and the vapor. The growth of crystalline films depends on many factors such as the density, energy, ionization degree, and the type of the condensing material, as well as the temperature and the physico-chemical properties of the substrate.

The minimum-energy shape of a nucleus is like a cap. The critical size of the nucleus depending on the driving force, i.e. the deposition rate and the substrate temperature. For the large nuclei, a characteristic of small supersaturation, they create isolate patches (islands) of the film on the substrate which subsequently grow and coalesce together. As the supersaturation increases, the critical nucleus shrinks until its height reaches on atomic diameter and its shape is that of a two-dimensional layer. For large supersaturation, the layer by layer nucleation will happen for incompletely wetted foreign substrates. The crystalline film growth depends on the surface mobility of the adatom (vapour atoms). Normally, the adatom will diffuse through several atomic distances before sticking to a stable position within the newly formed film. The surface temperature of the substrate determines the adatom's surface diffusion ability. High temperature favours rapid and defect free crystal growth, whereas low temperature or large supersaturation crystal growth may be overwhelmed by energetic particle impingement, resulting in disordered or even amorphous structures. The two main thermodynamic parameters for the growth mechanism are the substrate temperature T and the supersaturation D_m . They can be related by the following equation

$$D_m = kT \ln(R/R_e) \quad (2.1)$$

where k is the Boltzmann constant, R is the actual deposition rate, and R_e is the equilibrium value at the temperature T .

In the PLD process, due to the short laser pulse duration (~ 10 ns) and hence the small temporal spread (≤ 10 ms) of the ablated materials, the deposition rate can be enormous (~ 10 mm/s). Consequently a layer-by-layer

nucleation is favoured and ultra-thin and smooth film can be produced. In addition the rapid deposition of the energetic ablation species helps to raise the substrate surface temperature. In this respect PLD tends to demand a lower substrate temperature for crystalline film growth.

Advantages of pulsed laser deposition

1. PLD is one of the simpler and versatile method for the deposition of high quality thin films and epitaxial films.
2. It has the ability to operate in the pressure range from ultra high vacuum to low vacuum.
3. It is one of the most cost effective techniques for producing thin films because one laser can serve many vacuum systems.
4. Since the laser source is external to the vacuum chamber, any kind of reactive or inert gases can be used as ambient gas.
5. Relatively high deposition rates can be achieved at moderate laser fluences, with film thickness controlled in real time by simply turning the laser on and off.
6. Using PLD we can deposit many materials that are usually difficult to deposit by other methods, especially multi-element oxides, high temperature superconductors, ferroelectric and electro-optic materials.

Disadvantages of pulsed laser deposition

1. The ablation plume cross section is generally small (in the order of cm) due to a limited laser spot size. This, in turn, limits the sample size that can be prepared by PLD. In addition, this also brings difficulty to controlling thickness uniformity across the sample: This problem can be overcome, to some extent, by scanning the laser beam on a larger area of the target.
2. The plume of ablated material is highly forward directed, which causes poor conformal step coverage. It also makes thickness monitoring difficult.
3. The ablated material contains macroscopic globules of molten material, up to 10 μm diameter. The arrival of these particulates at the substrate is obviously detrimental to the properties of the film being deposited.
4. The fundamental processes that occur within the laser-produced plasma, are not fully understood; thus deposition of novel materials usually involves a period of empirical optimization of deposition parameters.

2.2.2 Hydrothermal Method

The hydrothermal technique not only helps in processing monodispersed and highly homogeneous nanoparticles, but also acts as one of the most attractive techniques for processing nano-hybrid and nanocomposite materials. Hydrothermal processing can be defined as any heterogeneous reaction in the presence of aqueous solvents or mineralizers under high pressure and temperature to dissolve and recrystallize (recover) materials that are

relatively insoluble under ordinary conditions. Hydrothermal is a heterogeneous chemical reaction in the presence of a solvent (whether aqueous or non-aqueous) above the room temperature and at pressure greater than 1 atm in a closed system [67]. Among various technologies available today in advanced materials processing, the hydrothermal technique occupies a unique place owing to its advantages over conventional technologies. This synthesis method uses the solubility in water of almost all inorganic substances at elevated temperature and pressures, and subsequent crystallization of the dissolved material from the fluid. The pressure, temperature, precursor concentration and time of reaction are the principal parameters in hydrothermal processing. The hydrothermal technique offers a unique method for the fabrication of powders or bulk ceramic bodies. In the last decade it has emerged as one of the frontline technologies for the processing of nanomaterials.



Figure 2.2: Hydrothermal furnace and autoclave used for the synthesis of nanostructures.

The hydrothermal processing of advanced materials has lots of advantages and can be used to give high product purity and homogeneity, crystal symmetry, meta stable compounds with unique properties, narrow particle

size distributions. Similarly, the thermodynamic studies yield rich information on the behaviour of solutions with varying pressure temperature conditions. Some of the commonly studied aspects are solubility, stability, yield, dissolution precipitation reactions and so on, under hydrothermal conditions. Hydrothermal crystallization is only one of the areas where our fundamental understanding of hydrothermal kinetics is lacking due to the absence of data related to the intermediate phases forming in solution in the absence of predictive models; we must empirically define the fundamental role of temperature, pressure, precursor, and time on crystallization kinetics of various compounds [68].

Material processing under hydrothermal conditions requires a vessel capable of containing a highly corrosive solvent at high temperature and pressure. Ideal hydrothermal apparatus popularly known as an autoclave should have the following characteristics:

1. Resistant to acids and bases.
2. Sufficient length to obtain a desired temperature gradient.
3. Rugged enough to bear high pressure and temperature experiments for long periods with no damage so that no machining or treatment is needed after each experimental run.

The hydrothermal furnace and autoclave used in the present study for the synthesis of nanostructures are shown in the figure 2.2. The closed containers are placed into the sealed stainless steel autoclaves and put into the furnace. Applying the desired hydrothermal synthesis temperature, an autogenous pressure is formed. The external pressure is adjusted as soon as the temperature equilibrium is achieved within the autoclave. By

the installation of the hydrothermal pressure, the reaction process takes place. Temperature fluctuations of the furnace have negative consequences because a rise in the temperature leads to a higher dissolution rate disturbing the dynamic equilibrium of dissolution-crystallization, while lowering of temperature leads to higher supersaturation.

2.3 Characterization tools

2.3.1 Structural characterization

X-ray diffraction

The structural characterization was carried out recording the x-ray diffraction (XRD) pattern of the samples using Rigaku X-ray diffractometer and PANalytical X'Pert PRO with Cu-K α radiation ($\lambda = 1.5418 \text{ \AA}$). XRD is a non destructive technique and can provide information about lattice parameters, orientation of the crystals, phase composition of the sample, grain size etc.

A given substance always produces a characteristic diffraction pattern whether that substance is present in the pure state or as one constituent of a mixture of substances. The particular advantage of X-ray diffraction analysis is that it discloses the presence of a substance, as that substance actually exists in the sample and not in terms of its constituent chemical elements. Diffraction analysis is useful whenever it is necessary to know the state of chemical combination of the elements involved or the particular phase in which they are present. Compared with ordinary chemical analysis the diffraction method has the advantage that it is usually much faster, requires only very small quantity of sample and is non destructive [69].

The basic law involved in the diffraction method of structural analysis is the Bragg's law. When monochromatic beam of x-rays impinge upon the atoms in a crystal lattice, each atom acts as a source of scattering. The crystal acts as series of parallel reflecting planes. The intensity of the reflected beam at certain angles will be maximum when the path difference between two reflected waves from two different crystal planes is an integral multiple of λ . This condition is termed as Bragg's law and is given by

$$2d\sin\theta = n\lambda \quad (2.2)$$

where n is the order of diffraction, λ is the wavelength of the x-rays, d is the spacing between consecutive parallel planes and θ is the glancing angle (or the complement of the angle of incidence) [70].

X-ray diffraction studies give a whole range of information about the crystal structure, orientation, average crystalline size and stress in the films. Experimentally obtained diffraction patterns of the sample are compared with the standard powder diffraction files published by the inorganic crystal structure database (ICSD).

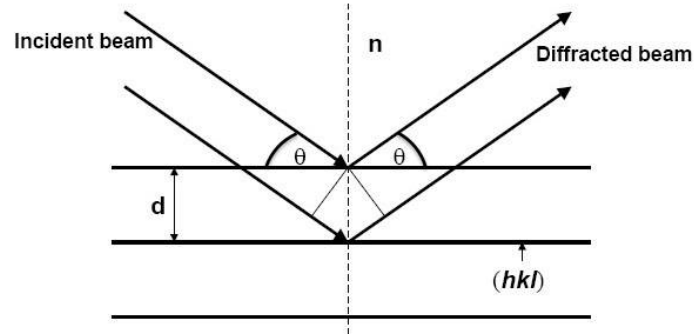


Figure 2.3: Bragg diffraction from a set of planes.

The average grain size of the film can be calculated using the Scherrer's formula 2.3 [69],

$$d = \frac{0.9\lambda}{\beta \cos\theta} \quad (2.3)$$

where, λ is the wavelength of the x-ray and β is the full width at half maximum intensity in radians. The lattice parameter for crystallographic systems in the present study can be calculated from the following equations using the (hkl) parameters and the interplanar spacing d.

Cubic system,

$$\frac{1}{d^2} = \frac{h^2 + k^2 + l^2}{a^2} \quad (2.4)$$

Tetragonal system,

$$\frac{1}{d^2} = \frac{h^2 + k^2}{a^2} + \frac{l^2}{c^2} \quad (2.5)$$

Hexagonal system,

$$\frac{1}{d^2} = \frac{4}{3} \left(\frac{h^2 + hk + k^2}{a^2} \right) + \frac{l^2}{c^2} \quad (2.6)$$

2.3.2 Thin film thickness

Thickness is one of the most important thin film parameter to be characterized since it plays an important role in the film properties unlike a bulk material. Microelectronic applications generally require the maintenance of precise and reproducible film metrology (i.e., thickness as well as lateral dimensions). Various techniques are available to characterize the film thickness which are basically divided into optical and mechanical methods, and are usually nondestructive but sometimes destructive in nature. Film thickness may be measured either by in-situ monitoring the rate of deposition or after the film deposition.

The stylus profiler takes measurements electromechanically by moving the sample beneath a diamond tipped stylus. The high precision stage moves the sample according to a user defined scan length, speed and stylus force. The stylus is mechanically coupled to the core of a linear variable differential transformer (LVDT). The stylus moves over the sample surface. Surface variations cause the stylus to be translated vertically. Electrical signals corresponding to the stylus movement are produced as the core position of the LVDT changes. The LVDT scales an ac reference signal proportional to the position change, which in turn is conditioned and converted to a digital format through a high precision, integrating, analog-to-digital converter. The film whose thickness has to be measured is deposited with a region masked. This creates a step on the sample surface. Then the thickness of the sample can be measured accurately by measuring the vertical motion of the stylus over the step. The thicknesses of the thin films prepared for the work presented in this thesis were measured by a stylus profiler (Dektak 6M).

2.3.3 Surface morphology

Surface morphology is an important property while studying nanostructures. Characterization tools used to study the surface morphology of the nanostructures is described below.

i) Atomic force microscopy

Following the invention of the scanning tunneling microscope (STM), a number of new scanning probe microscopes (SPM) has been developed that use the key components of the STM. One of the most important SPM is the atomic force microscope (AFM) [71]. In atomic force microscopy a tip, integrated to the end of a spring cantilever, is brought within the interatomic separations of a surface, such that the atoms of the tip and the surface are influenced by interatomic potentials (fig. 2.4). As the tip is rastered across the surface, it bounces up and down with the contours of the surface. By measuring the displacement of the tip (i.e. the deflection of the cantilever), one can theoretically map out the surface topography with atomic resolution.

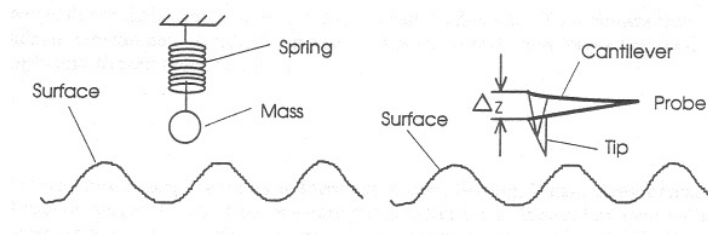


Figure 2.4: Shows how the tip is attached to the cantilever.

The first AFM's cantilever deflections were measured using a piggy-backed STM. Later instruments used more practical optical techniques.

The AFM is essentially identical in concept to the scanning profilometer, except that the deflection-sensitivity and resolution are improved by several orders of magnitude. There are a large number of applications for the AFM, including biological systems, polymers and a host of insulator and semiconductor materials.

An AFM images a surface in a manner analogous to the gramophone stylus sensing the grooves of gramophone disk. The essential elements of an AFM are shown in the figure 2.5. The tip is attached to a cantilever type spring as the tip and sample interact, forces act on the tip and cause the cantilever (spring) to deflect. The cantilever position is monitored by a position detector. The output of the detector is connected to a feedback controller that regulates the force between the sample and the tip by moving the sample up or down. The sample is moved by a PZT scanning actuator. The cantilever must be soft enough to deflect a measurable amount without damaging the surface features of the sample. The amount of deflection is proportional to the force acting on the tip.

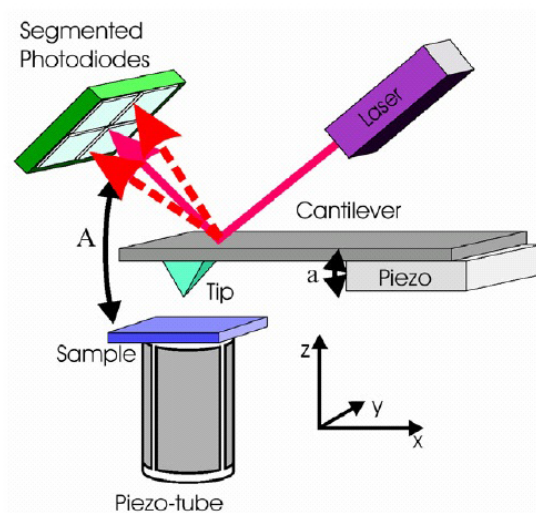


Figure 2.5: The essential elements of an AFM.

Variations of AFM include contact mode, dynamic force mode, phase mode, current image, friction force microscope, magnetic force microscope, surface potential microscope, etc. In the present work, Agilent 5500 series AFM was used for the morphological study.

1. **Contact Mode:** The most commonly used method in which the tip scans the sample and force on the tip is repulsive with a mean value of 10^{-9} N. This force is set by pushing the cantilever against the sample surface with a piezoelectric positioning element. In contact mode AFM the deflection of the cantilever is sensed and compared in a DC feedback amplifier to some desired value of deflection. If the measured deflection is different from the desired value the feedback amplifier applies a voltage to the piezo to raise or lower the sample relative to the cantilever to restore the desired value of deflection. The

voltage that the feedback amplifier applies to the piezo is a measure of the height of features on the sample surface. The typical problem with the contact mode is that the tip may scratch the surface and change its intrinsic features

2. **Non-Contact Mode:** In this mode the tip is held at 50 - 150 Å above the sample surface. Attractive Van der Waals forces acting between the tip and the sample are detected, and topographic images are constructed by scanning the tip above the surface. Since the attractive forces from the sample are substantially weaker than the forces used by contact mode therefore the tip is given a small oscillation so that AC detection methods can be used to detect the small forces between the tip and the sample by measuring the change in amplitude, phase, or frequency of the oscillating cantilever in response to force gradients from the sample. For highest resolution, it is necessary to measure force gradients from Vander Waals forces which may extend only a nanometer from the sample surface.
3. **Semi-Contact Mode:** Semicontact mode was developed as a method to achieve high resolution without including destructive frictional forces both in air and liquid. In this mode, the cantilever is made to oscillate at its natural frequency by using a piezo-electric crystal. The oscillating tip is moved close to the sample surface till it begins to just tap it and is then immediately lifted off again, while the sample is continuously scanned below the tip. The change in oscillation amplitude during the tapping period is used as a feedback to maintain constant height or force between the tip and the sample. The

feedback voltage serves as a measure of the surface features. The advantages of the semi-contact mode are that as the tip is not dragged over the sample there is no damage caused to the sample and also the tip is prevented from sticking to the sample surface due to adhesion. This method usually gives higher resolution than the previous two methods. With the semicontact mode, the very soft and fragile samples can be imaged successfully

ii) Scanning electron microscope (SEM)

The scanning electron microscope (SEM) is a microscope that uses electrons rather than light to form an image. The SEM has a large depth of field, which allows a large amount of the sample to be in focus at the same time. The SEM also produces images of high resolution, which means that closely spaced features can be examined at a high magnification. Preparation of the samples is relatively easy since most SEMs only require that sample should be conductive. The combination of higher magnification, larger depth of focus, greater resolution, and ease of sample observation makes SEM one of the most heavily used instruments in the research field. The electron beam comes from a filament, made of various types of materials. The most common is the Tungsten hairpin gun. This filament is a loop of tungsten that functions as the cathode. A voltage is applied to the loop, causing it to heat up. The anode, which is positive with respect to the filament, forms powerful attractive forces for electrons. This causes electrons to accelerate toward the anode. The anode is arranged, as an orifice through which electrons would pass down to the column where the sample is held. Other examples of filaments are lanthanum hexaboride filaments and field emission guns. The image in an SEM is produced by scanning

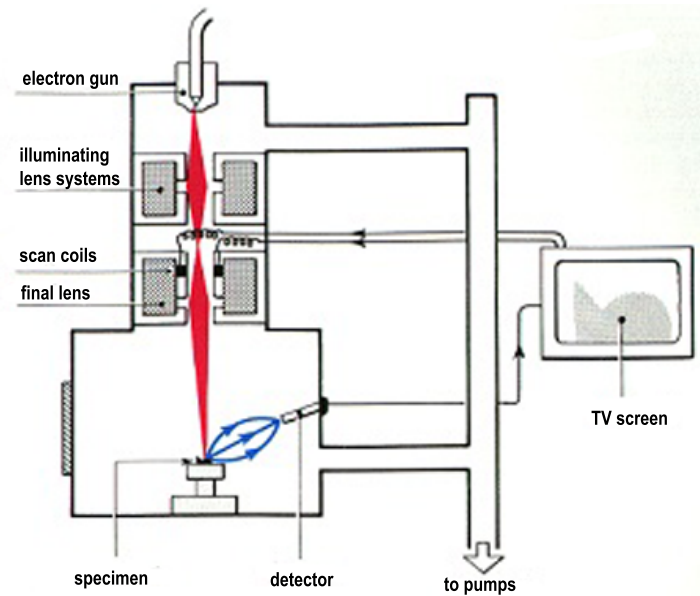


Figure 2.6: Schematic diagram of scanning electron microscope.

the sample with a focused electron beam and detecting the secondary and backscattered electrons.

Schematic diagram of a scanning electron microscope is shown in figure 2.6. The streams of electrons that are attracted through the anode are made to pass through a condenser lens, and are focused to very fine point on the sample by the objective lens. The electron beam hits the sample, producing secondary electrons from the sample. These electrons are collected by a secondary detector or a backscatter detector, converted to a voltage, and amplified. The amplified voltage is applied to the grid of the CRT that causes the intensity of the spot of light to change. Electrons and photons are emitted at each beam location and subsequently detected. Secondary images form the conventional SEM image. Emitted light is known

as cathodoluminescence and absorbed electrons are detected and amplified to control the brightness of a cathode ray tube (CRT) or television scanned with the sample beam scan in SEM. The image consists of thousands of spots of varying intensity on the face of a CRT that correspond to the topography of the sample. In the present thesis, JEOL JSM-5600 was used for SEM analysis.

2.3.4 Compositional Analysis

i) X-ray photoelectron spectroscopy (XPS)

X-ray photoelectron spectroscopy (XPS) is a quantitative spectroscopic technique that measures the elemental composition, empirical formula, chemical state and electronic state of the elements that exist within a material. XPS spectra are obtained by irradiating a material with a beam of X-rays while simultaneously measuring the kinetic energy and number of electrons that escape from the top 1 to 10 nm of the material being analyzed (fig.2.7). XPS requires ultra-high vacuum (UHV) conditions.

XPS is a surface chemical analysis technique that can be used to analyze the surface chemistry of a material in its "as received" state, or after some treatment, for example: fracturing, cutting or scraping in air or UHV to expose the bulk chemistry, ion beam etching to clean off some of the surface contamination, exposure to heat to study the changes due to heating, exposure to reactive gases or solutions, exposure to ion beam implant, exposure to ultraviolet light. The main features of the XPS are

1. XPS detects all elements with an atomic number (Z) of 3 (lithium) and above.

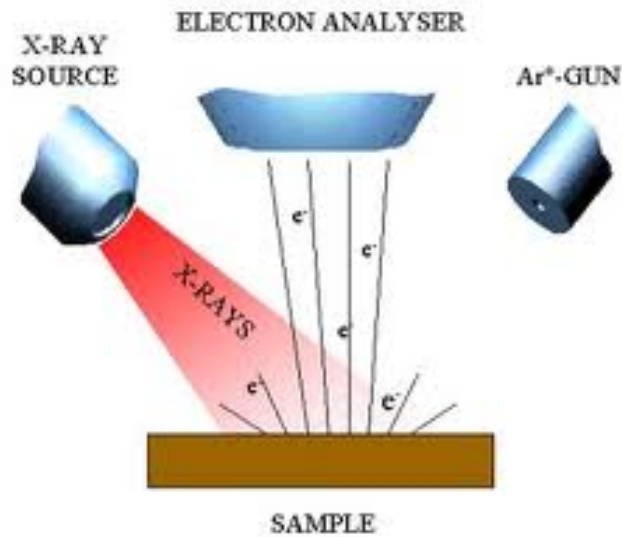


Figure 2.7: Schematic diagram of XPS.

2. Detection limits for most of the elements are in the parts per thousand range.
3. XPS is routinely used to analyze inorganic compounds, metal alloys, semiconductors, polymers, elements, catalysts, glasses, ceramics.
4. Uniformity of elemental composition across the top surface (or line profiling or mapping).

ii) Energy dispersive x-ray analysis (EDAX)

EDAX is a technique used for identifying the elemental composition of the specimen, on an area of interest thereof. During EDAX analysis, the specimen is bombarded with an electron beam inside the scanning electron microscope [40, 65]. The bombarding electrons collide with the specimen

atom's own electrons, knocking some of them off in the process. A position vacated by an ejected inner shell electron is eventually occupied by a higher-energy electron from an outer shell. To be able to do so, however, the transferring outer electron must give up some of its energy by emitting an x-ray. This amount of energy is predicted by the laws of quantum mechanics. The x-ray detector in the EDAX is reverse biased semiconductor pin or Schottky diode.

$$I(x) = I_0 \exp\left[-\frac{\mu}{\rho}\right] \rho x \quad (2.7)$$

where (μ/ρ) is the mass absorption coefficient, ρ the detector material density, $I(x)$ the x-ray intensity in the detector and I_0 is the incident x-ray intensity. The mass absorption coefficient is characteristic of a given element at specified x-ray energies and it varies with atomic number of the target. Thus, by measuring the energy of the x-rays emitted by a specimen during electron beam bombardment, the identity of the atom from which the x-ray was emitted can be established. The output of an EDAX analysis is an EDAX spectrum, which is a plot of how frequently x-ray is received for each energy level. The higher a peak in a spectrum, the more concentrated the element is in the specimen. An EDAX spectrum plot not only identifies the element corresponding to each of its peaks, but the type of x-ray to which it corresponds as well. Elements from Na to U can be detected with EDAX. In this work the compositional analysis were carried out using JEOL JSM-5600 SEM.

iii) Electron Paramagnetic Resonance

Electron paramagnetic resonance (EPR), also known as electron spin resonance (ESR) and electron magnetic resonance (EMR), is the name given to the process of resonant absorption of microwave radiation by paramagnetic ions or molecules, with at least one unpaired electron spin, and in the presence of a static magnetic field. EPR was discovered by Zavoisky in 1944. EPR is a spectroscopic technique that detects chemical species that have unpaired electrons. A great number of materials contain such paramagnetic entities, which may occur either as electrons in unfilled conduction bands, electrons trapped in radiation damaged sites, or as free radicals, various transition ions, bi-radicals, triplet states, impurities in semi-conductors, as well as other types. It has a wide range of applications in chemistry, physics, biology, and medicine: it may be used to probe the 'static' structure of solid and liquid systems, and is also very useful in investigating dynamic processes. One of the fundamental roles of any spectroscopic technique is identification of the chemical species being studied. In cases where two or more paramagnetic species co-exist, the spectral EPR lines arising from each can be simultaneously observed. Often definitive identification of the individual species is realized solely from the analysis of the EPR spectrum.

Furthermore, EPR spectroscopy is capable of providing molecular structural details inaccessible by any other analytical tool. These capabilities of EPR are a result of the unpaired electron's spin magnetic moment being very sensitive to local magnetic fields within the sample. EPR has been successfully applied in such diverse disciplines as biology, physics, geology, chemistry, medical science, material science, anthropology, to name but a few. Solids, liquids and gases are all accessible to EPR. By utilizing a vari-

ety of specialized techniques (such as spin-trapping, spin-labeling, electron spin echo envelope modulation (ESEEM), researchers are capable of obtaining detailed information of the materials. EPR remains one of the most sensitive windows into the chemical (i.e., electronic) nature of matter, being able to detect and identify spins with concentrations in the 10^{-9} region. In practice, limits of detection are usually somewhat less than this, due to line-width effects. Absolute concentrations of spin species are possible to determine using EPR, but because of the great number experimental parameters that must be taken into account, relative concentrations of species simultaneously present are more easily obtained.

How does EPR work? By application of a strong magnetic field B to material containing paramagnetic species, the individual magnetic moment arising via the electron 'spin' of the unpaired electron can be oriented either parallel or anti-parallel to the applied field [72]. This creates distinct energy levels for the unpaired electrons, making it possible for net absorption of electromagnetic radiation (in the form of microwaves) to occur. The situation referred to as the resonance condition takes place when the magnetic field and the microwave frequency are 'just right' (i.e., the energy of the microwaves corresponds to the energy difference ΔE of the pair of involved spin states).

Allowed EPR transitions occur when $|dM_s|=1$ (M_s is the magnetic spin quantum number of the spin state) and is shown in figure 2.8. The equation describing the absorption (or emission) of microwave energy between two spin states is $\Delta E = h\nu = g\beta B$, where ΔE is the energy difference between the two spin states, h is Planck constant, ν is the microwave frequency, g is the Zeeman splitting factor, β is the Bohr magneton, B is the applied magnetic field.

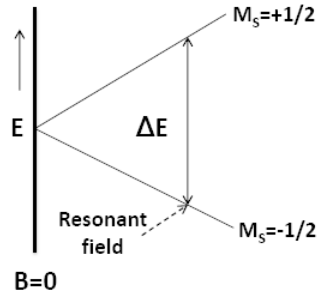


Figure 2.8: Energy-level diagram for two spin states as a function of applied field B.

2.3.5 Optical studies

i) Transmission spectroscopy

The band gap of a semiconductor is measured by studying the absorption of incident photons by the material. Here the photons of selected energy are directed to the sample and the relative transmission of the various photons is observed. Since photons with energies greater than the band gap energy are absorbed while photons with energies less than band gap energy are transmitted, the experiment gives an accurate measure of band gap [73, 74]. According to Bardeen et al. [75] for the parabolic band structure, the relation between the absorption coefficient (α) and the band gap E_g of the material is given by,

$$\alpha = \left[\frac{A}{h\nu} \right] (h\nu - E_g)^N \quad (2.8)$$

where, $N = 1/2$ for allowed direct transitions, $N = 2$ for allowed indirect transitions. A is the parameter which depends on the transition proba-

bility. The absorption coefficient can be deduced from the absorption or transmission spectra using the relation,

$$I = I_0 e^{-(\alpha)t} \quad (2.9)$$

where, I is the transmitted intensity and I_0 is the incident intensity of the light and t is the thickness of the film. In the case of direct transition, $(\alpha h\nu)^2$ will show a linear dependence on the photon energy ($h\nu$). A plot of $(\alpha h\nu)^2$ against $h\nu$ will be a straight line and the intercept on energy axis at $(\alpha h\nu)^2$ equal to zero will give the band gap. The transmission spectra of the thin film samples were recorded using JASCO V-570 spectrophotometer in the present studies.

ii) Diffuse reflectance spectroscopy

Diffuse reflectance spectrometry concerns one of the two components of reflected radiation from an irradiated sample, namely specular reflected radiation, R_s and diffusely reflected radiation, R_d . The former component is due to the reflection at the surface of single crystallites while the latter arises from the radiation penetrating into the interior of the solid and re-emerging to the surface after being scattered numerous times. These spectra can exhibit both absorbance and reflectance features due to contributions from transmission, internal and specular reflectance components as well as scattering phenomena in the collected radiation. Based on the optical properties of the sample, several models have been proposed to describe the diffuse reflectance phenomena. The model put forward by Kubelka-Munk in 1931 is widely used and accepted in diffuse reflectance infrared spectrometry. The intensity of the reflected light depends on the

scattering coefficient s and the absorption coefficient k . The reflectance data can be converted to absorbance by Kubelka-Munk equation [68, 76]. Kubelka-Munk equation is as

$$\text{Log}\left[\frac{1-r}{2r}\right] = \text{Log}k - \text{Log}s \quad (2.10)$$

Where $r = \frac{R(\text{sample})}{R(\text{standard})}$

Here the standard used is BaSO_4 . $R(\text{standard})$ is taken as unity. $R(\text{sample})$ is the diffuse reflectance of the sample

($R = I_{\text{sam}}/I_{\text{ref}}$).

Equation 2.10 Implies,

$$\frac{(1-R)^2}{2R} = \frac{k}{s} \quad (2.11)$$

The band gap is estimated from the plot of $((k/s)h\nu)^2$ vs $h\nu$ ($h\nu$ is the photon energy) by extrapolating the graph to the x-axis. DRS was recorded using JASCO V-570 spectrophotometer in the present study.

iii) Photoluminescence (PL)

Luminescence in solids is the phenomenon in which electronic states of solids are excited by photons from an external source and the excited states release energy as electromagnetic radiation. When short wavelength radiation illuminate a solid and results in the emission of higher wavelength, the phenomenon is called photoluminescence (PL). PL is divided into two major types: Intrinsic and extrinsic depending on the nature of electronic transition producing it.

Intrinsic luminescence are of three kinds

1. **Band to band luminescence:** Luminescence owing to the band-to-band transition, ie to the recombination of an electron in the conduction band with a hole in the valance band, can be seen in pure crystal at relatively high temperature. This has been observed in Si, Ge and IIIb-Vb compounds such as GaAs.
2. **Exciton luminescence:** An exciton is a composite particle of an excited electron and a hole interacting with one another. It moves in a crystal conveying energy and produces luminescence owing to the recombination of the electron and the hole. There are two kinds of excitons: Wannier exciton and Frenkel exciton. The Wannier exciton model express an exciton composed of an electron in the conduction band and a hole in the valence band bound together by Coulomb interaction.
3. **Extrinsic luminescence:** Luminescence caused by intentionally incorporated impurities, mostly metallic impurities or defects is classified as extrinsic luminescence. Most of the practical application belongs to this category. Intentionally incorporated impurities are activators and materials made luminescent in this way are called phosphors.

The emission spectra for the powder and thin film samples were recorded using LAB RAM spectrophotometer (HORIBA JOBIN YVON) with an excitation wavelength of 325 nm.

iv) Raman spectroscopy

Raman spectroscopy is a spectroscopic technique used to study vibrational, rotational, and other low-frequency modes in a system [77]. It relies on

inelastic scattering or Raman scattering of monochromatic light, usually from a laser in the visible, near infrared or near ultraviolet range. The laser light interacts with molecular vibrations, phonons or other excitations in the system, resulting in the energy of the laser photons being shifted up or down. If the final vibrational state of the molecule is more energetic than the initial state, then the emitted photon will be shifted to a lower frequency in order for the total energy of the system to remain balanced. This shift in frequency is designated as a Stokes shift. If the final vibrational state is less energetic than the initial state, then the emitted photon will be shifted to a higher frequency, and this is designated as an anti-Stokes shift. Infrared spectroscopy yields similar, but complementary, information. Typically, a sample is illuminated with a laser beam. Light from the illuminated spot is collected with a lens and sent through a monochromator. Wavelengths close to the laser line, due to elastic Rayleigh scattering, are filtered out while the rest of the collected light is dispersed onto a detector. For the spontaneous Raman effect, which is a form of scattering, a photon excites the molecule from the ground state to a virtual energy state. When the molecule relaxes it emits a photon and it returns to a different rotational or vibrational state. The difference in energy between the original state and this new state leads to a shift in the emitted photon's frequency away from the excitation wavelength. The Raman effect, which is a light scattering phenomenon, should not be confused with absorption (as with fluorescence) where the molecule is excited to a discrete (not virtual) energy level.

Spontaneous Raman scattering is typically very weak, and as a result the main difficulty of Raman spectroscopy is separating the weak inelastically scattered light from the intense Rayleigh scattered laser light. Historically, Raman spectrometers used holographic gratings and multiple dis-

persion stages to achieve a high degree of laser rejection. In the past, photomultipliers were the detectors of choice for dispersive Raman setups, which resulted in long acquisition times. However, modern instrumentation almost universally employs notch or edge filters for laser rejection and spectrographs (either axial transmissive (AT), Czerny-Turner (CT) monochromator) or FT (Fourier transform spectroscopy based), and CCD detectors.

The information about structure, phase, grain size, phonon confinement etc can be obtained from Raman spectroscopy. The extend of phonon confinement in a material can be observed as the shift in Raman line frequencies. Acoustic modes are not observed by Raman measurements in bulk systems because of their low frequencies. But in nanostructured materials, they appear in the measurable frequency range (below 100 cm^{-1}) [73, 78]. Confinement of optical phonons results in the frequency shift and asymmetrical broadening of longitudinal optical (LO) and transverse optical (TO) mode line shape [74]. The information about the structure and quality of the low dimensional structures can be obtained from Raman spectroscopy.

In the present work, Raman studies were carried out with Lab RAM HR spectrophotometer (HORIBA JOBIN YVON) with Ar ion laser (514.5 nm) as the excitation source.

2.3.6 Magnetic studies

i) SQUID Magnetometer

SQUID magnetometer is the instrument used to measure extremely sensitive magnetic fields of the order of 10^{-14} T. It consists of a superconducting ring interrupted with either one or two Josephson junctions (fig. 2.9). The superconducting quantum interference device (SQUID) consists of two

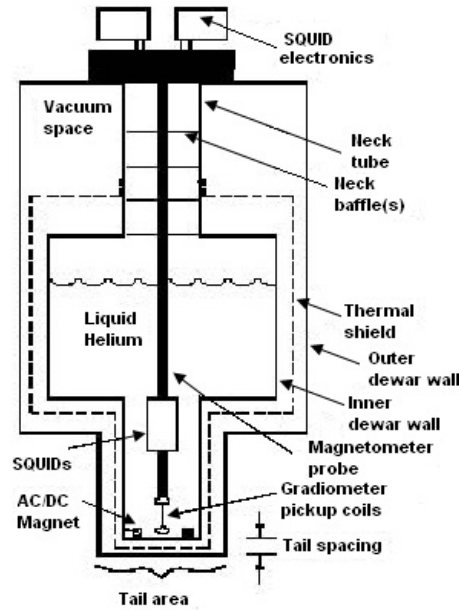


Figure 2.9: Schematic diagram of SQUID magnetometer

superconductors separated by thin insulating layers to form two parallel Josephson junctions. SQUID combine two physical phenomena,

1. Flux quantization: The fact that the flux ϕ in a closed superconducting loop is quantized in the units of ϕ_0 .
2. Josephson tunneling.

The great sensitivity of the SQUID devices is associated with measuring changes in magnetic field associated with one flux quantum ($h/2e$). The basic principle that follows in a SQUID magnetometer is that, if a constant biasing current is maintained in the SQUID device, the measured voltage oscillates with the changes in phase at the two junctions, which depends

upon the change in the magnetic flux. Counting the oscillations allows to evaluate the flux change which has occurred. Hence, when the sample is moved through the superconducting magnetic coils, a flux change is induced in the pick up coils. Highly magnetic sample should be moved slowly through the coils in order not to exceed the maximum slewing rate of the electronic system [76].

Quantum Design SQUID (MPMS XL) magnetometer has been used in present study to measure the magnetic properties and is shown in figure 2.9. The MPMS system comprises of two main sections; SQUID assembly and the electronic control system. The probe contains a high precision temperature control system, allowing measurements from 1.9K to 400K with an accuracy of 0.01K. The superconducting magnet system which provides reversible field operation up to 7 Tesla uses an oscillatory technique to minimize magnetic drift immediately following field changes. The sample handling system (sample translator and sample transport) which allows automatic sample measurements and position calibrations using a microstepping controller having a positioning resolution of 0.0003 cm. The dewar consists of an inner liquid helium reservoir and outer liquid nitrogen jacket, to reduce excessive liquid helium boil off. Liquid helium system provides refrigeration for the superconducting detection system and magnet, as well provides the operation down to 1.9K. Sample is mounted within a plastic straw and connected to one end of a sample rod which is used to position the sample within the center of the SQUID pickup coils. The SQUID detector system includes SQUID amplifier control electronics, sensing pick up loop and specially design filtering with computer control via the interface computer.

ii) Vibrating Sample Magnetometer

The vibrating sample magnetometer has become a widely used instrument for determining magnetic properties of a large variety of materials: diamagnetic, paramagnetic, ferromagnetic and antiferromagnetics. This experimental technique was invented in 1956 by Simon Foner, a scientist of the MIT. EGG Princeton applied research (EGG PAR) was the world leader company that started the commercialization of this magnetometers in the sixties. Vibrating sample magnetometer (VSM) measures the magnetic properties of materials. When a material is placed within a uniform magnetic field and made to undergo sinusoidal motion (i.e. mechanically vibrated), there is some magnetic flux change. This induces a voltage in the pick-up coils, which is proportional to the magnetic moment of the sample. Figure 2.10 shows the vibrating sample magnetometer schematic diagram.

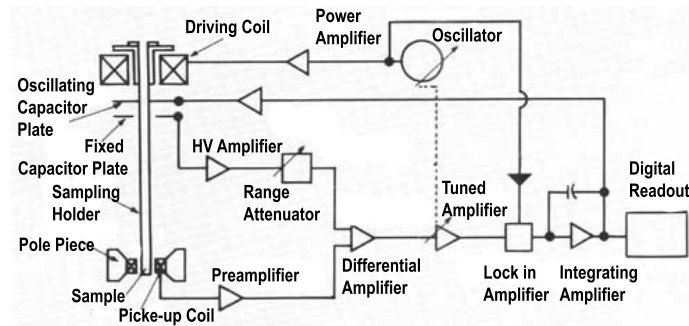


Figure 2.10: Schematic diagram of VSM

If a sample of any material is placed in a uniform magnetic field, created between the poles of a electromagnet, a dipole moment will be induced. If the sample vibrates with sinusoidal motion inducing sinusoidal electrical signal in the pick-up coils. The signal has the same frequency of vibration

and its amplitude will be proportional to the magnetic moment, amplitude, and relative position with respect to the pick-up coil system.

The sample is fixed to a small sample holder located at the end of a sample rod mounted in a electromechanical transducer. The transducer is driven by a power amplifier which itself is driven by an oscillator at a frequency of 90 Hertz. So, the sample vibrates along the Z axis perpendicular to the magnetizing field. The latter induced a signal in the pick-up coil system that is fed to a differential amplifier. The output of the differential amplifier is subsequently fed into a tuned amplifier and an internal lock-in amplifier that receives a reference signal supplied by the oscillator. The output of this lock-in amplifier, or the output of the magnetometer itself, is a DC signal proportional to the magnetic moment of the sample being studied. The electromechanical transducer can move along X, Y and Z directions in order to find the saddle point (which calibration of the vibrating sample magnetometer is done by measuring the signal of a pure Ni standard of known the saturation magnetic moment placed in the saddle point).

Using a vibrating sample magnetometer one can measure the DC magnetic moment as a function of temperature, magnetic field, angle and time. So, it allows to perform susceptibility and magnetization studies. Some of the most common measurements done are: hysteresis loops, susceptibility or saturation magnetization as a function of temperature (thermomagnetic analysis), magnetization curves as a function of angle (anisotropy), and magnetization as a function of time. In the present study magnetization measurements of the bulk and nanostructures were performed using vibrating sample magnetometer (Lakeshore VSM 7410).

Chapter 3

The dependence of structural and optical properties of PLD grown ZnO films on the ablation parameters

3.1 Introduction

ZnO is a wide band gap (3.3 eV) semiconductor with very interesting properties and attracted much attention in the last decades due to its wide variety of applications. Owing to its large exciton binding energy (60 meV) at room temperature, it has potential applications in optoelectronics [79, 80]. ZnO has attracted much interest for blue and ultra-violet (UV) optical devices, such as light-emitting diodes and laser diodes because it has an energy

gap of 3.37 eV at room temperature [2, 79, 81]. It has been commercially used for other applications like: transparent conductive films, solar cell windows and bulk acoustic wave devices etc. Various physical methods have been used for the deposition of ZnO thin films such as thermal evaporation, magnetron sputtering, molecular beam epitaxy (MBE), pulsed laser deposition (PLD), and metal organic chemical vapor deposition (MOCVD) [82–85]. Pulsed laser deposition (PLD) is a powerful technique due to its ability to congruently transfer the stoichiometry from the target to the film [86, 87].

Among the various techniques used for the growth of ZnO thin film, PLD offers the advantages such as deposition at relatively high oxygen pressure and growth of highly oriented crystalline films at low substrate temperature. The high energy of the ejected species allows low substrate temperature during deposition to obtain good crystalline films. The ability of precise control of growth rate of PLD technique is very convenient to grow nanometer size thin films and super-lattice structures. The effect of oxygen pressure on ZnO thin films properties has been investigated by many researchers [11, 88] and found that it is possible to obtain relatively high-quality ZnO thin films by controlling oxygen pressure. There are a markable difference between films deposited at low oxygen pressure and those obtained at high oxygen pressure. The nature of substrate plays an important role in controlling the film properties such as morphology, preferential orientation etc. [20]. The optical transmittance is affected by film thickness, surface roughness, oxygen deficiency and impurity centers [20, 89, 90]. The photoluminescent (PL) spectrum of ZnO thin films have two parts: band edge emission with energy around the band gap of ZnO and defect related deep level emission in the visible range.

This chapter describes the growth of transparent conducting ZnO thin films on quartz, p-silicon (100) and c-Al₂O₃ (0001) substrates by PLD at various substrate temperature (T_S) and oxygen partial pressures (PO_2). The two UV laser sources used for PLD are KrF excimer laser 248 nm (Laser Physik - Compax Pro) with repetition frequency of 10 Hz and Q-switched fourth harmonic Nd:YAG laser (266 nm) with repetition rate of 10 Hz and pulse width of 6-7 ns. The influence of oxygen partial pressure and substrates temperature on the structural, optical and morphological properties of ZnO films were studied.

3.2 Experimental

ZnO target (99.9% purity) prepared by the usual sintering techniques was used for PLD. A focused laser beam (KrF excimer laser 248 nm- Laser Physik - Compax Pro) with repetition frequency of 10 Hz was used for laser ablation. Another set of thin films were prepared using Q-switched fourth harmonic Nd:YAG laser (266 nm) with repetition rate of 10 Hz and pulse width of 6-7 ns. The incident laser fluence was adjusted within the 0.5-1.5 Jcm⁻² range. All the substrates were ultrasonically cleaned and for p-silicon substrates it is further cleaned with HF solution. The thin films were deposited at various T_S from 400 °C to 700 °C. The deposition chamber was initially evacuated to pressures in the 5×10^{-6} mbar and the oxygen partial (PO_2) pressure in the range $0.5-5 \times 10^{-3}$ mbar was used during deposition. The oxygen flow rate were controlled using MKS mass flow controller.

The structural characterization of the ZnO thin films were carried out by PANalytical X'Pert PRO X-ray diffractometer using Cu K α line (1.5418

Å). The thickness of the as prepared thin films were measured by stylus profiler (Dektak 6M). The surface morphology of the thin films was examined by field emission scanning electron microscopy (JEOL Model JSM - 6390LV). The transmission spectra of the films were recorded using UV-vis-NIR spectrophotometer (Jasco-V 570). The photoluminescent and Raman measurements of the ZnO thin films were analyzed by Lab RAM HR spectrophotometer (HORIBA JOBIN YVON). An excitation wavelength of 325 nm for the PL measurements and 514.5 nm for Raman studies were used.

3.3 Results and discussion

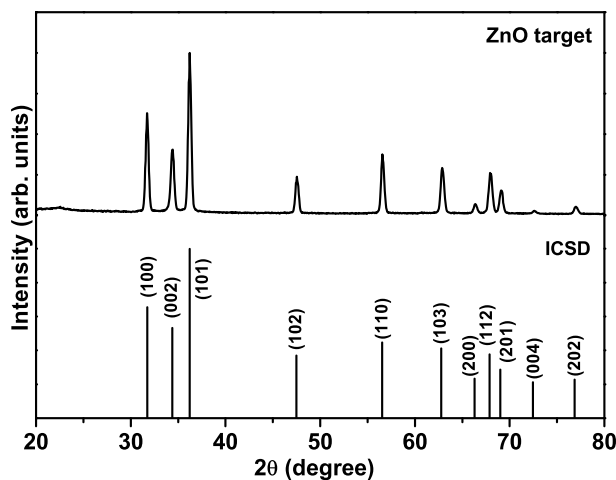


Figure 3.1: XRD pattern of ZnO target.

The phase purity of the target and films have been investigated by x-ray diffraction analysis. The x-ray diffraction pattern of ZnO target having wurtzite hexagonal structure is shown in figure 3.1. The thin films grown by PLD using KrF excimer laser ($\lambda_{ab} = 248$ nm) and Q-switched fourth

harmonic Nd:YAG laser ($\lambda_{ab} = 266$ nm) at different T_S and PO_2 (0.005 mbar) were found to be c-axis oriented, exhibiting only the (002) peak (figure 3.2) in the x-ray diffraction spectra. The PLD of ZnO, laser ablated plume containing various ionic species of zinc and oxygen is expanding adiabatically towards the substrate. Kinetic energy of the zinc and oxygen ionic species reaching the substrate is likely to stimulate the motion of the surface and near surface atoms in the deposited film, thereby relieving film stress, and encouraging changes in film morphology and microcrystalline structure. The discussion thus far has implicitly assumed that adatom adsorption and nucleation occurs homogeneously, and at various sites on the substrate surface. Amorphous films with almost uniform thickness were obtained when the deposition was carried out at room temperature (RT) at a target to substrate distance above 5 cm using KrF excimer laser. But the ablation is carried out using Nd:YAG laser at RT and 0.005 mbar PO_2 we got uniform ZnO film with small diffraction peak (002). Polycrystalline ZnO films oriented in the (002) plane having uniform thickness over 1 cm² area were formed at higher T_S and PO_2 . This type of variation in crystalline nature with substrate to target distance was reported by Cherief *et al.* [91]. Various ionic species of ZnO in the laser ablated plasma plume bombarding the substrate kept at 5 cm distance from the target surface may, have sufficient energy for crystallization to form ZnO films.

The ZnO thin films were grown on quartz, p-Si (100) and c-Al₂O₃ (0001) substrates by PLD technique using KrF excimer laser and fourth harmonic Nd:YAG laser. The x-ray diffraction pattern of ZnO films grown on different substrates at 500 °C T_S and 0.05 mbar PO_2 are shown in figure 3.3. The FWHM of the (002) peak of ZnO thin films grown on quartz substrate is

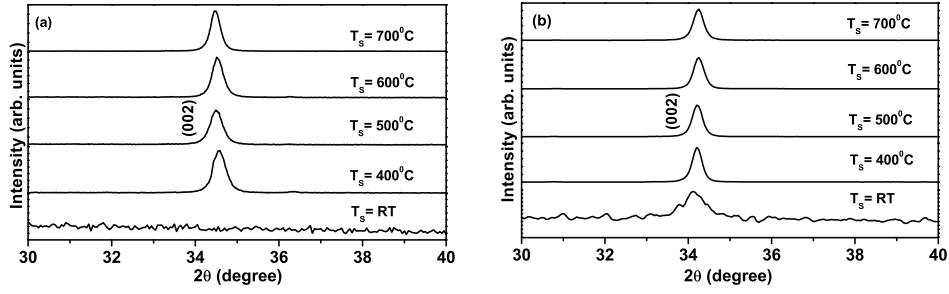


Figure 3.2: X-ray diffraction pattern of ZnO thin films grown by PLD on quartz at different T_S and 0.05 mbar PO_2 using (a) KrF laser ($\lambda_{ab} = 248$ nm) and (b) Nd:YAG laser ($\lambda_{ab} = 266$ nm).

higher than other substrates. The crystallinity of the films enhances with increase of T_S and crystalline nature of the substrates [92, 93].

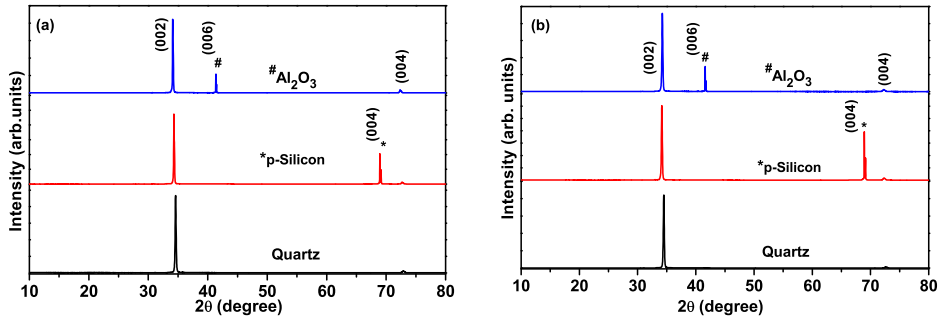


Figure 3.3: X-ray diffraction pattern of ZnO thin films grown on different substrate by PLD at 500 °C T_S and 0.05 mbar PO_2 using (a) KrF laser ($\lambda_{ab} = 248$ nm) and (b) Nd:YAG laser ($\lambda_{ab} = 266$ nm). Substrate peaks are marked as ‘#’ and ‘*’.

The grain size of ZnO films were calculated using Scherrer formula, $t = 0.9\lambda/\beta\cos\theta$. Where ‘ λ ’ is the wavelength of Cu $K\alpha$ radiation, ‘ β ’ is the full width half maximum in radians for a particular peak and ‘ θ ’ the Bragg angle.

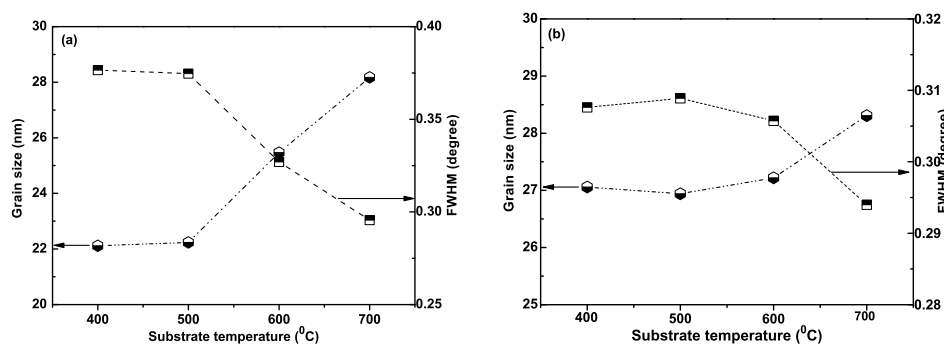


Figure 3.4: The variation of FWHM and grain size of the ZnO films prepared at different T_S and 0.005 mbar PO_2 using (a) KrF laser ($\lambda_{ab} = 248$ nm) and (b) Nd:YAG laser ($\lambda_{ab} = 266$ nm).

The figure 3.4 shows the variation of full width at half maximum (FWHM) and grain size of ZnO films deposited on quartz substrate at different T_S and 0.05 mbar PO_2 . The grain size is found to increase with increase of substrate temperature. The crystallinity is also improved with increase of substrate temperature [93]. Increasing substrate temperature favors the diffusion of atoms absorbed on the substrate and accelerates the migration of atoms to the energy favorable positions, resulting in the enhancement of the crystallinity and c-axis orientation of film, which can be indicated by the increase of (002) peak strength and decrease of FWHM value.

The effect of the substrate temperature and nature on the crystallinity of the ZnO thin films were studied. The effect of PO_2 with grain size of ZnO thin films on various substrates like quartz, p-silicon (100) and c- Al_2O_3 (0001) at $T_S=500$ $^{\circ}\text{C}$ is shown in figure 3.5. The grain size decreases with increases of the PO_2 (0.005 mbar-0.5 mbar) irrespective of the substrate nature at the same temperature. Intrinsic defects such as Zn interstitials and O vacancies, especially at Zn-rich or O-deficient atmosphere leads to non-

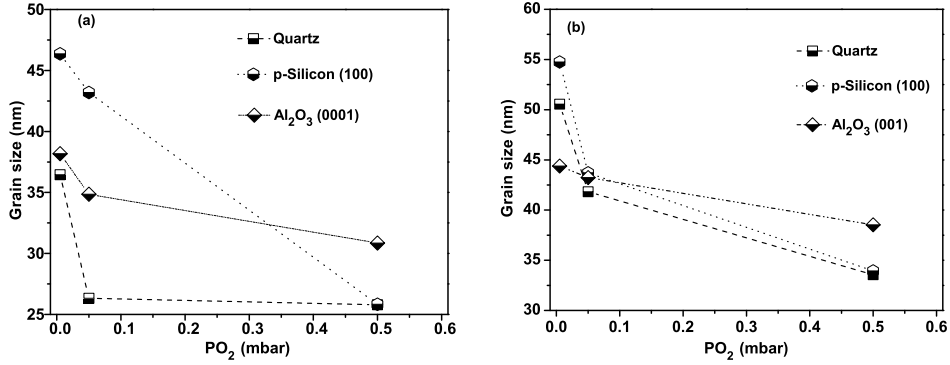


Figure 3.5: The variation of grain size of the ZnO films prepared at $T_S = 500^\circ\text{C}$ and different PO_2 using (a) KrF laser ($\lambda_{ab} = 248 \text{ nm}$) and (b) Nd:YAG laser ($\lambda_{ab} = 266 \text{ nm}$).

stoichiometric ZnO thin films. These intrinsic defects could be decreased by the increase of partial-oxygen pressure, so film with better crystallinity could be obtained at higher oxygen pressure. Above 0.5 mbar PO_2 the films become powdery with observable cluster of grains. The density of the laser created plasma decreases with increase of axial distance from the target to substrate [94], so at higher PO_2 the energy of the emitted particle is very less. Contradictory to this a few groups reported the formation of larger grains at higher PO_2 and lower T_S [95, 96]. At lower substrate temperature and higher ambient pressure the adatoms have lower energy so it favors the growth of larger grains. In our case the substrate temperature provide the necessary energy for the adatoms and we obtained highly crystalline films at high temperature [93, 97] and ambient pressure upto 0.5 mbar. The variation of the grain size with PO_2 at a particular T_S (500°C) on different substrate were studied. We got smaller grains at higher PO_2 (upto 0.5 mabr) regardless of the substrate nature but the grain size increases with

increase of substrate temperature (fig. 3.4).

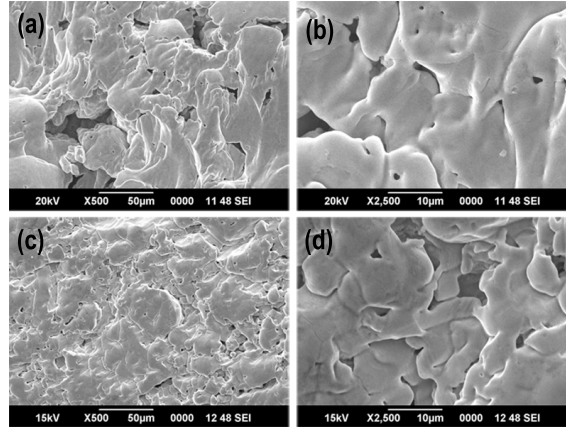


Figure 3.6: FESEM micrographs of the target surface after laser ablation at 1.1 Jcm^{-2} used for ablation (a) KrF laser ($\lambda_{ab}=248 \text{ nm}$) and (c) Nd:YAG laser ($\lambda_{ab} = 266 \text{ nm}$). The corresponding magnified view (b) and (d).

FESEM investigations of the targets surface after laser ablation from KrF excimer and Nd:YAG at 1.1 Jcm^{-2} fluences is shown in figure 3.6. At lower fluence ($0.5\text{-}1.1 \text{ Jcm}^{-2}$) the target surface melted, but the quantity of ablated material was too low to form a dense plasma [85]. After ablation the target surface exhibited a very smooth surface. At such low laser fluences the interaction process is more akin to the thermal evaporation than ablation. At 1.5 Jcm^{-2} laser fluence the target surface exhibiting a recrystallization process. The particulate generation is most likely due to the difference in the absorption coefficient when different laser wavelengths are used for ablation. The formation of particulate increases with increase of ablation wavelength. The absorption coefficient of the target is higher for lower wavelength (KrF excimer laser- $\lambda_{ab} = 248\text{nm}$) than the Nd:YAG laser ($\lambda_{ab} = 266 \text{ nm}$). Hence the penetration depth is more for Nd:YAG

laser ($\lambda_{ab} = 266$ nm) resulting the formation of hills and valleys after the ablation.

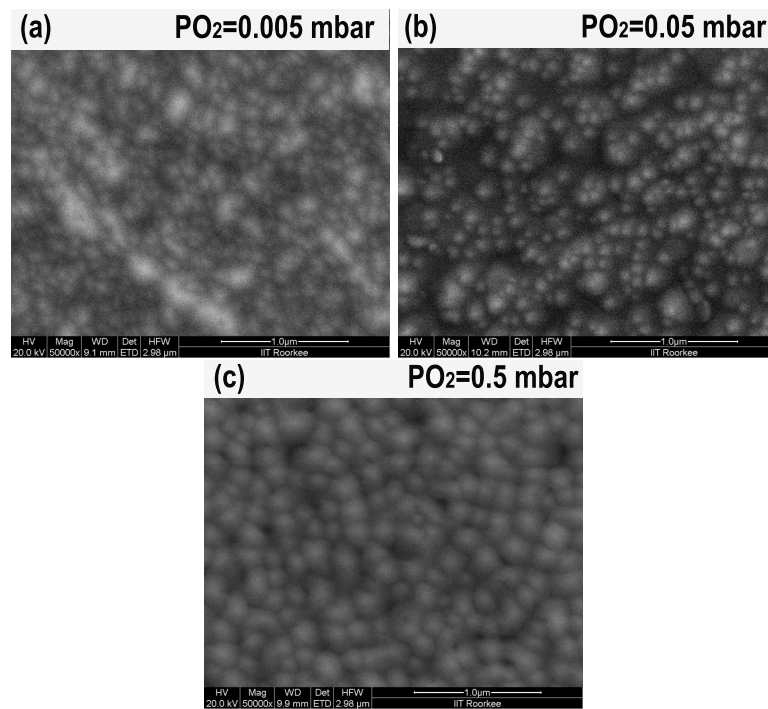


Figure 3.7: FESEM micrographs of the ZnO films prepared at $T_S = 700$ °C and different PO_2 (a) 0.005 mbar (b) 0.05 mbar and (c) 0.5 mbar using KrF laser ($\lambda_{ab} = 248$ nm).

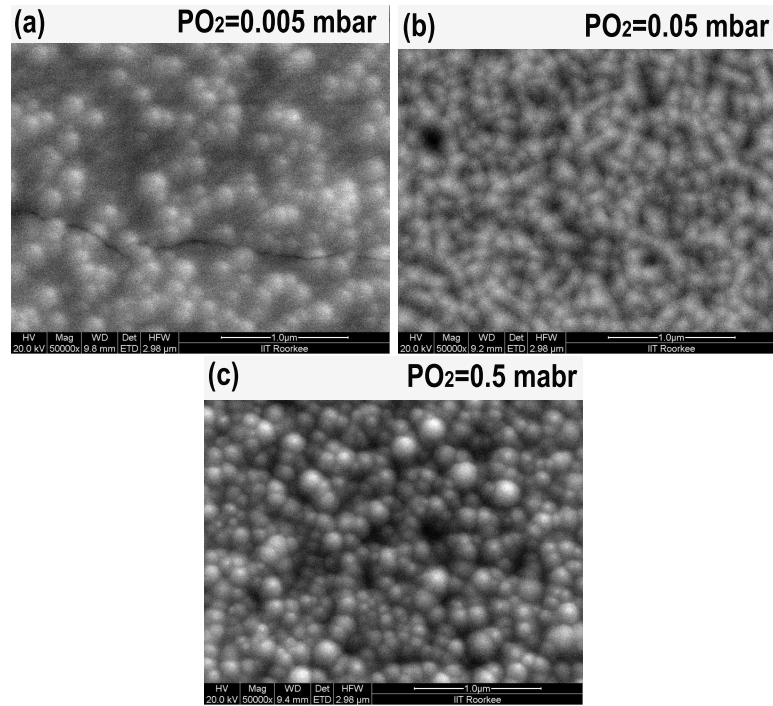


Figure 3.8: FESEM micrographs of the ZnO films prepared on $c\text{-Al}_2\text{O}_3$ substrate at $T_S = 700^\circ\text{C}$ and different PO_2 (a) 0.005 mbar (b) 0.05 mbar and (c) 0.5 mbar using Nd:YAG laser ($\lambda_{ab} = 266\text{ nm}$).

After the detailed structural characterization the surface morphology of the ZnO thin films were analyzed by FESEM. The morphology of the prepared thin films have direct dependence on substrate temperature and oxygen partial pressure. XRD analysis reveals that crystalline nature and grain size of the ZnO thin films varies with the T_S and PO_2 irrespective of the ablation wavelength. ZnO films deposited on $c\text{-Al}_2\text{O}_3$ at PO_2 0.5 mbar and T_S 700°C by KrF shows smooth surface. These films have uniformly packed denser almond like grains (figure 3.7). In the case of films ablated

using Nd:YAG laser we got non uniformly distributed almond like grains (figure 3.8). In both cases the average grain size is of the order of 70-100 nm, which is larger than one calculated from XRD analysis. It is because the XRD reflects the mean grain size at height direction and FESEM the size at lateral direction. The difference may also imply that there should be other growth defects, for example, lattice or intrinsic grain boundary dislocations, which contribute to the broadening of the diffraction peaks. One of the earlier studies shows that longer pulse intervals islands are given more time to ripen and get uniform grains [98]. The island density reduces and film aggregation tends to compact shape as the ablation progresses. In our experiment pulse repetition frequency (10 Hz) of the ablation wavelengths are same so the grains have almost similar structure.

FESEM images of ZnO thin films deposited using KrF excimer laser ($\lambda_{ab} = 248nm$) on different substrates at 600 °C and 0.05 mbar partial pressure of oxygen is shown in figure 3.9. FESEM images shows that the ZnO shows elongated structures. The shape, density and alignment of these nanowires varies with nature of substrate. So the growth of nanostructures are possible with KrF excimer and Nd:YAG lasers.

The film thickness was measured using Dektak stylus profiler. The average thickness of the films were found to be ~230 nm - 270 nm. The transparency, band gap and defect related emissions of the ZnO thin films analyzed by transmission and photoluminescent studies. The optical transmission spectra of the ZnO thin films were recorded in the wavelength range 200-1500 nm using Jasco V-570, UV-vis-NIR spectrophotometer. The optical transmission spectra of ZnO films grown using two different lasers at $T_S=500^\circ\text{C}$ and 0.05 mbar PO_2 are shown in figure 3.10. The films are transparent to visible light and the average optical transmittance values of

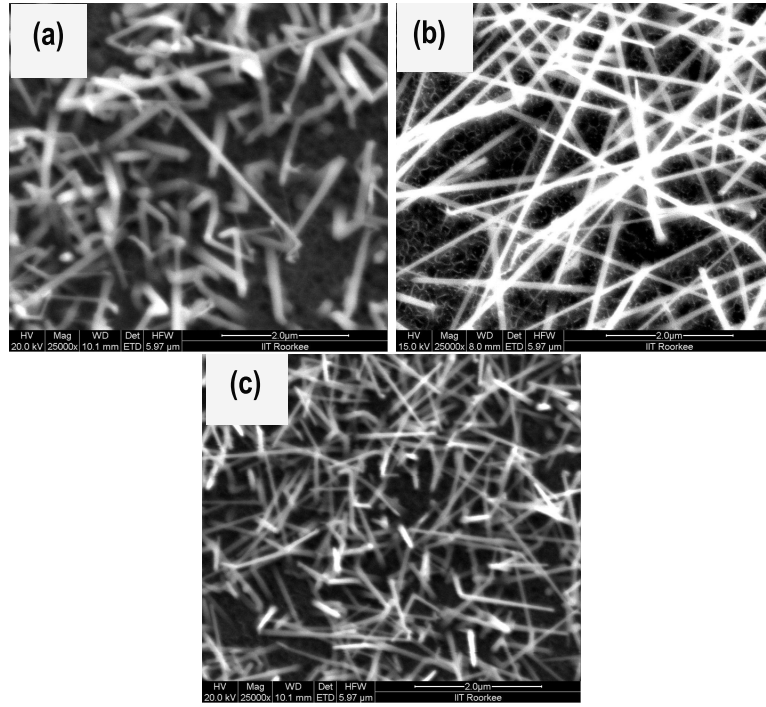


Figure 3.9: SEM micrographs of the ZnO films prepared by PLD on different substrate (a) quartz (b) p-silicon (c) c-Al₂O₃ at $T_S = 600^\circ\text{C}$ and PO_2 0.05 mbar using KrF laser ($\lambda_{ab} = 248$ nm).

films were about 70-90%. The direct band gap semiconductor, ZnO film has an absorption coefficient (α) obeying the following relation for high photon energies ($h\nu$). $\alpha^2 = A(h\nu - E_g)$, where E_g is the optical band gap of thin film, A is a constant and α is the absorption coefficient. The band gap of ZnO films can be calculated by plotting $(\alpha h\nu)$ for ZnO as a function of photon energy ($h\nu$) [99]. The energy band gap E_g for ZnO films grown by KrF and Nd:YAG laser was calculated to be 3.24 eV and 3.25 eV respectively.

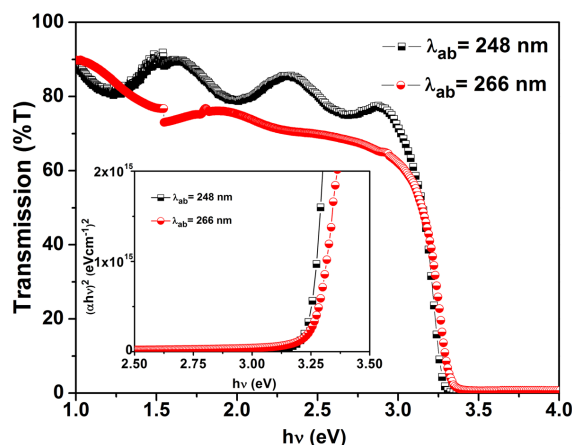


Figure 3.10: Transmission spectra of ZnO thin films grown by PLD using KrF laser ($\lambda_{ab} = 248$ nm) and Nd:YAG laser ($\lambda_{ab} = 266$ nm) at $T_S = 500^\circ\text{C}$ and 0.05 mbar PO_2 .

The photoluminescence (PL) spectra of the ZnO films grown by PLD using KrF and Nd:YAG lasers on quartz substrate at 0.05 mbar PO_2 and various T_S are shown in figure 3.11. Normally the ZnO thin films shows three peaks at 390, 510 and 550 nm labeled as UV, green and yellow bands respectively [100]. In our case ZnO films shows only one emission band in ultraviolet (UV) region at 380 nm without any visible emissions due to defects. The UV emission is attributed to the near band-edge free-exciton transition. The crystalline quality of ZnO films increases with increase of substrate temperature. As a result, the intensity of the UV emission also increases. The intensity and the FWHM of the UV emission strongly depend on the microcrystalline structure of the ZnO films. Jin *et al.* [101] suggested that UV PL intensity depended on the stoichiometry of the ZnO films rather than the microstructural quality of the crystal. In our case irre-

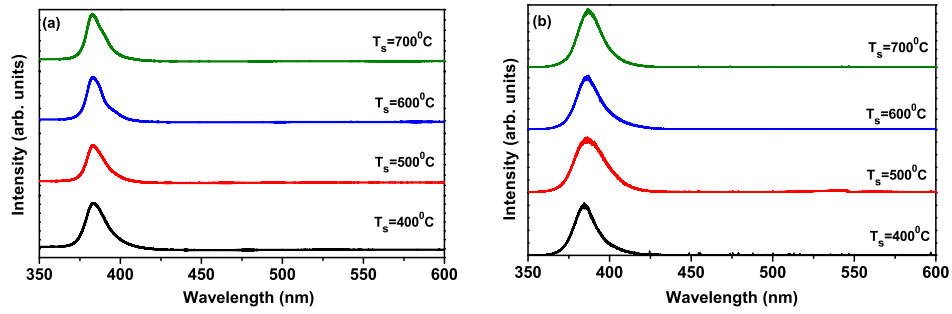


Figure 3.11: The PL spectra of ZnO films prepared at different T_S and 0.05 mbar PO_2 using (a) KrF laser ($\lambda_{ab} = 248$ nm) and (b) Nd:YAG laser ($\lambda_{ab} = 266$ nm).

spective of the ablation laser wavelength the UV PL intensity increase with crystallinity. Shan *et al.* [102] reported that films having good crystallinity have excellent UV emission also.

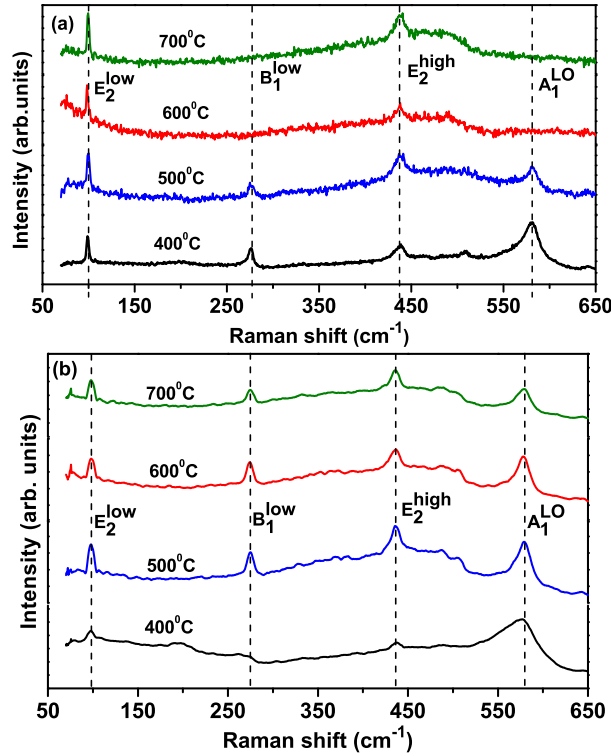


Figure 3.12: The Raman spectra of ZnO films prepared at various T_S and 0.05 mbar PO_2 using (a) KrF laser ($\lambda_{ab} = 248$ nm) and (b) Nd:YAG laser ($\lambda_{ab} = 266$ nm).

Raman scattering is one of the effective technique to investigate the crystal structure, phase purity and defects in the thin films. Wurtzite ZnO belongs to the C_{6v} [103] space group with two formula units per primitive cell. At the G point of the Brillouin zone, the $A_1 + E_1 + 2E_2$ modes are Raman active based on the group theory analysis. Polar A_1 and E_1 modes exhibit different frequencies for the transverse-optical (TO) and longitudinal-optical (LO) phonons, because of the macroscopic electric field associated

with the LO phonons. The non polar E_2 modes have two frequencies, namely E_2^{high} and E_2^{low} .

The Raman spectra of ZnO thin films deposited on quartz substrate using KrF excimer laser and Nd:YAG laser at 0.05 mbar PO_2 and various T_S are shown in figure 3.12. We have to note here that, there are no differences in Raman spectra of ZnO thin films deposited at different temperatures by PLD. The ZnO thin films show three predominant modes at E_2^{low} (99 cm^{-1}), E_2^{high} (436 cm^{-1}), A_1^{LO} (580 cm^{-1}) and one silent mode at B_1^{low} (268 cm^{-1}) [104]. These modes are presented only in highly c-axis oriented thin films. The intensity of the E_2^{high} mode increases with increase of crystalline nature of the thin films. The E_2^{low} mode and E_2^{high} of ZnO were shifted towards lower wave number due increase of disorder in the lattice or the compressive stress induced by the substrate [105].

3.4 Conclusion

The properties of the ZnO thin films grown by PLD on different substrates; quartz, p-Silicon and c- Al_2O_3 using two different UV lasers were studied. Since the wavelength were so close there was no observable variations in the film properties. On the other hand T_S and PO_2 affects the film properties considerably. Two major growth parameters; the substrate temperature and the ambient gas pressure were varied and the resulting films were characterized by XRD, FESEM, Raman spectroscopy and PL spectra. The effect of deposition parameters on the film structure and the optimized conditions for the growth of ZnO thin films by PLD have been identified as $500\text{ }^\circ\text{C}$ (T_S) and 0.05 mbar (PO_2). Under such conditions, highly c-axis oriented ZnO films with FWHM value less than 0.15° is obtained. An

increase in particle size is observed with increase in T_S but an inverse relation is observed with PO_2 . The films have optical transmittance above 80% in the visible region of the spectrum. The surface morphology of the films prepared at higher T_S exhibited almond like structure irrespective of the ablation wavelength. The band gap energies of the thin films were calculated by a linear fit of the transmittance spectra. The strong UV PL emission without defect level emission confirms the growth of highly stoichiometric and crystalline thin films.

Chapter 4

Structural, optical and magnetic properties of transition metal doped ZnO thin films grown by PLD

4.1 Introduction

Dilute magnetic semiconductors (DMS) have been of great interest in the last decade due to the combination of properties of the doped magnetic elements and the carriers of the host. Novel functions can be achieved using DMS, for example, in spin- field effect transistors or spin light emitting diodes, if the injection, transfer and detection of the carrier spin can be controlled electrically or optically [34, 106]. Magnetic properties of II-VI based and III-V based diluted magnetic semiconductors (DMS) have attracted much attention nowadays [33, 46, 107–110]. Spintronics is based

on concepts that utilize the quantum mechanical spin properties of carriers in addition to the carrier charge in realizing electronic functionality. The magnetic properties of a DMS are intimately coupled to the carrier concentration and carrier type within the material through the s-d and p-d exchange integrals. This is beneficial in that it allows external control over the magnetic properties by electronically or optically manipulating the carriers in the DMS. For example, this type of external control has been demonstrated in (In, Mn)As electric field-gated structure. While there has been much work on the III-V DMS materials, notably (In, Mn)As and (Ga, Mn)As, their ferromagnetic (FM) Curie temperatures (T_c) 90K for (In, Mn)As and 172K for (Ga, Mn)As. The realization of practical commercial or mobile devices will require the development of semiconductors that can retain their FM properties above room temperature. As a result, significant research effort has been focused on developing alternative DMS materials with higher Curie temperatures [31, 32, 111]. Carrier spins are used to transport, store and process information in novel ways, providing both enhanced performance and new functionalities in traditional microelectronic devices.

Among the other DMS, ZnO is especially interesting because the valency and ionic radii of the cations match those of the magnetic transition metals. The wide band gap of ZnO (3.37 eV) and large excitonic binding energy (60 meV) are promising characteristics that the room temperature magnetic and transparent optical hybrid devices can be realized with a single compound [106, 112]. This fact allows ZnO doping at high concentrations of magnetic ions. Moreover, some recent theoretical [33, 39] and experimental [113–117] reports have shown the room temperature FM in ZnO films highly doped with magnetic impurities. It is predicted that

n-type co-doping should reinforce the ferromagnetic ordering. Two principal approaches are used to introduce the transition metal ions into semiconductor materials. First the magnetic impurities are implanted into the host matrices [56]. Second the magnetic elements are introduced during the growth [118]. The second method is preferable for the growth of thin films and nanostructures.

This chapter is divided into two parts: first part deals with the growth and characterization of Co and Mn doped ZnO thin films and second part describes the synthesis and characterization of Ni and Cu doped ZnO thin films by PLD for spintronic applications.

4.2 Co and Mn doped ZnO thin films grown by PLD

The Co and Mn doped ZnO thin films have been prepared by various methods like rf-sputtering, chemical vapor deposition, sol-gel methods [33, 119–122]. Pulsed laser deposition (PLD) offers the advantages such as deposition at relatively high oxygen pressure, high deposition rate and growth of highly oriented crystalline films at low substrate temperature. One of the early works on cobalt-doped ZnO by Ueda *et al.* [46] showed that the material to be FM above 280K with 5-25% Co and 1% Al (added as an n-type dopant) without the secondary phases. Theoretical calculations by Sato *et al.* [38] and Yoshida *et al.* [39] predict that ZnO shows ferromagnetism for lower Mn doping concentration (5%) without any additional dopants for increasing the free electron concentration. Since then experimental and computational studies have been carried out on the origin of ferromagnetism in Co and Mn doped ZnO. Some groups observed room

temperature ferromagnetism in the absence of secondary phases or cobalt clusters [42, 48, 123, 124]. However, others report no ferromagnetism at room temperature [43, 125, 126] or that the observed ferromagnetism originates from metallic cobalt clusters [127] or manganese oxides [128]. The origin and reproducibility of the ferromagnetism are still controversial and the magnetic properties are very sensitive to thin film preparation methods and conditions.

During PLD the incorporation of the Co and Mn dopants into the ZnO lattice causes disorders, defects in the lattice and formation of secondary phases which can be analyzed by Raman spectroscopy [128–130]. The magnetic and optical properties strongly depend on the point defects and grain boundary defects arising in the thin film due to doping. In this chapter the magnetic, optical and structural properties of pulsed laser deposited Co and Mn doped ZnO films with dopant content up to 10 at.% are discussed. The intrinsic magnetic behavior and the origin of the defect induced Raman active modes in the Mn doped ZnO thin films were elucidated. The structural and magnetic properties can depend sensitively on film growth parameters and Co and Mn doping percentage. The crystal structure of the $\text{Zn}_{1-x}\text{Co}_x\text{O}$ and $\text{Zn}_{1-x}\text{Mn}_x\text{O}$ thin films were confirmed by XRD and Raman analysis. XPS confirms the oxidation states of Co and Mn dopants in the ZnO thin films.

4.2.1 Experimental

The properties of the deposited thin films depend on the specific synthesis route of the target. The targets were prepared by standard solid-state reaction. Stoichiometric amount of ZnO and Co_3O_4 powders were mixed in methanol medium for two hour and calcinated at 800°C for 15 hrs. The

powder was grounded again and pressed in the form of circular pellets of 1" diameter. These pellets sintered at 900 °C for 24 hrs were used as targets for laser ablation. In a similar method $Zn_{1-x}Mn_xO$ targets were prepared by weighed amount of ZnO and MnO.

Co and Mn doped ZnO thin films were grown on fused silica substrates by pulsed laser deposition (PLD) technique. The fourth harmonic of Nd:YAG laser (266 nm) with repetition rate of 10 Hz and pulse width 6 - 7 ns was used for ablation. The laser beam was focused on to the surface of the target kept inside the vacuum chamber through a quartz window. The ablation was carried out at laser energy density of 1.1 J cm^{-2} . The target was kept rotating during the ablation for uniform deposition and to avoid the pitting of the target surface. Fused silica substrate was placed in front of the target at a distance of 5.5 cm. The chamber was pumped down to a base pressure of 4×10^{-6} mbar and then oxygen was introduced into the chamber through mass flow controller. The deposition parameter such as laser energy, substrate to target distance, substrate temperature and oxygen pressure were initially optimized to get good crystalline films. $Zn_{1-x}Co_xO$ and $Zn_{1-x}Mn_xO$ thin films with various Co and Mn concentrations were grown at various substrate temperatures ($T_S = 350 \text{ °C} - 650 \text{ °C}$) varying the oxygen partial pressure ($PO_2 = 0.05 - 5 \times 10^{-4}$ mbar). The deposition duration was 1 hr for the growth of all thin films resulting a thickness ~ 230 nm.

The crystalline nature of $Zn_{1-x}Co_xO$ and $Zn_{1-x}Mn_xO$ bulk powders and thin films were investigated by Rigaku D-max C x-ray diffractometer with Cu $K\alpha$ (1.5418 Å) line. Stylus profiler (Dektak 6M) was used for thickness analysis. The surface morphology of the thin films were analyzed by Agilent 5500 series atomic force microscopy and scanning electron

microscopy. The transmission spectra of the films were recorded using UV-vis-NIR spectrophotometer (JASCO-V 570). Raman measurements of the $Zn_{1-x}Co_xO$ and $Zn_{1-x}Mn_xO$ bulk powders and thin films were performed by Lab RAM HR spectrophotometer (HORIBA JOBIN YVON) using 514.5 nm Ar^+ laser. The magnetization of all the samples was carried out using Vibrating sample magnetometer and Quantum design MPMS XL-7 superconducting quantum interference device (SQUID) magnetometer.

4.2.2 Results and discussion

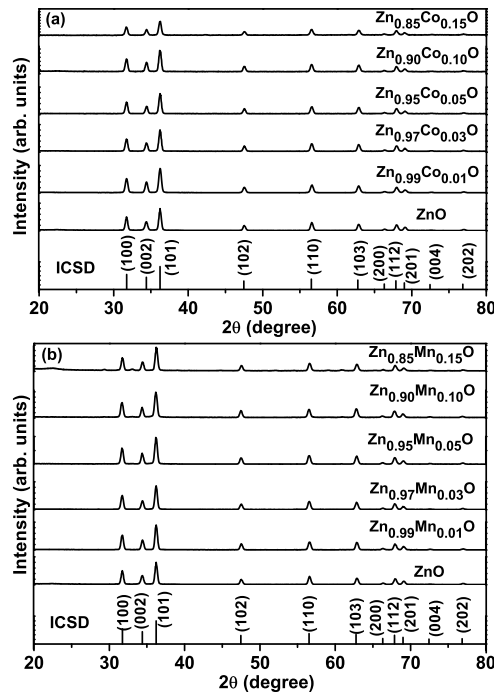


Figure 4.1: XRD pattern of (a) $Zn_{1-x}Co_xO$ and (b) $Zn_{1-x}Mn_xO$ targets for ($x=0-0.15$).

The properties of the deposited thin film depends on the growth conditions and also on the specific synthesis route of the target. The Co and Mn doped ZnO thin films for magnetic studies were grown at a lower T_S of 450°C and PO_2 (5×10^{-4} mbar) to avoid the possible formation of CoO, Co_2O_3 in $\text{Zn}_{1-x}\text{Co}_x\text{O}$ thin films and MnO, Mn_2O_3 in the $\text{Zn}_{1-x}\text{Mn}_x\text{O}$ thin films. The x-ray diffraction pattern of $\text{Zn}_{1-x}\text{Co}_x\text{O}$ and $\text{Zn}_{1-x}\text{Mn}_x\text{O}$ ($x = 0, 0.01, 0.03, 0.05, 0.10, 0.15$) targets are shown in figure 4.1, which confirms the wurtzite hexagonal phase for all the compositions. No secondary phases were detected by XRD upto 10 at.% of Co and Mn doped ZnO bulk powders.

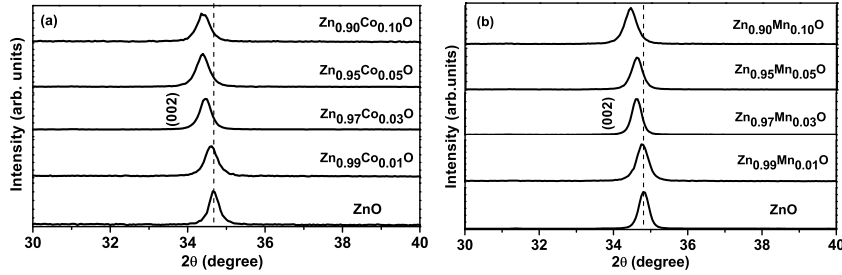


Figure 4.2: XRD pattern of (a) $\text{Zn}_{1-x}\text{Co}_x\text{O}$ and (b) $\text{Zn}_{1-x}\text{Mn}_x\text{O}$ thin films ($x = 0-0.10$) grown by PLD at T_S of 450°C and 0.005 mbar PO_2 .

The XRD pattern of $\text{Zn}_{1-x}\text{Co}_x\text{O}$ and $\text{Zn}_{1-x}\text{Mn}_x\text{O}$ thin films deposited by PLD at T_S of 450°C and 0.005 mbar PO_2 with different Co and Mn concentrations are shown in figure 4.2. The Co and Mn doped ZnO films show only the (002) diffraction peak indicating the films growth along the c axis perpendicular to the substrate surface. None of $\text{Zn}_{1-x}\text{Co}_x\text{O}$ or $\text{Zn}_{1-x}\text{Mn}_x\text{O}$ films show any impurity phases i.e., no peaks corresponding to either cobalt or cobalt oxides and manganese oxides appear in the diffraction pattern. The (002) diffraction peak is shifted slightly to lower angles with increase of

dopant concentration. The very small increase in the c axis lattice constant is due to the substitution of relatively large ionic radii Co^{2+} and Mn^{2+} ions at Zn^{2+} site in ZnO.

The formation of secondary phases in $\text{Zn}_{0.95}\text{Co}_{0.05}\text{O}$ thin films were ruled out from the XRD analysis. The oxidation state of the dopant are further examined by XPS measurements. Figures 4.3 (a),(b) and (c) shows the Zn (2p), O (1s) and Co (2p) core level XPS spectra of the $\text{Zn}_{0.95}\text{Co}_{0.05}\text{O}$ thin film. Two strong peaks appear at 1021.2 eV and 1044.4 eV, which are in agreement with the binding energies of Zn $2\text{P}_{3/2}$ and Zn $2\text{P}_{1/2}$, respectively [88]. The two peaks have narrow line widths, indicating that Zn^{2+} ions are dominant in the thin films. The O (1s) peak is asymmetric and stronger peak at 530.2 eV may be attributed to O^{2-} ions in Zn-O and Co-O bonds [88, 131]. The incorporation of Co is clearly demonstrated by the core level spectra of Co (2p). The Co $2\text{P}_{3/2}$ peak appears at 782 eV. No XPS signals from metallic Co was detected [131]. These results indicate that the doped Co ions are in divalent state. Two XPS peaks of Co^{2+} ions with satellite peaks confirms the uniform incorporation into the ZnO host lattice without any secondary phases.

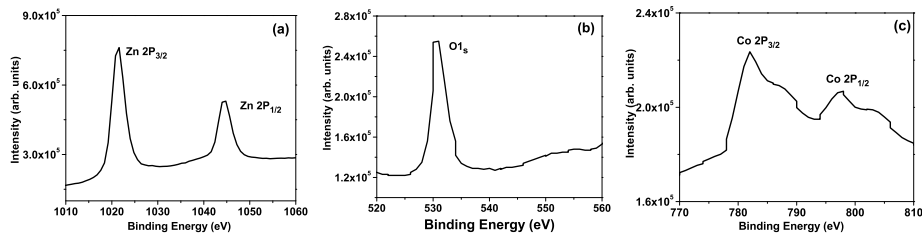


Figure 4.3: XPS spectra of (a) Zn 2p (b) O 1s and (c) Co 2p core levels from $\text{Zn}_{0.95}\text{Co}_{0.05}\text{O}$ thin film.

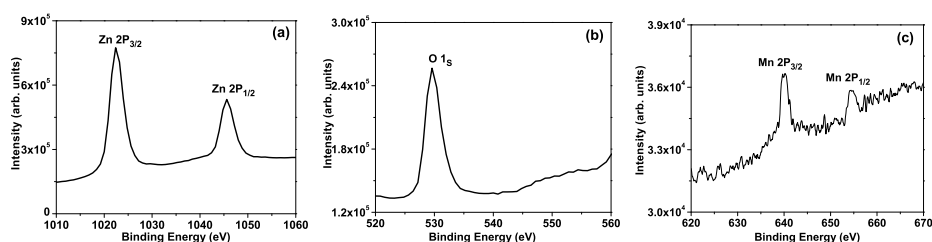


Figure 4.4: XPS spectra of (a) Zn 2p (b) O 1s and (c) Mn 2p core levels from $\text{Zn}_{0.97}\text{Mn}_{0.03}\text{O}$ thin film.

Figure 4.4 (a-c) shows the Zn (2p) and Mn (2p) and O (1s) core level XPS spectra of the $\text{Zn}_{0.97}\text{Mn}_{0.03}\text{O}$ thin film. Two strong peaks appear at 1021.2 and 1044.4 eV, which are in agreement with the binding energies of Zn $2\text{P}_{3/2}$ and Zn $2\text{P}_{1/2}$ respectively. The two peaks have narrow line widths, indicating that Zn^{2+} ions are dominant in the thin films and the influence of Mn impurities is negligible. We got stronger peak of O (1s) at 530.2 eV may be attributed to O^{2-} ions in Zn-O and Mn-O bonds. The peak at 531.8 eV associated with the loosely bound oxygen (e.g., adsorbed O_2 , -OH) chemisorbed on the surface and/or grain boundary of polycrystalline film [132] was not observed. The incorporation of Mn is clearly demonstrated by the core level spectra of Mn (2p). The Mn $2\text{P}_{3/2}$ peak appears at 640.5 eV. No XPS signals from metallic Mn (637.7 eV) were detected. These results indicate that the doped Mn ions are in divalent state [133] without any metallic Mn. The XPS peaks of Mn^{2+} ions were very weak, implying the low incorporation of Mn ions into the ZnO lattice.

SEM images of $\text{Zn}_{1-x}\text{TM}_x\text{O}$ (TM=Mn,Co) thin films deposited on fused silica at substrate temperature 400°C and 0.05 mbar partial pressure of oxygen is shown in figure 4.5. SEM images shows that the ZnO morphology

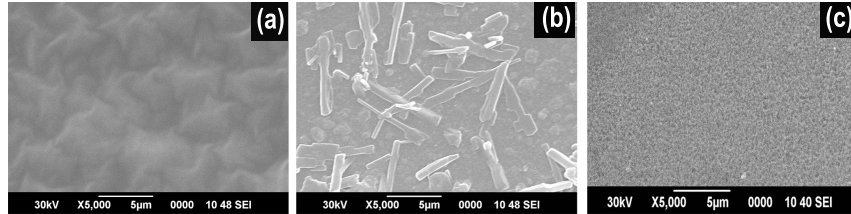


Figure 4.5: SEM images of (a) ZnO (b) $\text{Zn}_{0.97}\text{Co}_{0.03}\text{O}$ and (c) $\text{Zn}_{0.97}\text{Mn}_{0.03}\text{O}$ thin films deposited at T_S of 400°C and 0.005 mbar PO_2 .

is in the form of grains but $\text{Zn}_{0.97}\text{Co}_{0.03}\text{O}$ thin film shows dendrite-like growths. The $\text{Zn}_{0.97}\text{Mn}_{0.03}\text{O}$ thin films show uniformly placed small grains.

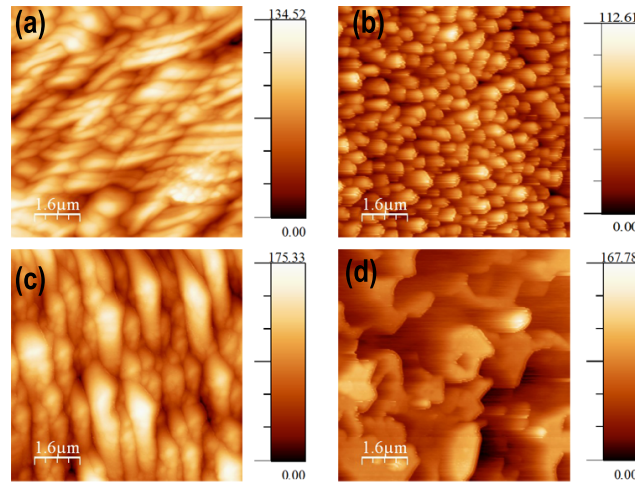


Figure 4.6: AFM images of $\text{Zn}_{1-x}\text{Co}_x\text{O}$ thin films, (a) $x = 0$, (b) $x = 0.03$, (c) $x = 0.05$ and (d) $x = 0.10$ deposited at T_S of 450°C and 0.005 mbar PO_2 .

The film thickness was measured using Dektak stylus profiler. The average thickness of the film was found to be $\sim 230\text{ nm}$. AFM images of $\text{Zn}_{1-x}\text{Co}_x\text{O}$ thin films ($x = 0-10$) on fused silica substrate at 450°C and 0.005 mbar oxygen partial pressure is shown in figure 4.6. The undoped

ZnO film having uniformly distributed smaller grains with RMS roughness of about 6 nm. The $\text{Zn}_{0.97}\text{Co}_{0.03}\text{O}$ films have densely packed columnar growth with RMS roughness of 9 nm and at higher doping become randomly distributed grains. The AFM images of Mn doped ZnO thin films prepared under the same condition shows smaller grains (fig. 4.7). The $\text{Zn}_{0.97}\text{Mn}_{0.03}\text{O}$ film has uniformly distributed smaller grains and the highest RMS roughness observed was 10 nm. At higher Co and Mn doping concentration the morphology of the films changed and RMS roughness increased with Co and Mn concentration. The texture and the crystal quality of Co and Mn doped ZnO films analyzed by AFM measurement.

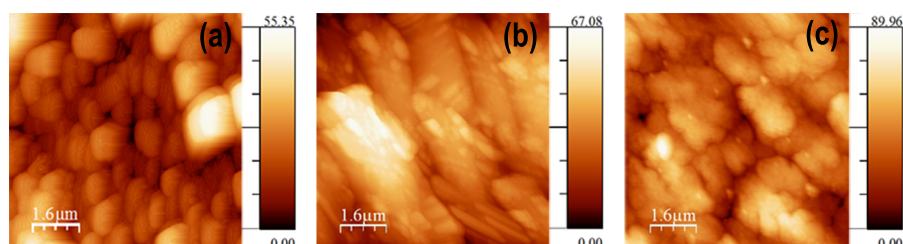


Figure 4.7: AFM images of $\text{Zn}_{1-x}\text{Mn}_x\text{O}$ thin films grown by PLD at 450°C T_S and 0.005 mbar PO_2 (a) $x = 0.03$, (b) $x = 0.05$, (c) $x = 0.10$.

The structurally characterized $\text{Zn}_{1-x}\text{Co}_x\text{O}$ and $\text{Zn}_{1-x}\text{Mn}_x\text{O}$ films transparency, band gap and defect emissions were analyzed by transmission and photoluminescent studies. The optical transmission spectra of Co and Mn doped ZnO films for ($x=0-0.100$) are shown in figure 4.8. The colour of the $\text{Zn}_{1-x}\text{Co}_x\text{O}$ films changes from light green to dark green on increasing the Co content but in the case of $\text{Zn}_{1-x}\text{Mn}_x\text{O}$ it changes from light yellow to amber on increasing the Mn content due to the change in their optical properties. All samples have an average transmittance greater than 80%

indicating good optical quality of the deposited films with low scattering or absorption losses. The green colour of the $\text{Zn}_{1-x}\text{Co}_x\text{O}$ film is assigned to typical d-d transitions of high spin states $\text{Co}^{2+} 3d^7(^4F)$ in tetrahedral oxygen coordination. In its neutral charge state, the Co^{2+} ions have an $[\text{Ar}] 3d^7$ electron configuration. The atomic 4F ground state splits under the influence of the tetrahedral component of the crystal field into 4A_2 ground state and $^4T_2 + ^4T_1$ excited states. The absorption around 1.89, 2.03 and 2.19 eV are in agreement with the Co^{2+} d-d transitions $^4A_2(F) \rightarrow ^2A_1(G)$, $^4A_2(F) \rightarrow ^4T_1(P)$ and $^4A_2(F) \rightarrow ^2E_1(G)$ respectively [134]. The appearance of these transitions clearly confirms that the Co^{2+} ions are in tetrahedral crystal field symmetry. However the transparency of $\text{Zn}_{1-x}\text{Co}_x\text{O}$ and $\text{Zn}_{1-x}\text{Mn}_x\text{O}$ films fades away when the Co and Mn dopant concentration increases.

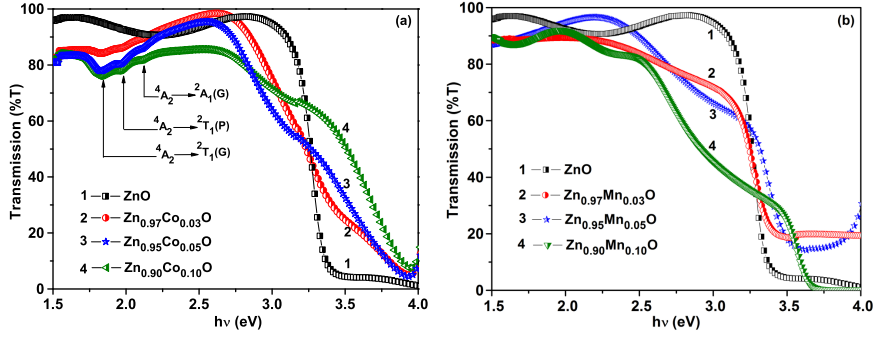


Figure 4.8: Transmission spectra of (a) $\text{Zn}_{1-x}\text{Co}_x\text{O}$ and (b) $\text{Zn}_{1-x}\text{Mn}_x\text{O}$ thin films ($x = 0-0.10$) at 450°C T_S and 0.005 mbar PO_2 .

The variation of band gap energy with Co and Mn concentration in the $\text{Zn}_{1-x}\text{TM}_x\text{O}$ thin films are shown in figure 4.9. The ZnO film shows a sharp absorption edge at 3.35 eV. The band gap estimated from transmission spectra shows a blue shift with increase in Co and Mn concentration

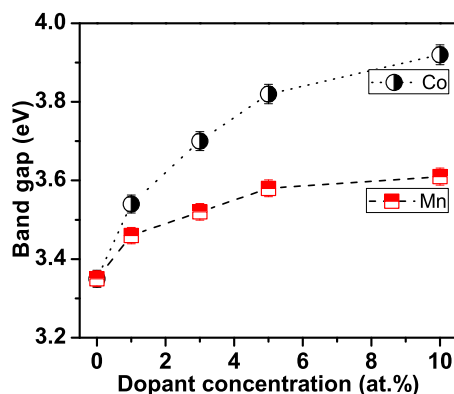


Figure 4.9: Band gap variation of $\text{Zn}_{1-x}\text{Co}_x\text{O}$ and $\text{Zn}_{1-x}\text{Mn}_x\text{O}$ with concentrations ($x = 0-0.10$).

[125, 135, 136]. The band gap of the Co doped ZnO varies from 3.35 eV to 3.78 eV as the cobalt concentration increases from 1-10 at.%. In the case of Mn the band gap is blue shifted from 3.35 eV to 3.92 eV. The absorption takes place in a wide range, therefore it is more reasonable to assign this absorption to the charge-transfer transition between donor ionization levels of Mn ions and the band continuum as observed in $(\text{ZnMn})\text{S}$ and $(\text{ZnMn})\text{Se}$ based on the Anderson impurity model [43]. The observed blue shift was attributed to the Burnstein-Moss effect due to increase of carrier concentration. The Hall measurement confirms the increase of carrier concentration with Co and Mn doping. The band gap is defined as the separation in energy between the top of the valence band and the unoccupied energy states in the conduction band. The shift arises because the Fermi energy (E_F) lies in the conduction band for degenerate n-type doping (or in the valence band for p-type doping). The filled states therefore block thermal or optical excitation. Consequently the measured band gap determined from the

onset of interband absorption moves to higher energy - a blue shift. Similar observations of band gap widening on Co and Mn doping in ZnO have been reported in literature [135, 136].

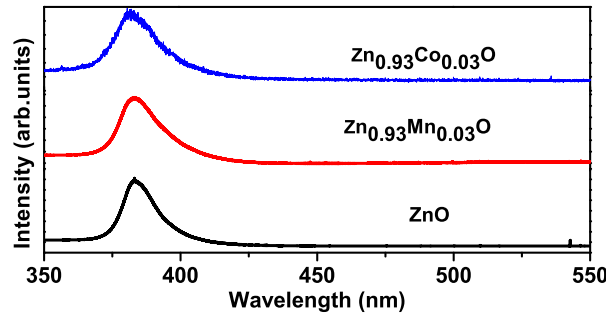


Figure 4.10: PL spectra of $\text{Zn}_{0.97}\text{TM}_{0.03}\text{O}$ thin films grown at T_S of 450°C and 0.005 mbar PO_2 ($\lambda_{exc} = 325$ nm).

The photoluminescence (PL) spectra of the $\text{Zn}_{1-x}\text{TM}_x\text{O}$ films are shown in figure 4.10. All the PL spectra have an emission band in ultraviolet (UV) region at 380 nm. The intensity of near band energy (NBE) emission depends strongly on the crystalline quality of ZnO films. The crystalline quality of Co and Mn doped ZnO films decreases with increase in TM concentration. As a result, the intensity of the UV emission also decreases [96, 137]. The NBE emission results from the exciton related recombination [96, 138]. So the intensity and the FWHM of the UV emission strongly depend on the microcrystalline structure of the $\text{Zn}_{1-x}\text{TM}_x\text{O}$ films.

Raman scattering is one of the effective technique to investigate the crystal structure, phase purity and defects in the thin films. Upon Co and Mn doping, the overall shape of the Raman spectrum changes, due to the loss of symmetry conservation leading to the appearance of 'silent' and mixed Raman modes from points off the center of the Brillouin zone.

Wurtzite ZnO belongs to the C_{6v} [103] space group with two formula units per primitive cell. At the G point of the Brillouin zone, the $A_1+E_1+2E_2$ modes are Raman active based on the group theory analysis. Polar A_1 and E_1 modes exhibit different frequencies for the transverse-optical (TO) and longitudinal-optical (LO) phonons, because of the macroscopic electric field associated with the LO phonons. The non polar E_2 modes have two frequencies, namely E_2^{high} and E_2^{low} .

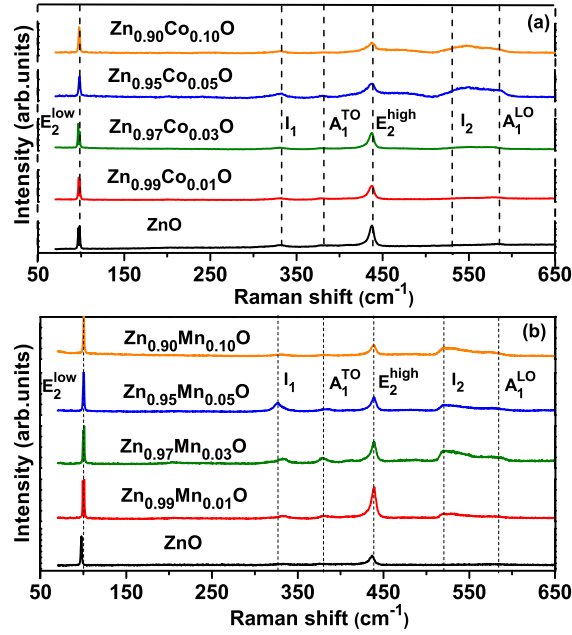


Figure 4.11: Raman spectra of (a) $Zn_{1-x}Co_xO$ and (b) $Zn_{1-x}Mn_xO$ targets ($x = 0-0.10$).

Raman spectra of the $Zn_{1-x}Co_xO$ and $Zn_{1-x}Mn_xO$ bulk powders are shown in figure 4.11. The characteristic optical modes of wurtzite ZnO are

observed at E_2^{low} (99 cm^{-1}), E_2^{high} (436 cm^{-1}), A_1^{TO} (376 cm^{-1}) and E_1^{LO} (584 cm^{-1}) [103, 139]. Apart from the normal modes of vibrations of ZnO two additional modes at 332 cm^{-1} (I_1) and 525 cm^{-1} (I_2) are observed. The modes I_1 and I_2 are assigned as multi-phonon scattering considering the two-phonon process in the disordered lattice due to Co and Mn doping. The modes are identified as $(E_2^{high} - E_2^{low})$ and $(E_2^{high} + E_2^{low})$, respectively [139]. The oxygen sub-lattice vibrational optical mode (E_2^{high}) was found shifted toward lower frequency compared to the ZnO bulk powder samples. A broad band ranging from 500 to 600 cm^{-1} appears at higher Co and Mn concentration, the defect induced modes. The intensity of the broad band increases significantly with Co and Mn doping concentration. When Co and Mn is substituted the Zn lattice site in ZnO, it forms the ternary alloy of $Zn_{1-x}Co_xO$ and the allowed region for the optical phonon becomes finite than the ZnO host lattice. The atomic substitution leads to the structural disorder and breaks the translational symmetry of the allowed phonons. The disorder induced effect causes the phonon line shapes become broadened and shifted towards lower frequency [103, 128, 129, 139, 140].

The Raman spectra of the Co and Mn doped ZnO thin films are shown in figure 4.12. The $Zn_{1-x}Co_xO$ thin films show three predominant modes at E_2^{low} (99 cm^{-1}), E_2^{high} (436 cm^{-1}), A_1^{LO} (581 cm^{-1}) and one silent mode at B_1^{low} (268 cm^{-1}). But in Mn doped ZnO thin films we got three modes E_1^{LO} , E_2^{high} and A_1^{LO} modes and are presented only in highly c-axis oriented thin films. The broadening of the E_2^{high} modes and its red shift indicates the substitution of Co and Mn into the ZnO sub-lattice [141]. The structural disorder due to the atomic substitution breaks the translational symmetry of the zone centered ($k=0$) optical phonons of the host lattice, which leads to the contribution of ($k \neq 0$) phonons to the finite size effects. Thus

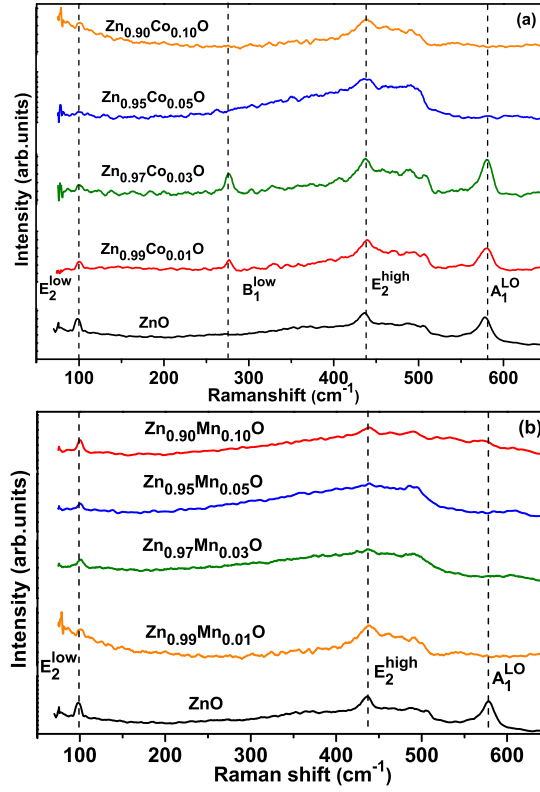


Figure 4.12: Raman spectra of (a) $\text{Zn}_{1-x}\text{Co}_x\text{O}$ and (b) $\text{Zn}_{1-x}\text{Mn}_x\text{O}$ thin films ($x=0-0.10$) at 450°C T_S and 0.005 mbar PO_2 .

Raman spectra confirm the incorporation of Co into the ZnO lattice. The E_2^{low} mode of ZnO was shifted toward higher frequencies and there was an increase in FWHM on Co and Mn substitution into ZnO lattice. A broad band ranging from 340 to 600 cm^{-1} appears at higher Mn concentration and its intensity increases significantly with increase of doping percentage. Similar observations are reported in literature [142, 143]. The multi-peak-fitting result reveals that at 10% Mn doping, the broad band could be

deconvoluted into five peaks, denoted as P₁-P₅ (figure 4.13).

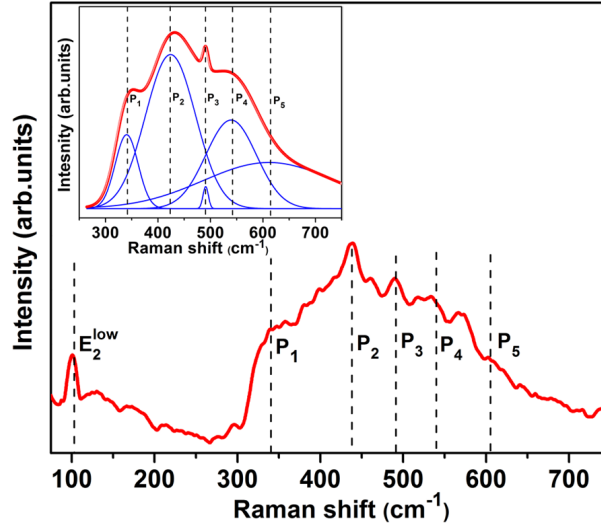


Figure 4.13: Raman spectra of Zn_{0.90}Mn_{0.10}O thin film and the inset shows the multi-peak fitting results.

The disorder-induced effects of E₂^{low} mode in Zn_{0.90}Mn_{0.10}O can be explained by alloy potential fluctuations (APF) using a spatial correlation (SC) model. Using an ab initio calculation, Manjñ *et al.* [144] predicted that the B₁^{low}, 2B₁^{low} and B₁^{high} silent modes of wurtzite ZnO occur at 261, 522 and 552 cm⁻¹, respectively. The peaks, P₂ (434 cm⁻¹), P₃ (485 cm⁻¹) and P₄ (552 cm⁻¹/B₁^{high}) and P₅ (620 cm⁻¹/E₁^{LO}) are present only in heavily Mn-doped ZnO films. Generally, the A₁^{LO} mode is weak because of two opposing contributions from the Frohlich interaction and the deformation potential [144]. However, the breakdown of translational symmetry due to structural disorder caused by a random incorporation of the dopants will lead to alloy potential fluctuations. The spatial correlation

function of the phonon becomes finite which results in the enhancement and broadening of the A_1^{LO} mode. These results are comparable with other groups findings, Hu *et al.* [129] and Wang *et al.* [145]. The defect induced Raman active modes arises due to two major types. The first one is the disorder-induced effects arising on the incorporation of Mn into the ZnO lattice, P_2 (434 cm^{-1}), P_3 (485 cm^{-1}) and P_4 ($552\text{ cm}^{-1}/B_1^{high}$) and surface phonon modes. The second one is due to the native lattice defects P_5 ($620\text{ cm}^{-1}/E_1^{LO}$) [129, 144–146].

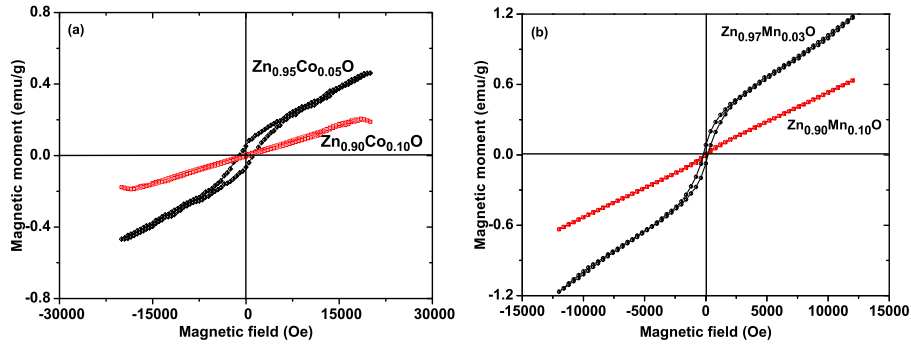


Figure 4.14: M-H curve of (a) $Zn_{1-x}Co_xO$ ($x = 0.05, 0.10$) and (b) $Zn_{1-x}Mn_xO$ ($x = 0.03, 0.10$) bulk powder samples.

Magnetic properties of $Zn_{1-x}TM_xO$ powders and thin films were investigated using vibrating sample magnetometer (VSM) and quantum design SQUID magnetometer respectively. Figure 4.14 shows the field dependent magnetization (M-H) of the $Zn_{1-x}Co_xO$ and $Zn_{1-x}Mn_xO$ pellet at 300 K. The $Zn_{0.95}Co_{0.05}O$ pellet shows ferromagnetic hysteresis loop with coercivity of 540 Oe but at higher Co concentrations $Zn_{1-x}Co_xO$ pellets show a paramagnetic behavior. Metallic cobalt, CoO, Co_2O_3 and nanoclusters of Co are responsible [131] for the reduction of ferromagnetism in $Zn_{1-x}Co_xO$

bulk powders. In the case of Mn doped samples, the $\text{Zn}_{0.97}\text{Mn}_{0.03}\text{O}$ pellet shows hysteresis loop at room temperature. The magnetic moment of $\text{Zn}_{0.97}\text{Mn}_{0.03}\text{O}$ increases with increase in external applied field, indicating a paramagnetic nature with the ferromagnetic loop. The oxides of Mn (MnO , Mn_2O_3) are responsible for the reduction of ferromagnetism at higher Mn doping concentrations [54, 145].

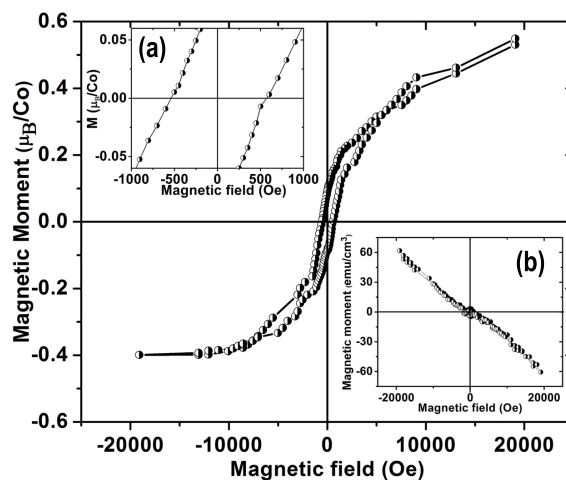


Figure 4.15: M-H curve for $\text{Zn}_{0.95}\text{Co}_{0.05}\text{O}$ film at 300K. Inset shows (a) magnified view near zero field and (b) M-H curve of the ZnO film.

The M-H curve of the $\text{Zn}_{0.95}\text{Co}_{0.05}\text{O}$ thin film is shown in figure 4.15. The samples were prepared and handled carefully to avoid any possible magnetic contamination. Theoretical modeling shows that Co^{2+} - oxygen vacancies are capable of producing long-range ferromagnetic ground state in ZnO [131, 147]. The M-H curve (figure 4.15) of the $\text{Zn}_{0.95}\text{Co}_{0.05}\text{O}$ thin films exhibits coercivity of 450 Oe. The saturation magnetic moment of the $\text{Zn}_{0.95}\text{Co}_{0.05}\text{O}$ thin film is $0.41\mu_B/\text{Co}$ atom. The high spin moment ($3d^7$) of

Co^{2+} is $3\mu_B$, while that of metallic cobalt is $1.7\mu_B$. The ZnO film prepared under the same condition shows diamagnetic nature (inset figure 4.15). Recent studies show that antiferromagnetic oxides below certain critical sizes can exhibit ferromagnetism [131, 147]. In the case of $\text{Zn}_{1-x}\text{Co}_x\text{O}$ thin films nanoclusters of Co and oxides (CoO , Co_2O_3) suppress the room temperature ferromagnetism.

The magnetization curve of the $\text{Zn}_{0.97}\text{Mn}_{0.03}\text{O}$ thin film at 300K is shown in figure 4.16 and the magnified view near zero field shown in the inset. It clearly shows the ferromagnetic loop at lower magnetic field with coercive field of 150 Oe. The curve shows the room temperature ferromagnetism for $\text{Zn}_{0.97}\text{Mn}_{0.03}\text{O}$ thin film [148, 149]. The saturation magnetic moment of the $\text{Zn}_{0.97}\text{Mn}_{0.03}\text{O}$ thin film is $0.37\mu_B/\text{Mn}$ atom. At higher doping percentages the Mn clusters or oxides (MnO , Mn_2O_3) suppress the room temperature ferromagnetism in $\text{Zn}_{1-x}\text{Mn}_x\text{O}$ thin films and paramagnetism is observed [40]. Increased number of n-type carriers and clustering of Mn at higher concentrations in the $\text{Zn}_{1-x}\text{Mn}_x\text{O}$ thin films deviate the system from achieving room temperature ferromagnetism [40, 149].

The shape of the M-H curve reveals that there is some trace of paramagnetism in the $\text{Zn}_{0.97}\text{Mn}_{0.03}\text{O}$ and $\text{Zn}_{0.95}\text{Mn}_{0.05}\text{O}$ thin film also. According to Ruderman-Kittel-Kasuya and Yosida (RKKY) interactions the concentration of free electrons plays a major role in stabilizing the magnetic phase in the Co and Mn doped ZnO thin films. At lower atomic doping concentrations the possibilities of secondary phases in the thin films are over ruled by XRD and Raman measurements [142, 143, 146]. At higher Co and Mn doping concentration, the possible origin of paramagnetism is due to the increase of nearest neighbor interactions among the dopant (Mn^{2+} and Co^{2+}) ions in the ZnO matrix [40, 131, 147, 150].

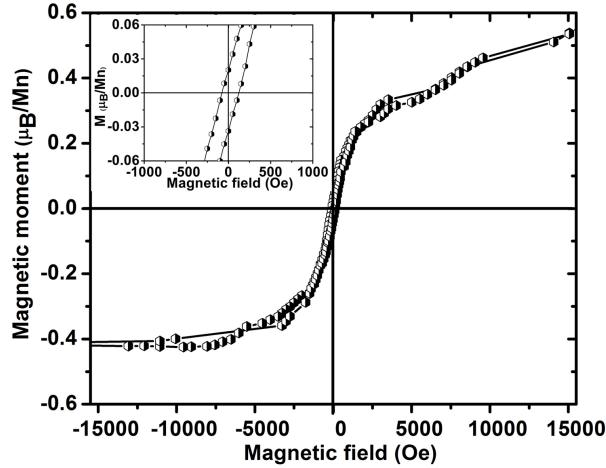


Figure 4.16: M-H curve for Zn_{0.97}Mn_{0.03}O film at 300K. Inset shows magnified view near zero field.

4.2.3 Conclusion

The structure and magnetic properties of Co and Mn doped ZnO films were studied in respect to the Co and Mn concentration and growth conditions. All the films show a wurtzite crystal structure with c axis orientation. The surface morphology of the synthesized samples was characterized by atomic force microscopy. The Zn_{1-x}Co_xO and Zn_{1-x}Mn_xO thin film shows blue shift in the band gap with increase in cobalt and manganese concentration respectively. The presence of non-polar E₂^{high} and E₂^{low} Raman modes in thin films indicates that Co and Mn doping did not change the wurtzite structure of ZnO. Zn_{0.95}Co_{0.05} thin films shows ferromagnetic behavior at room temperature with a saturation magnetization is 0.41 μ_B/Co. In the case of Mn doped ZnO we got magnetization at lower Mn doping (3 at.%) with saturation magnetization of 0.37 μ_B/Mn atom. Oxygen va-

cancies created during growth are likely necessary for the observed ferromagnetism. The magnetic properties rely on intricate combination of transition metal dopants and material defects such as oxygen vacancies which are difficult to characterize. XPS spectra confirms the incorporation of Co^{2+} and Mn^{2+} into the ZnO lattice. The formation of secondary phases in $\text{Zn}_{0.95}\text{Co}_{0.05}$ and $\text{Zn}_{0.97}\text{Mn}_{0.03}\text{O}$ thin films were overruled by XPS analysis. Hence the observed RTFM in Co and Mn doped ZnO thin films were intrinsic in nature.

4.3 Ni and Cu doped ZnO thin films grown by PLD

4.3.1 Introduction

Transition metal-doped ZnO is a promising candidate for spintronics. In order to realize spintronic devices we have to obtain room temperature ferromagnetism in single phase materials without any secondary phases. After the theoretical prediction of RTFM in transition metals doped ZnO thin films the experimental and computational studies have investigated on the origin of ferromagnetism in Ni and Cu doped ZnO. The morphological, optical and magnetic properties of ZnO can be modified by doping with Ni or Cu. The Cu dopant was considered as the origin of green emission in ZnO:Cu thin films [116]. The intrinsic magnetic and Raman spectra of the Ni and Cu doped ZnO thin films and nanostructures have gained much attention recently [113–117].

In this section the structural, optical and magnetic properties of pulsed laser deposited Ni and Cu doped ZnO films with dopant content up to 15%

were discussed. The origin of the defect induced Raman active modes in the Ni and Cu doped ZnO thin films elucidated. The Ni and Cu doping will affect the lattice dynamic properties of the host material and the Raman scattering will provide the information about the crystal structure. The parameters of the Raman modes such as peak width and peak positions is useful in analyzing lattice dynamics. Optical and structural characterizations are used to explore the origin of defect induced photoluminescence in Cu doped ZnO thin films. The formation of defect levels and optical transitions in pure ZnO, $Zn_{1-x}Ni_xO$ and $Zn_{1-x}Cu_xO$ thin films were elucidated using UV-vis absorption and PL studies. The structural information were gathered by XRD and Raman analysis and the oxidation states of the Ni and Cu dopant is confirmed by XPS analysis. Magnetic studies confirms the intrinsic origin of room temperature ferromagnetism in Ni and Cu doped ZnO thin films.

4.3.2 Experimental

Ni and Cu doped ZnO pellets were used as target for the deposition of $Zn_{1-x}Ni_xO$ and $Zn_{1-x}Cu_xO$ thin films. The $Zn_{1-x}Ni_xO$ composite targets were obtained by the standard solid-state reaction. Appropriate amount of ZnO (Alfa Aesar, 99.999%) and NiO (Alfa Aesar, 99.999%) were first weighed, mixed with a few drops of poly vinyl alcohol (PVA) as binder and ground along with methanol for 1 hour. Similarly $Zn_{1-x}Cu_xO$ targets were prepared by conventional solid state reaction using ZnO (Alfa Aesar, 99.999%) and CuO (Alfa Aesar, 99.999%). The mixed powder was blended mechanically again so that the mixture become homogeneous. The mixture was then calcined at 800 °C in air for 12 hours. The resultant powder was grounded again and was pressed into round pellets with 1" diameter and 5

mm thickness. The targets were finally obtained after sintering the pellets in oxygen at 900 °C for 24 hours.

Q-switched fourth harmonic Nd:YAG laser (266 nm) with repetition rate of 10 Hz and pulse width of 6-7 ns was used for the laser assisted film deposition. The ZnO films and Ni and Cu doped ZnO films were deposited on quartz substrate by ablating sintered ZnO, $Zn_{1-x}Ni_xO$ and $Zn_{1-x}Cu_xO$ targets. Before starting deposition the chamber was evacuated to a pressure of 10^{-6} mbar. The ablation was carried out at laser energy density of 1.1 J cm^{-2} . The target was kept rotating during the ablation for uniform ablation and to avoid the pitting of the target surface. The film properties were investigated by depositing them at various substrate temperatures keeping the substrate to target distance 5.5 cm and varying the oxygen pressure to obtain crystalline film.

The structural characterization of as prepared Ni and Cu doped ZnO thin films were carried out by PANalytical X'Pert PRO X-ray diffractometer using Cu $K\alpha$ line (1.5418 \AA). The thickness of the as prepared thin films were measured by Stylus Profiler (Dektak 6M). The surface morphology of the thin films was examined by Agilent 5500 series atomic force microscopy. The transmission spectra of the films were recorded using UV-vis-NIR spectrophotometer (Jasco-V 570). The photoluminescent and Raman measurements of the $Zn_{1-x}Ni_xO$ and $Zn_{1-x}Cu_xO$ thin films were analyzed by Lab RAM HR spectrophotometer (HORIBA JOBIN YVON). An excitation wavelength of 325 nm for the PL measurements and 514.5 nm for Raman studies were used. The magnetic measurements were carried out by Quantum Design MPMS XL-7 superconducting quantum interference device (SQUID) magnetometer.

4.3.3 Results and discussion

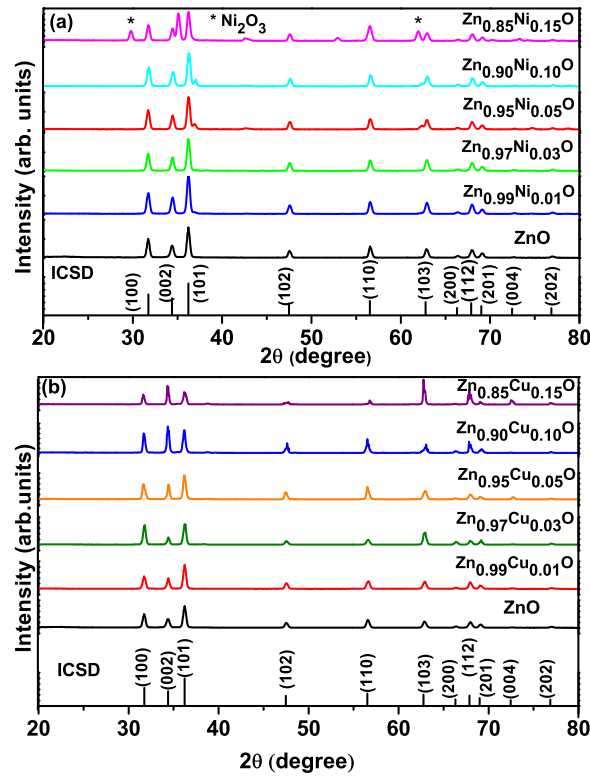


Figure 4.17: XRD pattern of (a) $\text{Zn}_{1-x}\text{Ni}_x\text{O}$ and (b) $\text{Zn}_{1-x}\text{Cu}_x\text{O}$ targets for ($x = 0-0.15$).

The properties of the deposited thin films not only depend on the growth conditions but also on the target preparation conditions. The phase purity of the target and films has been investigated by X-ray diffraction (PANalytical X'pert PRO). The x-ray diffraction pattern of $\text{Zn}_{1-x}\text{Ni}_x\text{O}$ and $\text{Zn}_{1-x}\text{Cu}_x\text{O}$ ($x = 0$ to 0.15) targets sintered at 900°C are shown in figure 4.17. All the diffraction peaks agreed with the reported ICSD data file

[151]. The presences of any other secondary phases were not detected by the XRD upto $x = 10$, but on 15% Ni doping in ZnO we got an additional (002) peak of Ni_2O_3 . No secondary phases were detected in $\text{Zn}_{1-x}\text{Cu}_x\text{O}$ targets upto $x = 0.15$. The colour of the pellets become greenish blue and light green by the increase of Ni and Cu concentration. These structurally characterized pellets were used as the targets for the PLD technique.

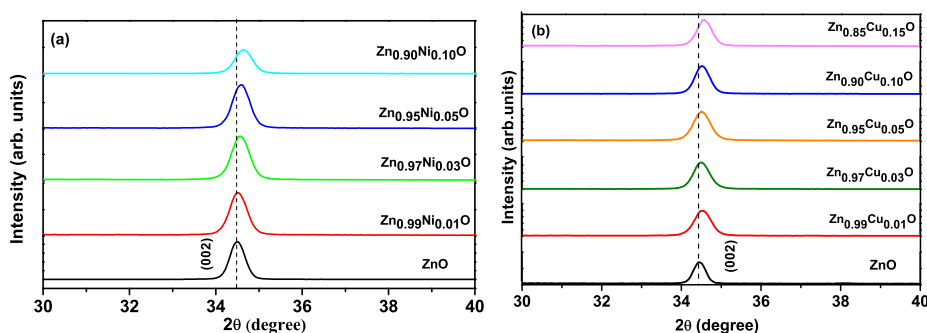


Figure 4.18: X-ray diffraction pattern of (a) $\text{Zn}_{1-x}\text{Ni}_x\text{O}$ and (b) $\text{Zn}_{1-x}\text{Cu}_x\text{O}$ thin films grown by PLD at T_S of 450°C and 0.005 mbar PO_2 .

The structural properties of the Ni and Cu doped ZnO thin films were investigated by depositing them at various substrate temperatures and different substrate to target distance. The x-ray diffraction pattern of highly oriented $\text{Zn}_{1-x}\text{Ni}_x\text{O}$ and $\text{Zn}_{1-x}\text{Cu}_x\text{O}$ thin films grown at substrate temperature (T_S) 450°C and oxygen partial pressure (PO_2) 0.005 mbar are shown in figure 4.18. No peaks corresponding to either CuO or Cu_2O appear in the diffraction patterns of $\text{Zn}_{1-x}\text{Cu}_x\text{O}$. The $\text{Zn}_{1-x}\text{Ni}_x\text{O}$ thin films do not show any sign of impurity phases ie. no peaks corresponding to NiO, NiO_2 or Ni_2O_3 were observed. The (002) diffraction peak is shifted slightly to higher angles with increase of Ni and Cu concentration. The grain size and c axis lattice constant of Ni and Cu doped ZnO shows a small decrease

due to the substitution of relatively smaller ionic radii of $\{\text{Ni}^{2+}$ (0.55 Å) or Cu^{2+} (0.57 Å) $\}$ dopants at Zn^{2+} site (0.60 Å) in ZnO wurtzite network [56, 152]. This confirms that the disordering increases with the increase in Ni and Cu concentration in $\text{Zn}_{1-x}\text{Ni}_x\text{O}$ and $\text{Zn}_{1-x}\text{Cu}_x\text{O}$ thin films resulting in small grain growth. The incorporation of 3d transition metal has reported generally to deteriorate the crystallinity of ZnO [152].

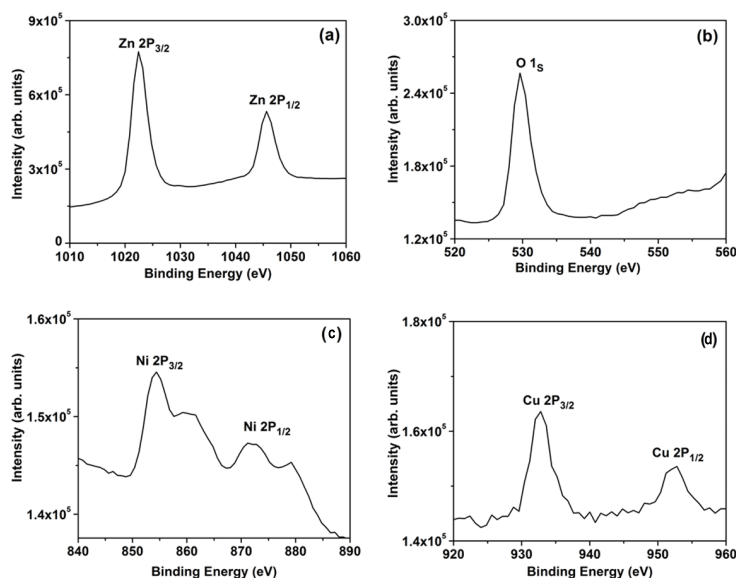


Figure 4.19: XPS spectra of (a) Zn 2p (b) O 1s and (c) Ni 2p and (d) Cu 2p core levels from $\text{Zn}_{0.97}\text{Ni}_{0.03}\text{O}$ and $\text{Zn}_{0.97}\text{Cu}_{0.03}\text{O}$ thin film.

The XPS measurements were carried out to study the bonding nature and oxidation state of the Cu into the $\text{Zn}_{0.97}\text{Cu}_{0.03}\text{O}$ thin films (fig. 4.19 d). The Zn^{2+} shows strong peaks at 1021.2 eV ($2\text{P}_{3/2}$) and 1044.4 eV ($2\text{P}_{1/2}$) [153]. The sharp peaks indicate the dominance of Zn^{2+} ions in the thin films (fig. 4.19 a). The O(1s) shows (fig. 4.19 b) a symmetric

sharp peak at 530.2 eV, it may be attributed to O^{2-} ions in Zn-O bond [154]. The incorporation of Cu is clearly demonstrated by the core level spectra of Cu(2p) and have two peaks located at 932.88 eV ($2p_{3/2}$) and 952.68 eV ($2p_{1/2}$). So the formation of metallic copper is over ruled by the XPS analysis [56]. Similarly in $Zn_{0.97}Ni_{0.03}O$ thin films we observed sharp peaks of Zn^{2+} and O^{2-} . The incorporation of Ni is clearly demonstrated by the core level spectra of Ni (2p) (fig. 4.19 c). The peaks of Ni $2p_{3/2}$ are located at 853.5 eV and 859.8 eV. No XPS signals from metallic Ni (858.9 eV) was detected. These results indicate that the doped Ni ions are in divalent state [155].

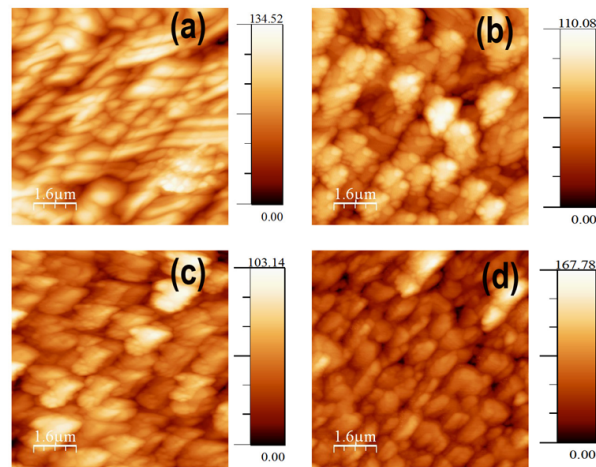


Figure 4.20: AFM images of $Zn_{1-x}Cu_xO$ thin films deposited at T_S 450 °C and 0.005 mbar PO_2 (a) $x = 0$, (b) $x = 0.03$, (c) $x = 0.05$ and (d) $x = 0.10$.

The surface morphology and thickness of the Ni and Cu doped ZnO thin films have direct impact on its optical and magnetic properties. So the thickness of the $Zn_{1-x}Ni_xO$ and $Zn_{1-x}Cu_xO$ films grown by PLD

were measured by stylus profiler (Dektak 6M). The average thickness of the films were found to be ~ 230 nm. The surface morphology of the Ni and Cu doped thin films on fused silica substrate deposited at a substrate temperature 450°C and oxygen partial pressure of 5×10^{-3} mbar were analyzed using Agilent 5500 series AFM in non-contact mode. The RMS roughness of the undoped ZnO is 6 nm and that of 15% Cu doped ZnO is 10 nm (figure 4.20). $\text{Zn}_{1-x}\text{Cu}_x\text{O}$ films have uniformly placed smaller grains. The surface morphology of the $\text{Zn}_{1-x}\text{Ni}_x\text{O}$ thin films were shown in figure 4.21. The $\text{Zn}_{0.97}\text{Ni}_{0.03}\text{O}$ film have uniformly distributed smaller grains and the highest RMS roughness observed was 8 nm. At higher Ni and Cu doping concentration the morphology of the films changed. The RMS roughness of the Ni and Cu doped ZnO films increase with doping percentage. The morphological variation of the ZnO thin films with Ni and Cu doping indicates the incorporation of the transition metals into the ZnO host lattice. These results are consistent with the smaller grain growths observed by XRD analysis.

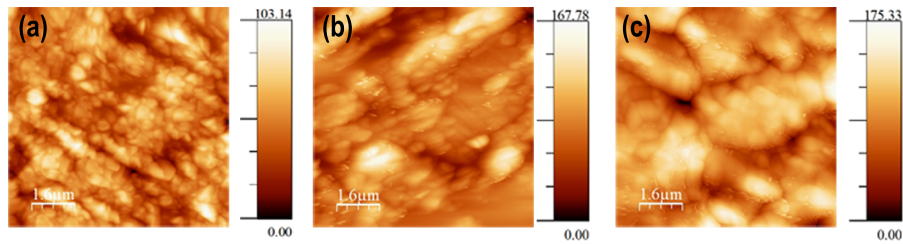


Figure 4.21: AFM images of $\text{Zn}_{1-x}\text{Ni}_x\text{O}$ thin films deposited at T_S 450°C and 0.005 mbar PO_2 (a) $x = 0.03$, (b) $x = 0.05$ and (c) $x = 0.10$.

The optical transmission spectra of $\text{Zn}_{1-x}\text{Cu}_x\text{O}$ ($x = 0, 0.03$ and 0.15) and $\text{Zn}_{1-x}\text{Ni}_x\text{O}$ ($x = 0, 0.01, 0.03$ and 0.10) thin films were recorded in

the wavelength range 300-1200 nm using Jasco-V 570, UV-vis-NIR spectrophotometer (figure 4.22). All the films have an average transmittance greater than 75% in the visible region indicating good quality of the deposited films with low scattering or absorption losses. The colour of the $Zn_{1-x}Ni_xO$ and $Zn_{1-x}Cu_xO$ films become light green and light blue with increase of the dopant concentration. The oscillations in the spectra are caused by multi-reflections at the film-air and film-substrate interfaces. The ZnO film shows a sharp absorption edge at 380 nm. However the transparency of Ni and Cu doped ZnO thin films fade away with increase of the dopant. $Zn_{1-x}Ni_xO$ thin films show predominant visible d-d transitions in the tetrahedral geometry. The absorptions were around 2.10, 2.26 and 2.39 eV, the corresponding d-d transitions ${}^3A_2(G) \rightarrow {}^3T_2(G)$, ${}^3A_2(G) \rightarrow {}^3T_1(G)$ and ${}^3A_2(G) \rightarrow {}^3T_1(P)$. So these d-d transitions clearly indicate that Ni is occupying the tetrahedral lattice points in the ZnO host lattice [156].

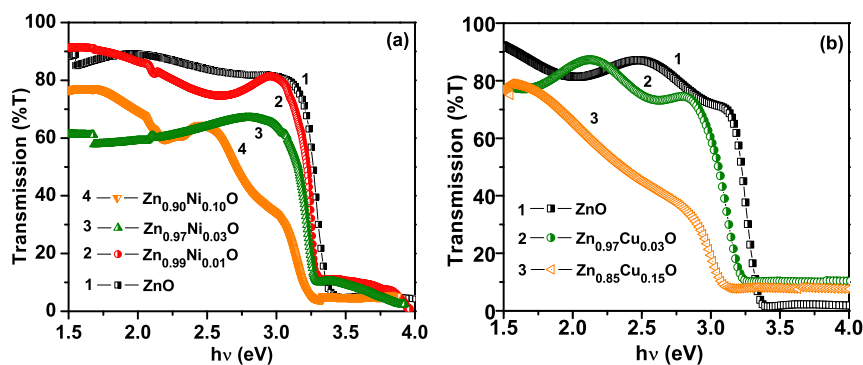


Figure 4.22: Transmission spectra of (a) $Zn_{1-x}Ni_xO$ and (b) $Zn_{1-x}Cu_xO$ thin films at T_S 450 °C and 0.005 mbar PO_2 .

The optical absorption coefficient of a direct band gap semiconductor near the band edge for photon energy $h\nu$ greater than the band gap en-

ergy of the semiconductor is given by $\alpha h\nu = \text{constant} (h\nu - E_g)^{1/2}$ [157]. The band gap of $\text{Zn}_{1-x}\text{Ni}_x\text{O}$ and $\text{Zn}_{1-x}\text{Cu}_x\text{O}$ thin films can be calculated by plotting $(\alpha h\nu)^2$ as a function of photon energy ($h\nu$). The band gap of the $\text{Zn}_{1-x}\text{Cu}_x\text{O}$ films decreases from 3.35 eV to 3.24 eV with increase of Cu concentration upto 10%. In the case of $\text{Zn}_{1-x}\text{Ni}_x\text{O}$ thin films the band gap reduces to 3.17 eV at 10% of Ni doping (figure 4.23). The reduction of optical band gap in $\text{Zn}_{1-x}\text{Cu}_x\text{O}$ and $\text{Zn}_{1-x}\text{Ni}_x\text{O}$ thin films at room temperature may attributed to the sp-d exchange interaction between the band electrons and the localized d electron of the Ni^{2+} and Cu^{2+} ion substituting Zn^{2+} ions [125, 158–160]. The s-d and p-d exchange give rise to negative and positive corrections to the conduction band and the valence band respectively, leading the band gap narrowing [156, 161]. The decrease of absorption edge suggests an increase in the disorder in $\text{Zn}_{1-x}\text{Cu}_x\text{O}$ film. The Ni and Cu substitution in ZnO host lattice creates impurity level in the forbidden energy region of ZnO. Hence the transmission spectra and band gap analysis confirms the Ni and Cu incorporation into the ZnO lattice and its crystalline nature too.

The room temperature photoluminescence (RTPL) measurements of the $\text{Zn}_{1-x}\text{Ni}_x\text{O}$ and $\text{Zn}_{1-x}\text{Cu}_x\text{O}$ films using an excitation wavelength of $\lambda_{ex}=325$ nm are shown in figure 4.24. All the PL spectra have ultraviolet (UV) emission band at 380 nm region. The RTPL shows that the UV emission is red shifted with increase of Ni and Cu concentration. The UV emission is attributed to the near band-edge free-excitation transition and its depends strongly on the crystalline quality of ZnO films. The crystalline quality of Ni and Cu doped ZnO films decreases with increase in Ni and Cu concentration in agreement with the XRD and AFM analysis. The intensity of the UV emission also decreases with increase of Ni and Cu

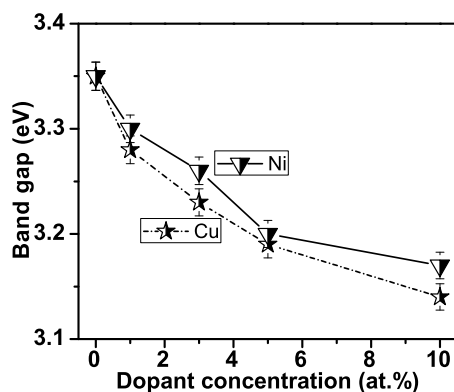


Figure 4.23: Band gap variation of $\text{Zn}_{1-x}\text{Ni}_x\text{O}$ and $\text{Zn}_{1-x}\text{Cu}_x\text{O}$ with concentrations ($x= 0-0.10$).

content in the ZnO thin films [113–115, 162]. The NBE emission results from the exciton related recombination. The green emission (545 nm) was observed in $\text{Zn}_{1-x}\text{Cu}_x\text{O}$ thin films for $x>1\%$ and it is quenched at high Cu doping. Samanta *et al.* [117] and Sakaguchi *et al.* [113] reported that decrease in green emission is due to the formation of point defects, which will act as nonradiative centers. The surface defects, Cu impurities and oxygen vacancies are responsible for the observed green emission [163]. The incorporation of Cu in Zn lattice site will create donor level at 0.17-0.19 eV below the bottom of the conduction band [163, 164]. This Cu impurity center behaves like a trap for non-equilibrium holes or electrons. The radiative recombination of the exciton gives rise to green emission in the spectrum [164–166]. So the intensity and the FWHM of the UV emission strongly depend on the microcrystalline structure of the $\text{Zn}_{1-x}\text{Ni}_x\text{O}$ and $\text{Zn}_{1-x}\text{Cu}_x\text{O}$ films.

Raman scattering is one of the effective technique to investigate the

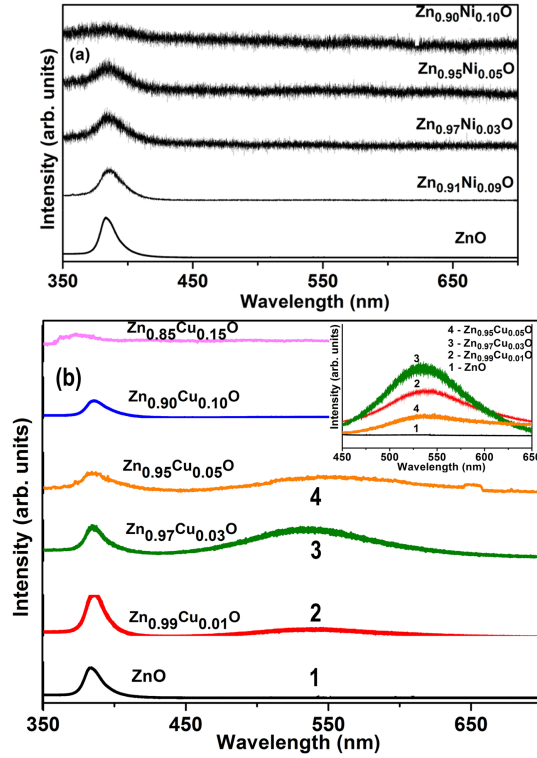


Figure 4.24: Room temperature PL spectra of (a) $\text{Zn}_{1-x}\text{Ni}_x\text{O}$ ($x=0-0.10$) and (b) $\text{Zn}_{1-x}\text{Cu}_x\text{O}$ thin films ($x=0-0.15$). Inset in fig b shows the magnified view of green region.

crystallization, structure and defects in the thin films. The wurtzite structure of ZnO has the space group C_{6v}^4 with two formula units per primitive cell with all atoms occupying C_{6v} sites. Each Zn^{2+} atom is tetrahedrally coordinated to four O atoms and vice versa. The number of optical modes for the ZnO structures is given by $A_1 + E_1 + 2B_1 + 2E_2$, where B_1 modes are silent in Raman scattering, A_1 and E_1 modes are polar and hence, exhibit different frequencies for the transverse-optical (TO) and longitudinal-optical

(LO) phonons. The non polar E_2 modes have two frequencies, namely E_2^{high} and E_2^{low} associated with the motion of oxygen atoms along with zinc sub lattice vibrations [21, 103, 167].

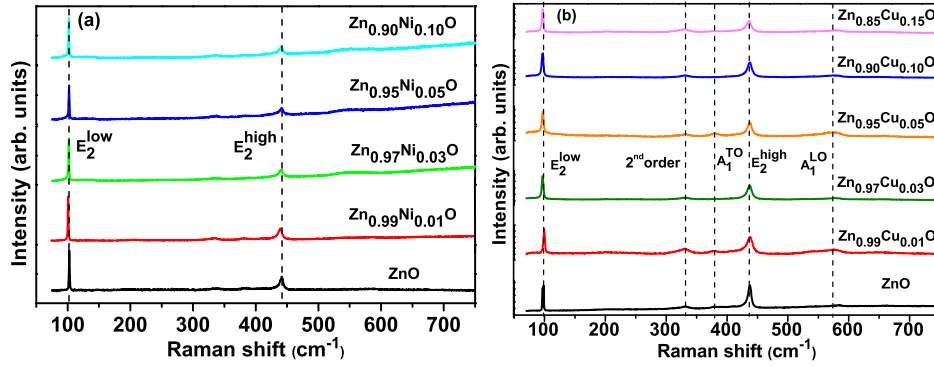


Figure 4.25: Raman spectra of (a) $Zn_{1-x}Ni_xO$ ($x = 0-0.10$) and (b) $Zn_{1-x}Cu_xO$ ($x = 0-0.15$) bulk powder samples.

Raman spectra of the Ni and Cu doped ZnO bulk powders are shown in figure 4.25. In $Zn_{1-x}Ni_xO$ powders we observed normal modes at E_2^{low} (100.5 cm^{-1}) and E_2^{high} (438 cm^{-1}), other modes are suppressed [21, 167]. But in the case of $Zn_{1-x}Cu_xO$ powders the characteristic optical modes of wurtzite ZnO are observed at E_2^{low} (99 cm^{-1}), E_2^{high} (436 cm^{-1}), second phonon line (332 cm^{-1}), A_1^{TO} (376 cm^{-1}) and A_1^{LO} (575 cm^{-1}) [103, 166]. The oxygen sub-lattice vibrational optical mode (E_2^{high}) of the $Zn_{1-x}Cu_xO$ bulk powder samples were found shifted toward lower wave number compared to that of the ZnO bulk powder. When transition metal is substituted the Zn lattice site in ZnO, it forms the ternary alloy of $Zn_{1-x}TM_xO$ and the allowed region for the optical phonon becomes finite than the ZnO host lattice. The atomic substitution leads to the structural disorder and breaks the translational symmetry of the allowed phonons. The disorder induced

effect causes the phonon line shapes become broadened and shifted towards lower wavenumber [33, 117, 140].

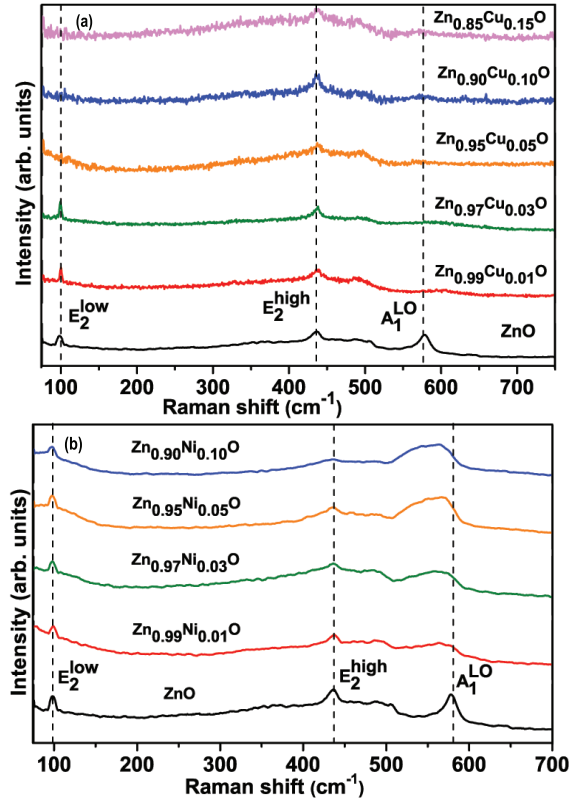


Figure 4.26: Raman spectra of (a) $\text{Zn}_{1-x}\text{Cu}_x\text{O}$ ($x = 0-0.15$) and (b) $\text{Zn}_{1-x}\text{Ni}_x\text{O}$ ($x = 0-0.10$) thin films.

The Raman spectra of the $\text{Zn}_{1-x}\text{Cu}_x\text{O}$ thin films (figure 4.26 a) shows three predominant modes at E_2^{low} (99 cm^{-1}), E_2^{high} (435 cm^{-1}) and A_1^{LO} (575 cm^{-1}). These modes are present only in highly c-axis oriented thin films. The broadening of the E_2^{high} modes and its red shift indicates the substitution of Cu into the ZnO sub-lattice [114, 117, 168]. The disappear-

ance of the A_1^{LO} mode and red shift of the E_2^{high} mode at higher Cu doping is due to the formation of mixed crystal states [114, 117]. Thus Raman spectra confirms the incorporation of Cu into the ZnO lattice and all the films are oriented along the c-axis.

The Raman spectra of the $Zn_{1-x}Ni_xO$ thin films are shown in figure 4.26 b. The E_2^{low} mode of ZnO was shifted towards lower frequencies and there was an increase in FWHM up to 10% of Ni substituted ZnO. The shift of E_2^{low} mode was detected as 1.05 cm^{-1} compared to the bulk value. The FWHM was found to increase with nickel concentration in $Zn_{1-x}Ni_xO$ thin films. The atomic substitution of Ni in ZnO host lattice induces structural disorder. The disorder induced effect (lower frequency shift and broadening) in $Zn_{1-x}Ni_xO$ thin films were explained by alloy potential fluctuations (APF) using a spatial correlation (SC) model [103, 140, 169]. When the crystal is alloyed the spatial correlation region of the phonons become finite owing to the potential fluctuation of the alloying disorder, which gives rise to the relaxation of $q=0$ selection rule in Raman scattering. A broad band ranging from 300 to 700 cm^{-1} appears at higher Ni concentration and its intensity increases significantly with increase of doping percentage. Similar observations are reported in literature [152, 167]. The multi-peak-fitting result reveals that at 10% Ni doping broad band could be deconvoluted into five peaks, denoted as P_1 - P_5 (figure 4.27).

The disorder induced effects of E_2^{low} mode in $Zn_{1-x}Ni_xO$ can be explained by alloy potential fluctuations using a spatial correlation model. Manjon *et al.* [144] predicted that the B_1^{low} , $2B_1^{low}$ and B_1^{high} silent modes of wurtzite ZnO occur at 261 , 522 and 552 cm^{-1} , respectively. In our case, the peaks, P_2 ($434 \text{ cm}^{-1}/E_2^{high}$), P_3 ($485 \text{ cm}^{-1}/I_1$) and P_4 ($552 \text{ cm}^{-1}/B_1^{high}$) and P_5 ($620 \text{ cm}^{-1}/E_1^{LO}$) are present only in heavily Ni-doped ZnO films.

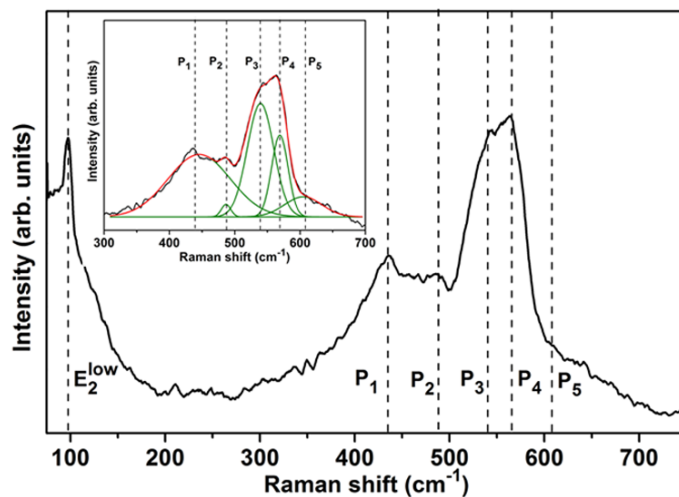


Figure 4.27: Room temperature Raman spectra of $\text{Zn}_{0.90}\text{Ni}_{0.10}\text{O}$ thin films and inset shows multi-peak fittings.

Generally, the A_1^{LO} mode is weak because of two opposing contributions from the Frohlich interaction and the deformation potential [56]. The defect induced Raman active modes arise due to two major types of lattice disorders. The first one is the disorder induced effects arising on the incorporation of Ni into the ZnO lattice, P_2 ($434\text{ cm}^{-1}/E_2^{high}$), P_3 ($485\text{ cm}^{-1}/I_1$) and P_4 ($552\text{ cm}^{-1}/B_1^{high}$) and surface phonon modes. The second one is due to the native lattice defects P_5 ($620\text{ cm}^{-1}/E_1^{LO}$).

The decrease of crystalline nature, formation of defect induced Raman active modes and reduction of optical band gap confirms the uniform incorporation of Ni and Cu into the ZnO host lattice. If the doping percentage is above 5 at.% the reduction of the UV emission (for Ni and Cu doping) and the green emission (for Cu doping) occurs. According to the above structural and optical characterization and in view of spintronic applica-

tion the study focusses the magnetic studies of the thin films below 5 at.% only. Room temperature magnetic properties of Ni and Cu doped ZnO thin films were investigated using Quantum Design MPMS XL-7 superconducting quantum interference device (SQUID) magnetometer.

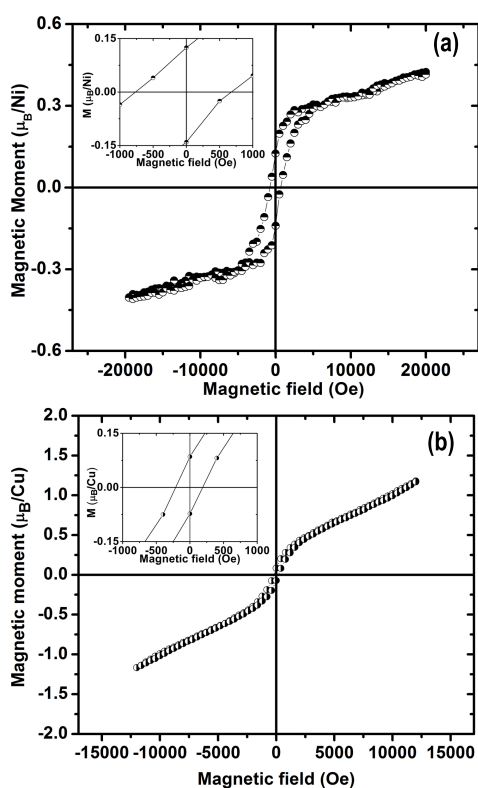


Figure 4.28: Room temperature M-H curve of the (a) $\text{Zn}_{0.97}\text{Ni}_{0.03}\text{O}$ and (b) $\text{Zn}_{0.97}\text{Cu}_{0.03}\text{O}$ thin films. Inset shows the magnified view near zero field.

The magnetic behaviour of the $\text{Zn}_{0.97}\text{Ni}_{0.03}\text{O}$ and $\text{Zn}_{0.97}\text{Cu}_{0.03}\text{O}$ thin films prepared at 450°C and 5×10^{-4} mbar are shown in figure 4.28 a and b respectively. The magnetization field (M-H) curve reveals an obvious

hysteresis loop, indicating the room temperature ferromagnetic ordering existing in the films. The saturation magnetization (M_S) and coercive field (H_C) of the 3 at.% Cu doped ZnO films are $0.28 \mu_B/\text{Cu}$ and 190 Oe respectively. But the Ni doped ZnO films shows better saturation magnetization (0.34 B/Ni atom) and coercive field (640 Oe). The ZnO thin films prepared at the same condition shows diamagnetic nature. $\text{Zn}_{0.97}\text{TM}_{0.03}\text{O}$ thin films prepared at 450°C and 0.05 mbar oxygen pressure shows lower saturation magnetization than one prepared at 5×10^{-4} mbar pressure. This support the assumption that magnetism is due to the exchange interaction between local spin polarized electrons and conduction electrons. According to Ruderman- Kittel- Kasuya and Yosida (RKKY) interactions the concentration of free electrons plays a major role in stabilizing the magnetic phase in the $\text{Zn}_{0.97}\text{Ni}_{0.03}\text{O}$ or $\text{Zn}_{0.97}\text{Cu}_{0.03}\text{O}$ thin films. ZnO is n-type material, due to oxygen vacancies and zinc interstitials. Higher oxygen pressure result in less oxygen vacancies and reduce the carrier concentration. At higher concentrations the TM clusters and transition metal oxides suppress the room temperature ferromagnetism in $\text{Zn}_{1-x}\text{TM}_x\text{O}$ thin films and paramagnetism is observed. The possibilities of metallic Ni and Cu and secondary phases (NiO, Ni_2O_3 , CuO) is over ruled by XRD and Raman measurements [33, 152]. In the application point of view we can use these lower at.% doped ZnO materials for spintronic devices.

In $\text{Zn}_{1-x}\text{Cu}_x\text{O}$ thin films magnetization is reduced by the formation of secondary phases - CuO and Cu_2O . The theoretical magnetic moment of Cu^{2+} ion is $\sim 1 \mu_B$. At higher Ni concentration in $\text{Zn}_{1-x}\text{Ni}_x\text{O}$ thin films increased number of metallic Ni, NiO and Ni_2O_3 deviate the system from achieving room temperature ferromagnetism [47, 152, 167]. The decrease of saturation magnetization at higher Ni and Cu doping due to increased

number of Ni and Cu atom occupying adjacent cation site resulting anti-ferromagnetic alignment [47, 170].

4.3.4 Conclusion

Pulsed Laser Deposition technique is one of the physical methods for the preparation of highly oriented compound semiconductors and doped semiconductors. The thin films morphology and optical properties can be tuned by varying the laser fluence and background pressure. Phase pure $Zn_{1-x}Ni_xO$ ($x = 0-10$) and $Zn_{1-x}Cu_xO$ ($x=0-15$) thin films were grown by PLD technique. The PLD targets were synthesized by solid state reaction. The wurtzite structure of the targets were confirmed by XRD. The structural, morphological, optical and magnetic properties of TM doped ZnO films were analyzed. XRD pattern reveals that all the Ni and Cu doped ZnO films have c-axis orientation normal to the substrate. The surface morphology characterized by atomic force microscopy shows $Zn_{1-x}Cu_xO$ and $Zn_{1-x}Ni_xO$ films have uniformly placed smaller grains and larger gains at higher doping percentages. The TM doped ZnO films have transmittance greater than 75% in the visible region. The band gap of the ZnO thin films shows red shift with increase of Ni and Cu concentration in thin films. The Cu doped ZnO thin film shows green PL emission at 542 nm and the band edge emission at 385 nm. The defect induced Raman active modes in Ni and Cu doped ZnO thin films and bulk sample is also elucidated. The presence of non-polar E_2^{high} and E_2^{low} Raman modes in thin films indicates that Ni and Cu doping didnt change the wurtzite structure of ZnO. The intensity of E_2^{high} high mode and the peak position shifted towards the lower wavenumber with increase of Ni and Cu concentration. The XPS confirm the incorporation of Cu^{2+} and Ni^{2+} ions into the ZnO

lattice. Room temperature ferromagnetism is obtained for lower doping concentrations of Ni and Cu. The combination of photoluminescent and magnetic properties of $\text{Zn}_{1-x}\text{Cu}_x\text{O}$ thin films make them attractive for spin light emitting diodes.

Chapter 5

Structural, optical and magnetic properties of hydrothermally grown transition metal (Cu/Ni/Mn) doped ZnO nanostructures

5.1 Introduction

Semiconductors with dimensions in the nanometer realm are important because their electrical, optical and chemical properties can be tuned by changing the size of the particles. Optical and magnetic properties of these materials are of great interest for application in optoelectronics, photo-

voltaics and spintronics. Zinc oxide (ZnO) is a unique material with a direct band gap (3.37 eV) and large exciton binding energy of 60 meV [171, 172]. ZnO has been widely used in gas sensors, transparent conductor and for piezoelectric applications [173–177]. II-VI semiconductors doped with transition metals have aroused research interest due to their robust magnetic properties. In dilute magnetic semiconductors (DMS) a fraction of the host atoms is replaced by magnetic atoms resulting a magnetically active solid solution. The new class of semiconductor nanostructures having combined magnetic, optical and electronic properties have applications in the field of spintronics and nanoelectronics [34, 178]. A large number of research work have been published after the theoretical prediction on the room temperature ferromagnetism (RTFM) exhibited by transition metals doped ZnO. The theoretical predictions realizes RTFM in p-type transition metals doped ZnO [179]. However the origin of RTFM is not clearly understood but the properties are highly process dependent.

The ZnO nanoparticles can be prepared on a large scale by low cost simple solution - based methods, such as chemical precipitation [180, 181], sol-gel synthesis [182] and solvothermal/hydrothermal reaction [183–185]. The hydrothermal process have several advantages over other growth processes such as use of simple equipment, catalyst-free growth, low cost, large area uniform production, environmental friendliness and less hazardous. The low reaction temperature makes this method an attractive one for microelectronics and plastic electronics [186]. This method has also been successfully employed to prepare nano-scale ZnO and other luminescent materials. The particle properties such as morphology and size can be controlled via the hydrothermal process by adjusting the reaction temperature, time and concentration of precursors.

Transition metals (TM) doped ZnO nanopowders need high temperature sintering, which will cause agglomeration of transition metal in the ZnO lattice during the cooling process. The present study focuses on the low temperature hydrothermal synthesis of surfactant free ZnO and TM doped ZnO structures. The existence of RTFM and Raman spectra in Cu/Ni/Mn doped ZnO is visualized by various groups [187–189]. But the origin of ferromagnetism is still debatable whether due to the formation of impurity phases or clusters during the growth process [178]. In this chapter we report the hydrothermal synthesis of ZnO and ZnO:TM nanostructures and the effect of TM concentration on the structural, optical, morphological and magnetic properties.

5.2 Experimental

The pure ZnO and ZnO:TM nanostructures were grown by hydrothermal method. An appropriate amount of ammonium hydroxide was added to the mixture of zinc acetate (0.3 M-1 M) and copper acetate or nickel acetate or manganese acetate (0.001 M-0.1 M) solution to adjust the pH value between 9 and 11. The TM content in the nanostructures is modified by varying the molar ratio of zinc acetate and TM acetate. The mixture was stirred vigorously for 30 minutes to form a homogeneous solution. These solutions were transferred into teflon lined stainless steel autoclave and maintained at a temperature range of 100-200 °C for 3 to 6 h under autogenous pressure. It was then allowed to cool naturally to room temperature. After the reaction was complete, the resulting solid products were washed with methanol, filtered and then dried in air in a laboratory oven at 60 °C.

The structural characterizations of the ZnO:TM nanostructures were carried out by Rigaku D-max C x-ray diffractometer using Cu K α radiation (1.5418 Å). The surface morphology and chemical composition of the nanostructures were analyzed by SEM and EDAX measurements using JEOL Model JSM - 6390LV. The optical absorption of the these nanostructures were recorded using UV-vis-NIR spectrophotometer (JASCO-V 570). The photoluminescent and Raman measurements of the ZnO:TM nanostructures were recorded by Lab RAM HR spectrophotometer (HORBIA JOBIN YVON). An excitation wavelength of 325 nm for the PL measurements and 514.5 nm for Raman measurements were used. The magnetization measurements of all the samples were performed using vibrating sample magnetometer (Lakeshore VSM 7410).

5.3 Results and discussion

X-ray diffraction studies confirmed that the synthesized materials were ZnO with wurtzite phase and all the diffraction peaks agreed with the reported ICSD data [151] and no characteristic peaks other than ZnO were observed (fig.5.1). The lattice parameters 'a' and 'c' increase with TM incorporation into the ZnO lattice (fig.5.2). The lattice parameter variation strongly reflects the relationship between ionic radii of the TM ion [Cu²⁺ (0.57Å) or Ni²⁺ (0.55Å or Mn²⁺ (0.66Å)] and Zn²⁺ ion (0.60Å). The calculated lattice parameters were also in agreement with the reported values [188].

ZnO:TM nanostructures were synthesized hydrothermally at 150 °C for 3 h by keeping the concentration of Zn(CH₃COO)₂ as 1 M in all reactions, while the concentration of TM(CH₃COO)₂ was varied from 0.001 M to 0.1 M. All the peaks match well with the standard wurtzite structure of ZnO

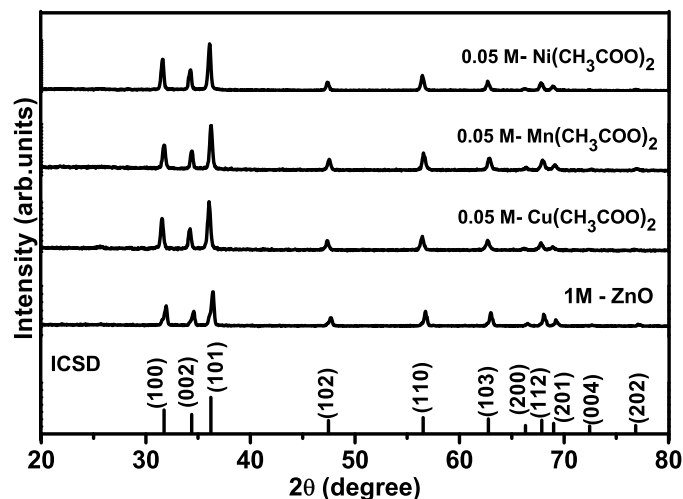


Figure 5.1: XRD patterns of TM doped ZnO nanostructures synthesized from 1 M $\text{Zn}(\text{CH}_3\text{COO})_2$ with 0.05M concentration of $\text{TM}(\text{CH}_3\text{COO})_2$ (TM=Cu,Mn,Ni) at 150 °C for 3 h.

and the FWHM of the (101) diffraction peak increases with the increasing concentration of $\text{TM}(\text{CH}_3\text{COO})_2$ due to structural disorders.

Under hydrothermal conditions the $\text{Zn}(\text{OH})_2$ precipitate will dissolve to considerable extent to form ions of Zn^{2+} and OH^- . Once the product of $[\text{Zn}^{2+}]$ and $[\text{OH}^-]$ exceeds a saturation level the ZnO crystals will precipitate. The solubility of ZnO is significantly smaller than that of $\text{Zn}(\text{OH})_2$ under hydrothermal conditions, consequently, the $\text{Zn}(\text{OH})_2$ precipitates will be transformed into ZnO crystals during the hydrothermal process [190, 191]. At the initial stage of the process, the concentrations of Zn^{2+} and OH^- were relatively higher so that the crystal growth in different directions was possible [190, 192]. So the molar ratio of $\text{TM}(\text{CH}_3\text{COO})_2$

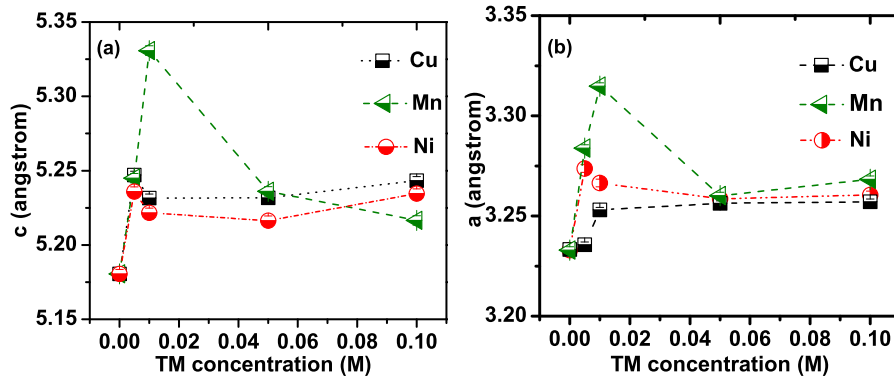


Figure 5.2: The lattice parameters 'a' and 'c' of ZnO:TM nanostructures.

during the growth process will provide the TM^{2+} ion into the ZnO nanostructures. The TM^{2+} (Cu/Ni/Mn) doping can be controlled by adjusting the concentration of the $\text{TM}(\text{CH}_3\text{COO})_2$ in the precursor solution.

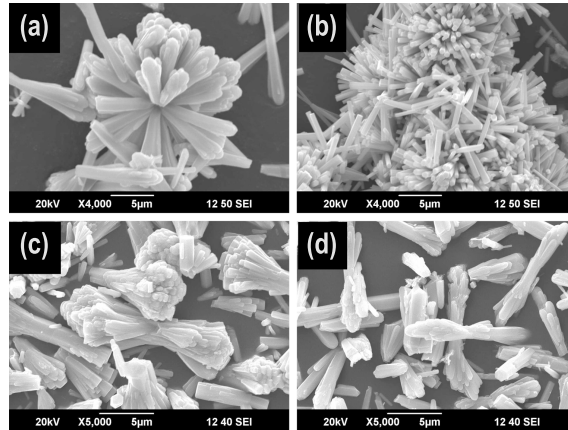


Figure 5.3: SEM images of ZnO and ZnO:TM nanostructures synthesized at 150°C for 6 h (a) undoped ZnO and ZnO doped with 0.05 M (b) $\text{Cu}(\text{CH}_3\text{COO})_2$, (c) $\text{Mn}(\text{CH}_3\text{COO})_2$, (d) $\text{Ni}(\text{CH}_3\text{COO})_2$ in the precursor solution.

The morphology and chemical composition of as synthesized nanostructures were investigated by SEM and EDAX analysis. Figure 5.3 shows the SEM images of undoped ZnO and TM doped ZnO nanostructures prepared using 0.05 M TM(CH₃COO)₂ in the precursor solution at 150 °C for 6 h. SEM images confirm the formation of ZnO nanostructures and is assembled like branched structures. The TM doping change the morphology and we get uniformly placed elongated nanorods in the form of bunches. The diameter of the ZnO:Cu nanorods decreases with Cu incorporation. The ZnO:Cu rods have average diameter of 100 nm and length of about 3 μm. The ZnO:Mn rods have average diameter of 100 nm and length of about 2.5 μm. The Ni doping change the morphology and we get elongated nanorods. The diameter of the ZnO:Ni nanorods decreases with Ni incorporation. The ZnO:Ni rods have average diameter of 100 nm and length of about 3 μm. SEM results showed a decrease in aspect ratio of nanorods with increasing TM²⁺ doping percentage. The agglomeration could be induced by densification resulting from the narrow space between particles, but the ZnO:TM nanorods doesn't show any cluster formation. The incorporation of TM into the ZnO nanorods was confirmed by EDAX measurements. Figure 5.4 shows the EDAX spectra of ZnO:TM nanorods with 0.05 M TM(CH₃COO)₂ in the precursor solution. The EDAX indicates that TM is incorporated uniformly into the ZnO nanorods.

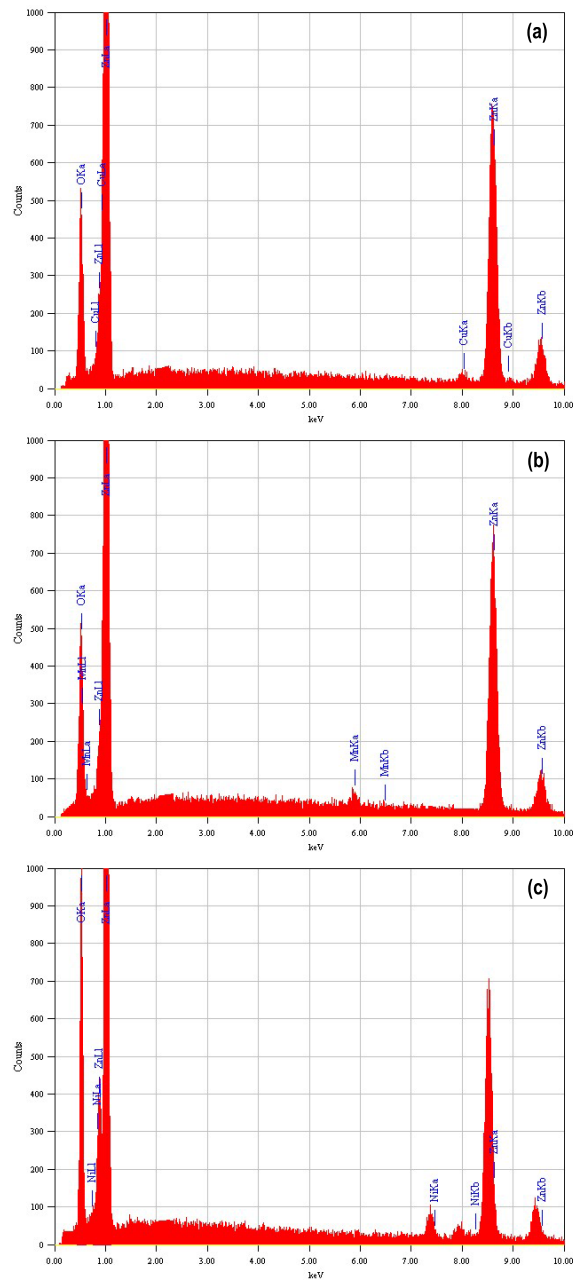


Figure 5.4: EDAX spectra of ZnO:TM nanostructures synthesized at 150 °C for 6 h with (a) 0.05 M $\text{Cu}(\text{CH}_3\text{COO})_2$, (b) 0.05 M $\text{Mn}(\text{CH}_3\text{COO})_2$ and (c) 0.05 M $\text{Ni}(\text{CH}_3\text{COO})_2$ in the precursor solution.

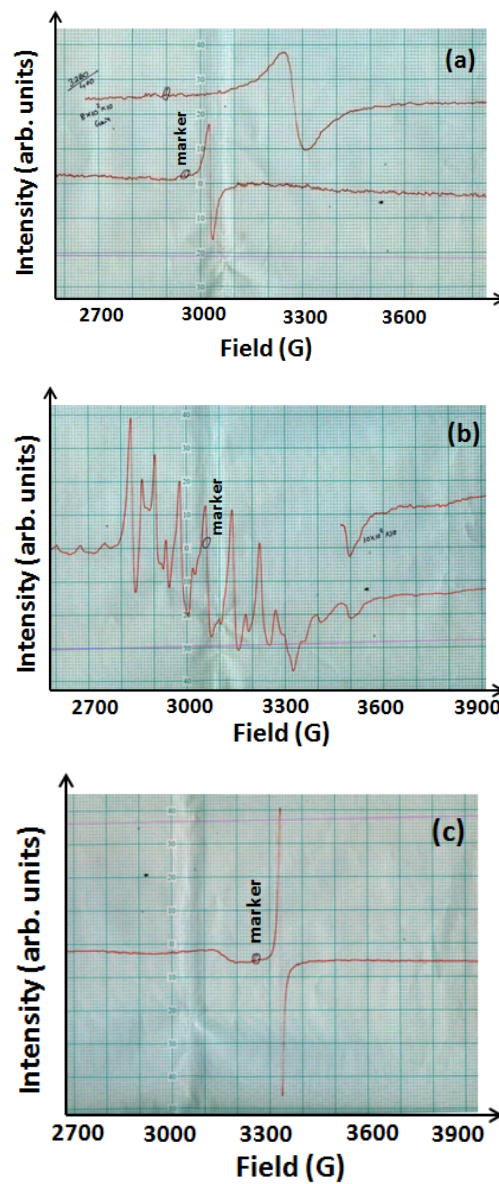


Figure 5.5: Room temperature EPR spectra of ZnO:TM nanostructures synthesized at 150 °C for 6 h with (a) 0.05 M $\text{Cu}(\text{CH}_3\text{COO})_2$, (b) 0.05 M $\text{Mn}(\text{CH}_3\text{COO})_2$ and (c) 0.05 M $\text{Ni}(\text{CH}_3\text{COO})_2$ in the precursor solution.

The incorporation of the TM^{2+} ion into ZnO nanostructures is further confirmed by electron paramagnetic resonance (EPR) analysis (fig.5.5). This technique used to characterize the environment of paramagnetic species in a host lattice. The ZnO:Cu and ZnO:Ni samples shows a broad peak and the corresponding 'g' values are 1.958 and 1.957 respectively. But the Zn:Mn nanostructures shows a sextuplet superimposed on a broad background of resonance indicating the isolated free Mn^{2+} ions and 'g' value is 2.002. The 'g' values of TM^{2+} are well agreement with the reported ones [193, 194].

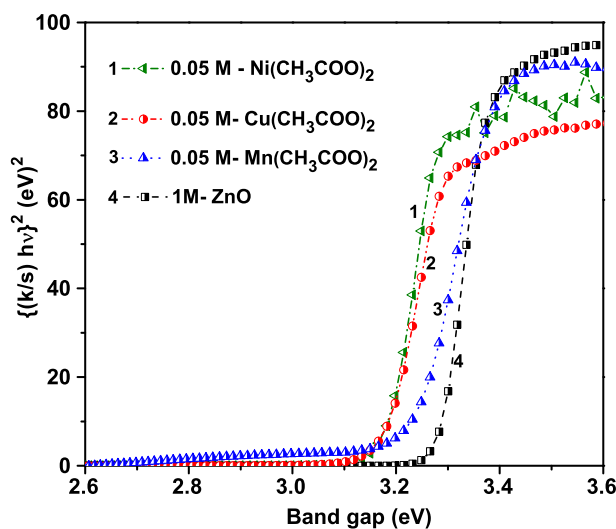


Figure 5.6: The $\{[k/s]h\nu\}^2$ vs $h\nu$ plot of ZnO:TM nanostructures synthesized at 150°C for 3 h with 0.05 M TM concentration.

Diffuse reflectance spectral studies in the UV-vis-NIR region were carried out to estimate the optical band gap of synthesized nanostructures. Figure 5.6 shows the plot of $\{[k/s]h\nu\}^2$ vs $(h\nu)$ of the nanoparticles synthe-

sized via hydrothermal method at 150 °C for 3 h for 0.05 M TM(CH₃COO)₂ concentration. The band gap of ZnO:TM nanostructures shows red shift with increase of TM doping. The observed red shift in the band gap energy of transition-metal doped II-VI semiconductors was attributed to the ‘sp-d’ spin-exchange interactions between the band electrons and the localized d electrons of the transition-metal ion substituting the cation. Diouri *et al.* [161] and Bylsma *et al.* [195] had theoretically explained the mechanism behind ‘s-d’ and ‘p-d’ exchange interactions using second-order perturbation theory attributed to band gap narrowing. The red shift of the band gap confirms the substitution of TM into the ZnO lattice and the band gap narrowing is due to the exchange interactions [195–197]. ZnO:Ni nanostructures shows mid band gap absorptions at 439 (2.82 eV), 615 (2.01 eV) and 655 nm (1.89 eV) corresponding to $^4A_2(F) \rightarrow ^3T_1(P)$ crystal field splitting in tetrahedrally bonded Ni²⁺ ions [198, 199].

The room temperature photoluminescence (RTPL) spectra of the ZnO:TM nanostructures excited at 325 nm is shown in figure 5.7. The ZnO:Cu nanostructures have two emission bands, an ultraviolet (UV) emission band in 370 nm and a broad orange-red emission centered at 630 nm [200]. Other TM (Mn/Ni) doped ZnO nanostructures have PL spectra similar to undoped ZnO nanostructures. The UV emission is attributed to the near band-edge free-exciton transition [201].

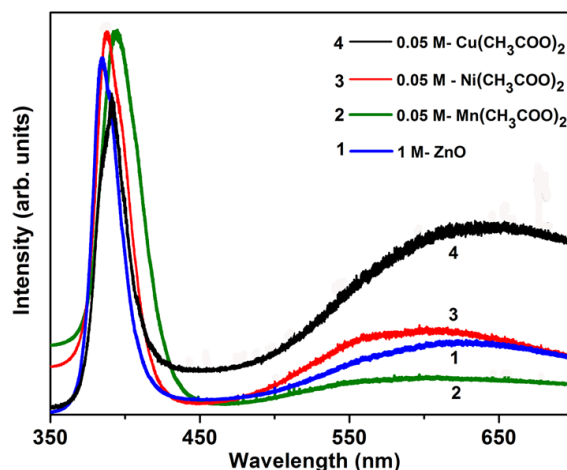


Figure 5.7: Room temperature PL spectra ($\lambda_{exc} = 325nm$) of ZnO:TM nanostructures synthesized at $150^\circ C$ for 3 h with 0.05 M TM concentration.

The different surface to volume ratios of nanostructures with different diameters may affect the intensities of defect emissions, but the shift in peak positions is not expected to be significant. Green and yellow emissions are the most commonly observed defect emissions in ZnO nanostructures [202, 203]. The green emission is attributed to oxygen vacancies or zinc interstitials [204]. Yellow defect emission is typically attributed to oxygen interstitials [205]. The defect responsible for yellow emission is not located at the surface [14], unlike the green emission. The intensity of the green-yellow related emission due to defect was found to be dependent also on the nanowire diameter [202]. Cu impurities have been proposed as origin of the green emission in Cu doped ZnO materials [206]. Fan *et al.* [207] reported that the visible emission in ZnO dendritic wires and nanosheets consisted of two components centered at ~ 540 nm and ~ 610 nm.

The ZnO:Cu nanostructures have shown a broad orange-red emission

[207, 208] centered at 640 nm. The orange-red emission from the nanorods shows a slight red shifted with increase of $\text{Cu}(\text{CH}_3\text{COO})_2$ concentration in the precursor solution. The intensity of orange-red emission decreases with increase of $\text{Cu}(\text{CH}_3\text{COO})_2$ concentration in the precursor solution [209]. This emission consists of a small green component, which is likely due to copper impurities or oxygen vacancies and dominant red emission, whose width makes it difficult to resolve components in orange-red spectral range ($\sim 630\text{-}700$ nm). So the green, yellow and orange-red emissions likely originate from different defect-related transitions, in agreement with the literature [210, 211]. If the sample contains both green and orange-red emissions, it is very difficult to distinguish in UV excitation ($\lambda_{exc} = 325\text{nm}$) because all the emissions will contribute to the RTPL. ZnO:Ni and ZnO:Mn nanostructures shows UV emission at 370 nm and broad deep level emission (DLE) [162, 212] centered at 620 nm. Generally the UV emission in ZnO:Mn and ZnO:Ni reduces at higher doping percentage. [138, 204]. The intensity of the visible emission reduces at higher concentration of $\text{Mn}(\text{CH}_3\text{COO})_2/\text{Ni}(\text{CH}_3\text{COO})_2$ in the precursor solution due to non-radiative recombination processes.

Raman spectroscopic studies were employed to understand the effect of TM doping on microscopic structure and vibrational properties of prepared ZnO:TM nanostructures. The collective Raman modes of ZnO can be represented as E_2^{low} (100 cm^{-1}), E_2^{high} (437 cm^{-1}), A_1^{TO} (380 cm^{-1}), A_1^{LO} (580 cm^{-1}), E_1^{TO} (407 cm^{-1}) and E_1^{LO} (587 cm^{-1}) [213, 214]. Wurtzite ZnO belongs to the C_{6v} space group with two formula units per primitive cell. At the G point of the Brillouin zone, the $A_1 + E_1 + 2E_2$ modes are Raman active based on group theory analysis [141]. Polar A_1 and E_1 modes exhibit different frequencies for the transverse-optical (TO) and longitudinal-optical

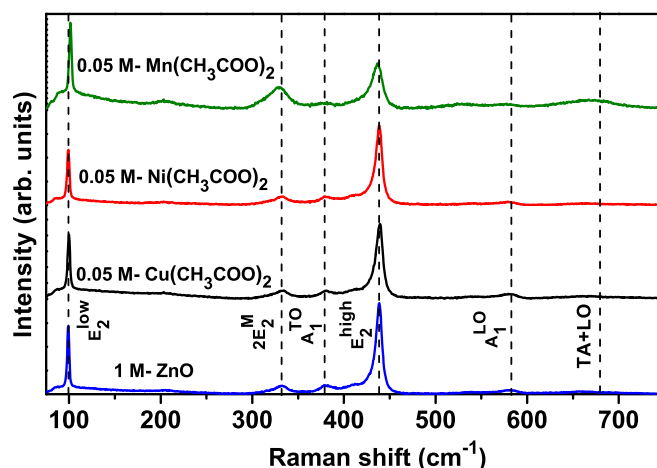


Figure 5.8: Raman spectra of ZnO:TM nanostructures synthesized at 150 °C for 3 h with 0.05 M TM concentration.

(LO) phonons, because of the macroscopic electric field associated with the LO phonons. The non polar E_2 modes have two frequencies, namely E_2^{high} and E_2^{low} , associated with the motion of oxygen atoms along with zinc.

Raman spectra of ZnO:TM nanostructures (fig.5.8) show five predominant modes at E_2^{low} (100 cm^{-1}), second phonon line- $2E_2^M$ (332 cm^{-1}), A_1^{TO} (380 cm^{-1}), E_2^{high} (437 cm^{-1}) and A_1^{LO} (580 cm^{-1}). The slight broadening of the E_2^{high} modes and its red shift from the bulk value indicates the substitution of TM ions into the ZnO sub-lattice [140, 167, 187, 188, 215, 216]. The shifting and broadening of E_2^{high} is due to the potential fluctuations of the alloy disorder by TM incorporation into the ZnO lattice. The intensity of the second phonon line- $2E_2^M$ (332 cm^{-1}) and TA+LO (670 cm^{-1}) modes increases with Mn concentration in the precursor solution [187, 189]. The enhancement of these modes are due to the reinforcement of LO phonon scattering. The impurity-induced mechanism is responsible for the enhance-

ment of A_1^{LO} (580 cm^{-1}) and TA+LO (670 cm^{-1}) mode. The mode shifting and broadening in ZnO:TM nanostructures are due to the enhancement of residual stress, structural disorder and crystal defects with TM doping. Thus Raman spectra confirm the incorporation of TM ions into the ZnO nanostructures.

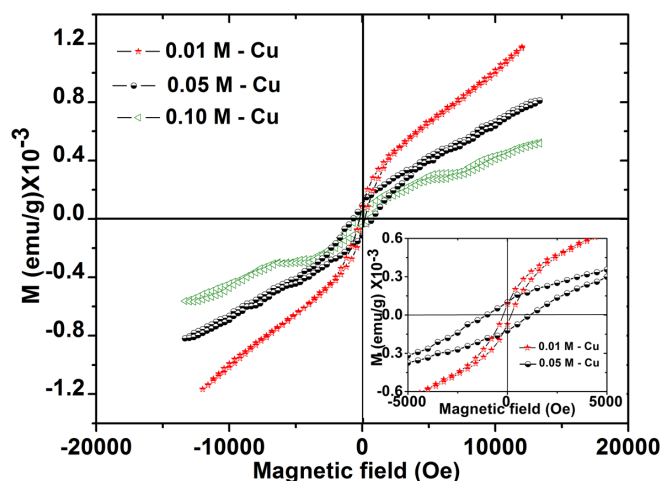


Figure 5.9: Room temperature M-H loop of ZnO:Cu nanostructures. Inset shows the enlarged view near zero field.

Magnetic properties of ZnO:TM nanostructures were investigated using vibrating sample magnetometer (Lakeshore VSM 7410). Figure 5.9-5.11 show the field dependent magnetization (M-H) of the TM doped ZnO nanostructures. The magnetization of the ZnO:Cu nanostructures were first increased with increase of copper doping and at higher doping the room temperature ferromagnetism reduces (fig. 5.9). The Cu doping with 0.05 M $\text{Cu}(\text{CH}_3\text{COO})_2$ in the precursor solution shows a distinguishable hysteresis loop with higher coercive field (900 Oe). The noticeable coercivity of M-H loop could be attributed to strong ferromagnetism at room

temperature. Undoped ZnO nanostructures prepared under same condition shows diamagnetic behavior.

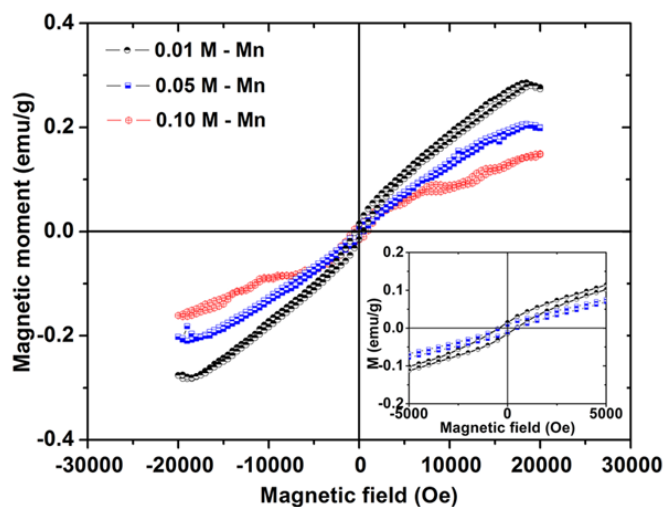


Figure 5.10: Room temperature M-H loop of ZnO:Mn nanostructures. Inset shows the enlarged view near zero field.

The magnetic properties of ZnO:Mn nanostructures are shown in figure 5.10. The magnetization of ZnO:Mn nanostructures decreases with increase of Mn doping. The 0.01 M $\text{Mn}(\text{CH}_3\text{COO})_2$ in the precursor solution shows a distinguishable hysteresis loop with higher coercive field (420 Oe). The noticeable coercivity of M-H loop could be attributed to strong ferromagnetism at room temperature.

The magnetization of the ZnO:Ni nanostructures were first increased with increase of Ni doping and at higher doping the room temperature ferromagnetism reduces (fig.5.11). The Ni doping with 0.05M $\text{Ni}(\text{CH}_3\text{COO})_2$ in the precursor solution shows a distinguishable hysteresis loop with higher

coercive field (500 Oe). The noticeable coercivity of M-H loop could be attributed to strong ferromagnetism at room temperature.

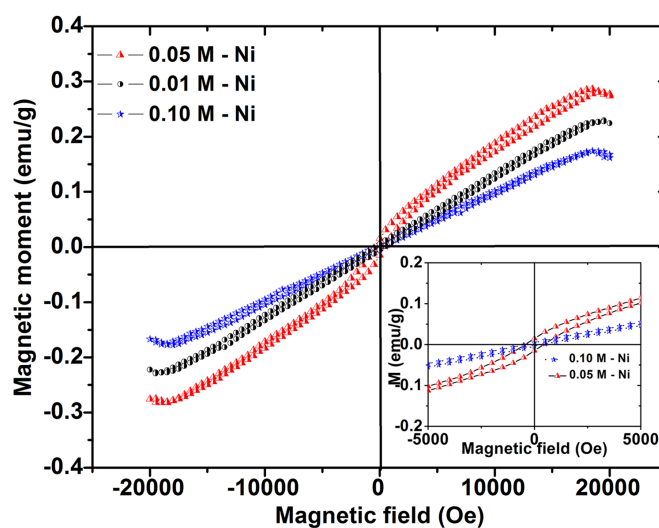


Figure 5.11: Room temperature M-H loop of ZnO:Ni nanostructures. Inset shows the enlarged view near zero field.

The ferromagnetic behavior can be attributed to the presence of small magnetic dipoles located at the surface of nanocrystals, which interacts with the nearest neighbors within the crystal. Consequently, the interchange energy in these magnetic dipoles making other neighboring dipoles oriented in the same direction. In nanocrystals, surface to volume ratio is large, so the population of magnetic dipoles oriented in the same direction will increase at the surface. The interchange energy in the magnetic dipoles making other neighboring dipoles oriented in the same direction and magnetization increases. Thus, the sum of the total amount of dipoles oriented along the same direction will increase subsequently. In short the crystal surface will be usually more magnetically oriented. The enhanced

antiferromagnetic interaction between neighboring TM-TM ions suppress the ferromagnetism at higher doping concentrations.

The room temperature hysteresis loops of ZnO:TM nanostructures were not saturated and it shows that there is some traces of paramagnetism in the prepared samples. The origin of magnetism in DMSs is still controversial; there can be two possible origins of ferromagnetism. The most common mechanism for observed ferromagnetism in ZnO:TM nanostructures is the carrier induced ferromagnetism (RKKY mechanism), often reported for DMSs [217]. The second arises due to secondary phases or clusters. In the present studies the XRD and Raman spectra could not find any cluster formation or secondary phase formation. The broadening and the shift of (101) peaks in the XRD pattern confirms the incorporation of TM ions into the ZnO lattice.

5.4 Conclusion

ZnO and TM (Cu/Ni/Mn)doped ZnO nanostructures were synthesized using hydrothermal method. The effect of concentration of the precursors, temperature and time of growth on the structure, grain size, band gap energy, PL emission and magnetic properties were investigated. The XRD analysis demonstrates that the nanostructures have the hexagonal wurtzite structure and the particle size increases with growth temperature. The orange-red PL emissions observed for the synthesized ZnO nanostructures is due to oxygen vacancy or Zn interstitial defects. The presence of non-polar E_2^{high} and E_2^{low} Raman modes in nanostructures indicates that TM doping doesn't change the wurtzite structure of ZnO. The reduction in

intensity and broadening of Raman mode (E_2^{high}) indicates the incorporation of TM into the ZnO lattice. ZnO:TM nanostructures showed strong ferromagnetic behavior, however at higher doping percentage of TM the ferromagnetic behavior was suppressed. The enhanced antiferromagnetic interaction between neighboring TM-TM ions suppress the ferromagnetism at higher doping concentration.

Chapter 6

Summary and Scope for further study

6.1 Summary of the present study

Dilute Magnetic Semiconductors have wide applications in spintronics due to magnetic and electric properties of the dopants and the host. A large number of research groups synthesize and characterize ZnO and transition metals (TM) doped ZnO thin films and nanostructures by various methods but most of them achieved room temperature ferromagnetism due to impurity phases or metallic clusters. The successful realization of most spintronic applications depend critically on the ability to create spin-polarized charge carriers in a conventional semiconductor in a device structure. This can be accomplished under ambient conditions via optical pumping with appropriately polarized laser light. However ultimate device integration will require electrical spin injection. Electrical spin injection can be accomplished either by injecting from a spin-polarized source or by spin-filtering

unpolarized carriers at the interface. Despite persistent efforts by many groups, spin injection from a conventional ferromagnetic metal into a semiconductor has proved highly inefficient. In contrast, efficient spin injection has recently been successfully demonstrated in all semiconductor tunnel diode structures either by using a spin polarized dilute magnetic semiconductor as the injector or by using a paramagnetic semiconductor under high magnetic field as a spin filter. The most effective measurement of the quality of the oxide-based ferromagnetic materials will be in the operation of device structures, such as spin-FETs. The use of ferromagnetic semiconductors as the injection source in device structures should allow a more direct measurement of the efficiency and length scale of spin transport.

Pulsed Laser Deposition technique is one of the physical methods for the preparation highly oriented compound semiconductors and doped semiconductors. The thin film morphology and optical properties can be tuned by varying the laser fluence and background pressure. The focus of the present study is the growth and characterization of ZnO and transition metal (Co/Mn/Ni/Cu) doped ZnO thin films and nanostructures for optoelectronic and spintronic applications. Highly transparent and crystalline ZnO thin films grown by PLD on different substrates like, quartz, p-Silicon and c-Al₂O₃ were studied. Two major growth parameters; the substrate temperature and the ambient gas pressure were varied and the resulting films were characterized. The effect of deposition parameters on the film structure and the optimized conditions for the growth of ZnO thin films by PLD have been identified. The films have optical transmittance above 80% in the visible region of the spectrum. The surface morphology of the films prepared at higher T_S exhibited almond like structure irrespective of the ablation wavelength. The strong UV-PL emission without defect level

emission confirms the growth of highly stoichiometric and crystalline thin films.

Phase pure $\text{Zn}_{1-x}\text{TM}_x\text{O}$ (TM = Co, Mn, Ni, Cu) thin films were grown by PLD technique. The PLD targets were synthesized by solid state reaction. The structural, morphological, optical and magnetic properties of ZnO:TM thin films were analyzed. XRD pattern revealed that all the TM doped ZnO films have c-axis orientation normal to the substrate. The surface morphology characterized by atomic force microscopy shows that $\text{Zn}_{1-x}\text{TM}_x\text{O}$ films have uniformly placed smaller grains at lower doping percentages and vice versa. The TM doped ZnO films have transmittance greater than 75% in the visible region. The band gap of the ZnO thin films shows red shift with increase of Ni and Cu concentration but it blue shifts with Co and Mn doping. The Cu doped ZnO thin film shows green PL emission at 542 nm and band edge emission at 385 nm. The defect induced Raman active modes in TM doped ZnO thin films and bulk sample is also elucidated. The presence of non-polar E_2^{high} and E_2^{low} Raman modes in thin films indicates that TM doping didnt change the wurtzite structure of ZnO. We obtained room temperature ferromagnetism for lower doping concentrations of TM. These phase pure, highly oriented TM doped ZnO thin films have applications in the field of spintronics.

ZnO and TM (Cu/Mn/Ni)doped ZnO nanostructures were synthesized using hydrothermal method. The effect of concentration of the precursors, temperature and time of growth on the structure, grain size, band gap energy, PL emission and magnetic properties of the nanostructures were investigated. The orange-red PL emissions observed for the synthesized ZnO nanostructures is due to the oxygen vacancy or Zn interstitial defects. The presence of non-polar E_2^{high} and E_2^{low} Raman modes in nanostructures

indicates that TM doping doesn't change the wurtzite structure of ZnO. ZnO:TM nanostructures showed strong ferromagnetic behavior, however at higher doping percentage of TM the ferromagnetic behavior was suppressed.

6.2 Scope for further study

Highly transparent and crystalline ZnO thin films grown by PLD on different substrates; quartz, p-Silicon and c-Al₂O₃ can be used for various optoelectronic applications. The strong UV-PL emission without defect level emission from the highly stoichiometric and crystalline thin films have applications in UV LEDs and UV lasers. The successful realization of spintronics depends critically on the ability to create spin-polarized charge carriers in a conventional semiconductor in a device structure. Single phase Zn_{1-x}TM_xO (TM = Co, Mn, Ni, Cu) thin films grown by PLD technique have wide applications in the field of spin FET, magnetic tunnel junctions etc. The spin injection from a TM doped ZnO layer to pure semiconductors was a long time goal for the ZnO:TM semiconductors. ZnO:TM based heterostructures have been developed to study the spin injection and spin polarized transport mechanism. Spin polarized transport studies in ZnO:TM/ZnO/Zn:TM multi-layer heterostructures fabricated by PLD technique will enlighten the future aspects of the spintronic devices; spin FET, spin tunnel junction, spin filters in information processing devices etc. The combination of photoluminescent and magnetic properties of Zn_{1-x}TM_xO thin films and nanostructures make them attractive candidate for spin light emitting diodes.

Appendix A

Abbreviations used in the thesis

Abbreviation	Expansion
AFM	Atomic Force Microscope
AlN	Aluminum Nitride
BN	Boron Nitride
BR	Blombergen-Rowland
Co	Cobalt
Cu	Copper
CdS	Cadmium Sulphide
CdSe	Cadmium Selenide
CdTe	Cadmium Telluride
CRT	Cathode Ray Tube
CVD	Chemical Vapour Deposition
DMS	Diluted Magnetic Semiconductor
DOS	Density of States
DRS	Diffuse Reflectance Spectroscopy
DSC	Differential scanning calorimetry
EDAX	Energy Dispersive X-ray Spectroscopy
EPR	Electron Paramagnetic Resonance

Abbreviation	Expansion
FED	Field Emission Display
FESEM	Field Emission Scanning Electron Microscope
FET	Field Effect Transistor
FM	Ferromagnetism
FWHM	Full Width at Half Maximum
GaAs	Gallium Arsenide
GaAsP	Gallium Arsenide Phosphide
GaInP	Gallium Indium Phosphide
GaN	Gallium Nitride
GaP	Gallium Phosphide
GMR	Giant Magneto-resistance
GPa	Giga Pascal
hcp	hexagonal-close-packed
HVPE	hydride vapor phase epitaxy
ICSD	Inorganic Crystal Structure Database
InAs	Indium Arsenide
KrF	Krypton Fluoride
LED	Light Emitting Diode
LO	Longitudinal Optical
LP-PLA	Liquid Phase Pulsed Laser Ablation
LVDT	Linear Variable Differential Transformer
MBE	Molecular Beam Epitaxy
MIS	Metal Insulator Semiconductor
Mn	Manganese
MOCVD	Metal Organic Chemical Vapour Deposition
NaCl	Sodium Chloride
NBE	Near Band Energy
Nd:YAG	Neodymium Yttrium Aluminium Garnet
Ni	Nickel
nm	nanometer
PECVD	Plasma Enhanced Chemical Vapour Deposition
PID	Proportional Integral Derivative
PL	Photoluminescence
PLD	Pulsed Laser Deposition

Abbreviation	Expansion
PO ₂	Oxygen partial pressure
PVD	Physical Vapor Deposition
rf	Radio Frequency
RKKY	Ruderman-Kittel-Kasuya-Yosida
RT	Room Temperature
RTFM	Room Temperature Ferromagnetism
RTPL	Room Temperature Photoluminescence
SEM	Scanning Electron Microscopic
SiC	Silicon Carbide
SP	Superparamagnetic
SPM	Scanning Probe Microscope
STM	Scanning Tunneling Microscope
SQUID	Superconducting Quantum Interference Device
T _c	Curie temperature
TM	Transition metals
TO	Transverse Optical
T _S	Substrate temperature
UV	Ultraviolet
XPS	X-ray Photoelectron Spectroscopy
XRD	X-ray Diffraction
ZnCdO	Zinc Cadmium Oxide
Zn _{1-x} Co _x O	Zinc Cobalt Oxide
Zn _{1-x} Cu _x O	Zinc Copper Oxide
Zn _{1-x} Mn _x O	Zinc Manganese Oxide
ZnMgO	Zinc Magnesium Oxide
ZnMnO	Zinc Manganese Oxide
Zn _{1-x} Ni _x O	Zinc Nickel Oxide
ZnO	Zinc Oxide
ZnS	Zinc Sulfide
ZnSe	Zinc Selenide
ZnTe	Zinc Telluride

Bibliography

- [1] N. W. Emanetoglu, J. Zhu, Y. Chen, J. Zhong, Y. Chen and Y. Lu, *Appl. Phys. Lett.* **85** (2004) 3702.
- [2] D. P. Norton, Y. W. Heo, M. P. Ivill, K. Ip, S. J. Pearton, M. F. Chisholm and T. Steiner, *Materials Today* **7** (2004) 34.
- [3] T. Aoki, Y. Hatanaka and D. C. Look, *Appl. Phys. Lett.* **76** (2000) 3257.
- [4] P. Verardi, N. Nastase, C. Gherasim, C. Ghica, M. Dinescu, R. Dinu and C. Flueraru, *J. Cryst. Growth* **197** (1999) 523.
- [5] E. Fortunato, P. Nunes, A. Marques, D. Costa, H. Aguas, I. Ferreira, M. E. V. Costa, M. H. Godinho, P. L. Almeida, J. P. Borges and R. Martins, *Gold Bull.* **33** (2000) 103.
- [6] T. Dietl, H. Ohno and F. Matsukura, *Science* **287** (2000) 1019.
- [7] M. P. Maruska and J. J. Tietjen, *Appl. Phys. Lett.* **15** (1969) 327.
- [8] J. I. Pankove, E. A. Miller and J. E. Berkeyheiser, *RCA Rev.* **32** (1971) 383.

- [9] H. Ohta, K. Kawamura, M. Ovita, N. Sarukura, M. Hirano and H. Hosono, *Materials Research Society Symposia Proceedings* **623** (2000) 283.
- [10] S. Flickyngerova, K. Shtereva, V. Stenova, D. Hasko, I. Novotny, V. Tvarozek, P. Sutta and E. Vavrinsky, *Appl. Surf. Sci.* **254** (2008) 3643.
- [11] Y. Nakata, T. Okada and M. Maeda, *Appl. Surf. Sci.* **197** (2002) 368.
- [12] B. Kong, S. Mohanta, D. Kim and H. Cho, *Physica B: Condensed Matter* **401** (2007) 399.
- [13] Ü. Özgür, Y. I. Alivov, C. Liu, A. Teke, M. A. Reshchikov, S. Dogan, V. Avrutin, S. J. Cho and H. Morko, *J. Appl. Phys.* **98** (2005) 041301.
- [14] D. Li, Y. H. Leung, A. B. Djuriiæ, Z. T. Liu, M. H. Xie, S. L. Shi and S. J. Xu, *Appl. Phys. Lett.* **85** (2004) 1601.
- [15] I. Zutic, J. Fabian and S. D. Sarma, *Rev. Mod. Phys.* **76** (2004) 323.
- [16] M. J. Calderon and S. D. Sarma, *Annals of Physics* **322** (2007) 2618.
- [17] S. D. Sarma, *American Scientist* **89** (2001) 516.
- [18] P. Wisniewski, *Appl. Phys. Lett.* **90** (2007) 192106.
- [19] N. Ashkenov, B. N. Mbenkum, C. Bundesmann, V. Riede, M. Lorenz, D. Spemann, E. M. Kaidasev, A. Kasic, M. Schubert, M. Grundmann, G. Wagner, H. Neumann, V. Darakchieva, H. Arwin and B. Monema, *J. Appl. Phys.* **93** (2003) 126.

- [20] S. Singh, P. Thiyagarajan, K. M. Kant, D. Anita, S. Thirupathiah, N. Rama, B. Tiwari, M. Kottaisamy and M. S. R. Rao, *J. Phys. D: Appl. Phys.* **40** (2007) 6312.
- [21] H. Morkoç and Ü. Özgür, *Zinc Oxide Fundamentals, Materials and Device Technology*, Wiley-VCH Verlag GmbH & Co. KGaA, Weinheim (2009).
- [22] C. Klingshirnr, *Semiconductor Optics*, Springer-Berlag Berlin, Heridelberg (1997).
- [23] S. B. Ogale, *Thinfilms and Heterostructures for Oxide Electronics*, Springer, USA (2005).
- [24] A. Gulino, F. Castelli, P. Rossi and I. Fragala, *Chem. Mater.* **12** (200) 548.
- [25] J. Jin, S. Im and S. Y. Le, *Thin Solid Films* **366** (2000) 107.
- [26] Y. R. Ryu, S. Zhu, J. D. Budai, H. R. Chandrasekhar, P. F. Miceli and H. W. White, *J. Appl. Phys.* **88** (2000) 201.
- [27] K. K. Kim, J. H. Song, H. J. Jung and S. J. Park, *J. Appl. Phys.* **87** (2000) 3573.
- [28] M. Tanaka, *J. Vac. Sci. Technol. B* **16** (1998) 2267.
- [29] A. Ohtomo, M. Kawasaki, T. Koida, K. Masubuchi, H. Koinuma, Y. Sakurai, Y. Yoshida and Y. Segawa, *Appl. Phys. Lett.* **72** (1998) 2466.
- [30] F. Matsukura, H. Ohno, A. Schen and Y. Sugawara, *Phys. Rev. B* **57** (1998) R2037.

- [31] H. Ohno, *Science* **281** (1998) 951.
- [32] S. J. Pearton, C. R. Abernathy, D. P. Norton, A. F. Hebard, Y. D. Park, L. A. Boatner and J. D. Budai, *Mater. Sci. Eng. R* **40** (2003) 137.
- [33] F. Pan, C. Song, X. J. Liu, Y. C. Yang and F. Zeng, *Mater. Sci. Eng. R* **62** (2008) 1.
- [34] S. A. Wolf, D. D. Awschalom, R. A. Buhrman, J. M. Daughton, S. von Molnar, M. L. Roukes, A. Y. Chtchelkanova and D. M. Treger, *Science* **294** (2001) 1488.
- [35] B. D. Cullity and C. D. Graham, *Introduction to Magnetic Materials*, IEEE Press, Wiley - A John Wiley & Sons Inc. Publications, New Jersey (2009).
- [36] S. Blundell, *Magnetism in Condensed Matter*, Oxford University Press, New York (2001).
- [37] D. Sellmyer and R. Skomski, *Advanced Magnetic Nanostructures*, Springer, New York (2006).
- [38] K. Sato and H. K. Yoshida, *Jpn. J. Appl. Phys.* **40** (2001) L334.
- [39] H. K. Yoshida and K. Sato, *Physica B* **327** (2003) 337.
- [40] P. Sharma, A. Gupta, K. V. Rao, F. J. Owens, R. Sharma, R. Ahuja, J. M. O. Guillen, B. Johansson and G. A. Gehring, *Nature. Mater.* **2** (2003) 673.

- [41] A. K. Pradha, K. Zhang and S. Mohanty, *Appl. Phys. Lett.* **86** (2005) 152511.
- [42] Y. Q. Chang, D. B. Wang and X. H. Luo, *Appl. Phys. Lett.* **83** (2002) 4020.
- [43] T. Fukumura, Z. W. Jin and M. Kawasak, *Appl. Phys. Lett.* **78** (2001) 958.
- [44] S. S. Kim, J. H. Moon, B. T. Lee, O. S. Song and J. H. Je, *J. Appl. Phys.* **95** (2004) 454.
- [45] T. Fukumura, C. Jin, A. Ohtomo, H. Koinuma and M. Kawasaki, *Appl. Phys. Lett.* **75** (1999) 3366.
- [46] K. Ueda, H. Tabata and T. Kawai, *Appl. Phys. Lett.* **79** (2001) 988.
- [47] K. Sato and H. K. Yoshida, *J. Appl. Phys.* **39** (2000) L555.
- [48] J. H. Kim, H. Kim, D. Kim, Y. E. Ihm and W. K. Choo, *J. Appl. Phys.* **92** (2002) 6066.
- [49] T. Wakano, N. Fujimura, Y. Morinaga, N. Abe and T. Ito, *Physica E* **10**(2001) 260.
- [50] Z. G. Yin, N. Chen, F. Yang, S. L. Song, C. L. Chai, J. Zhong, H. J. Qian and K. Ibrahim, *Solid State Commun.* **135** (2005) 430.
- [51] S. W. Jung, W. I. Park, G. C. Yi and M. Kim, *Adv. Mater.* **15** (2003) 1358.
- [52] M. Venkatesan, C. B. Fitzgerald, J. G. Lunney and J. M. D. Coey, *Phys. Rev. Lett.* **93** (2004) 177206.

- [53] S. W. Jung, S. J. An, G. C. Yi, C. U. Jung, S. I. Lee and S. Cho, *Appl. Phys. Lett.* **80** (2002) 4561.
- [54] D. P. Norton, S. J. Pearton, A. F. Hebard, N. Theodoropoulou, L. A. Boatner and R. G. Wilson, *Appl. Phys. Lett.* **82** (2003) 239.
- [55] D. P. Norton, M. E. Overberg, S. J. Pearton and K. Preusser, *Appl. Phys. Lett.* **83** (2003) 5488.
- [56] D. Chakraborti, J. Narayan and J. T. Prater, *Appl. Phys. Lett.* **90** (2007) 062504.
- [57] Z. Jin, T. Fukumura, M. Kawasaki, K. Ando, H. Saito, Y. Z. Yoo, M. Murakami, Y. Matsumoto, T. Hasegawa and H. Koinuma *Appl. Phys. Lett.* **78** (2001) 3824.
- [58] D. B. Buchholz, R. P. H. Chang, J. H. Song and J. B. Ketterson, *Appl. Phys. Lett.* **87** (2005) 082504.
- [59] J. D. Ye, S. L. Gu, F. Qin, S. M. Zhu, S. M. Liu, X. Zhou, W. Liu, L. Q. Hu, R. Zhang, Y. Shi, Y. D. Zheng and Y. D. Ye, *Appl. Phys. A* **81** (2005) 809.
- [60] S. J. Pearton, C. R. Abernathy, M. E. Overberg, G. T. Thaler, D. P. Norton, N. Theodoropoulou, A. F. Hebard, Y. D. Park, F. Ren, J. Kim and L. A. Boatner, *J. Appl. Phys.* **93** (2003) 1.
- [61] G. A. Prinz, *Science* **282** (1998) 1660.
- [62] D. Chiba, M. Yamanouchi, F. Matsukura and H. Ohno, *Science* **301** (2003) 943.

- [63] Y. Matsumoto, M. Murakami, T. Shono, T. Hasegawa, T. Fukumura, M. Kawasaki, P. Ahmet, T. Chikyow, S. Koshihara and H. Koinuma, *Science* **291** (2001) 854.
- [64] S. H. Bae, S. Y. Lee, B. J. Jin and S. Im, *Appl. Surf. Sci.* **154** (2000) 458.
- [65] T. Nagase, T. Ooie, Y. Nakatsuka, K. Shinozaki and N. Mizutani, *Jpn. J. Appl. Phys.* **39** (2000) L713.
- [66] K. Iwata, P. Fons, S. Niki, A. Yamada, K. Matsubara, K. Nakahara and H. Takasu, *Phys. Stat. Sol. A* **180** (2000) 287.
- [67] K. Byrappa, I. Yoshimura and M. Yoshimura, *Handbook of Hydrothermal Technology*, William Andrew Publishing, New York (2001).
- [68] K. Byrappa and T. Adschiri, *Progress in Crystal Growth and Characterization of Materials* **53** (2007) 117.
- [69] B. D. Cullity and S. R. Stock, *Elements of X-ray diffraction*, Prentice Hall, New Jersey, 3 edition (2001).
- [70] C. Kittel, *Introduction to Solid State Physics*, Wiley Eastern Ltd (1996).
- [71] D. K. Schroder, *Semiconductor material and device characterization*, A Wiley-interscience publication (1998).
- [72] C. N. Banwell, *Fundamental of Molecular spectroscopy*, Tata McGraw-Hill Education, New Jersey (1994).
- [73] A. Tanaka, S. Onari and T. Arai, *Phys. Rev. B* **47** (1993) 1237.

- [74] A. Tanaka, S. Onari and T. Arai, *Phys. Rev. B* **45** (1992) 6587.
- [75] J. Bardeen and F. J. Blatt and L. H. Hall, *Proc. of Photoconductivity Conf.*, J. Wiley and Sons, Atlantic city (1954).
- [76] K. Gramm, L. Lundgren and Beckman, *Physica Scripta*. **13** (1976) 93.
- [77] C. V. Raman and K. S. Krishna, *Nature* **121** (1928) 501.
- [78] M. Rajalakshmi, T. Sakunthala and A. K. Arora, *J. Phys.: Condens. Matter*. **9** (1997) 9745.
- [79] Y. F. Chen, D. M. Bagnall, H. J. Koh, K. T. Park, K. J. Hiraga, Z. Q. Zhu and T. F. Yao, *J. Appl. Phys.* **84** (1998) 3912.
- [80] R. F. Service, *Science* **276** (1997) 895.
- [81] D. M. Bagnall, Y. F. Chen, Z. Zhu, T. Yao, S. Koyama, M. Y. Shen and T. Goto, *Appl. Phys. Lett.* **70** (1997) 2230.
- [82] C. Li, G. Fang, F. Su, G. Li, X. Wu and X. Zhao, *Nanotechnology* **17** (2006) 3740.
- [83] H. Y. Yang, S. P. Lau, S. F. Yu, A. P. Abiyasa, M. Tanemura, T. Okita and H. Hatano, *Appl. Phys. Lett.* **89** (2006) 011103.
- [84] X. P. Gao, C. S. Lao, W. L. Hughes and Z. L. Wang, *Chem. Phys. Lett.* **408** (2005) 174.
- [85] V. Craciun, S. Amirhaghi, D. Craciun, J. Elders, J. G. E. Gardeniers and I. W. Boyd, *Appl. Surf. Sci.* **86** (1995) 99.
- [86] X. W. Sun and H. S. Kwok, *J. Appl. Phys.* **86** (1999) 408.

- [87] D. C. Look, D. C. Reynolds, C. W. Litton, R. L. Jones, D. B. Eason and G. Cantwell, *Appl. Phys. Lett.* **81** (2002) 1830.
- [88] R. S. Ajimsha, R. Manoj, P. M. Aneesh and M. K. Jayaraj, *Curent. Appl. Phys.* **10** (2010) 693.
- [89] W. Zhaoyang, H. Lizhong, Z. Jie, S. Jie and W. Zhijun, *Vacuum* **78** (2005) 53.
- [90] E. S. Shim, H. S. Kang, J. S. Kang, J. H. Kim and S. Y. Lee, *Appl. Surf. Sci.* **186** (2002) 474.
- [91] N. Cherief, D. Givord, A. Lienard, K. Mackay, O. F. K. McGrath, J. P. Rebouillat, F. Robaut and Y. Souche, *J. Magn. Magn. Mater.* **121** (1993) 94.
- [92] N. Fujimura, T. Nishihara, S. Goto, J. Xu and T. Ito, *J. Cryst. Growth* **130** (1993) 269.
- [93] J. L. Zhao, X. M. Li, J. M. Bian, W. D. Yu and X. D. Gao, *J. Cryst. Growth* **276** (2005) 507.
- [94] S. Im, B. J. Jin and S. Yi, *J. Appl. Phys.* **87** (2000) 4558.
- [95] A. Mitra, R. K. Thareja, V. Ganesan, A. Gupta, P. K. Sahoo and V. N. Kulkarni, *Appl. Surf. Sci.* **174** (2001) 232.
- [96] X. M. Fan, J. S. Lian, Z. X. Guo and H. J. Lu, *Appl. Surf. Sci.* **239** (2005) 176.
- [97] J. Zhao, L. Hu, Z. Wang, Z. Wang, H. Zhang, Y. Zhao and X. Liang, *J. Cryst. Growth* **280** (2005) 455.

- [98] W. Zhaoyang, S. Liyuan and H. Lizhong, *Vacuum* **85** (2010) 397.
- [99] A. Sarkar, S. Ghosh, S. Chaudhuri and A. K. Pal, *Thin Solid Films* **204** (1991) 255.
- [100] S. A. Studeninkin, N. Golego and M. Cocivera, *J. Appl. Phys.* **84** (1998) 2287.
- [101] B. J. Jin and S. H. Bae, *Mater. Sci. Eng. B* **71** (2000) 301.
- [102] F. K. Shan, B. C. Shin, S. W. Jang and Y. S. Yu, *J. Eur. Ceram. Soc.* **24** (2004) 1015.
- [103] T. C. Damen, S. P. S. Porto and B. Tell, *Phys. Rev.* **142** (1966) 570.
- [104] K. A. Alim, V. A. Fonoberov, M. Shamsa and A. A. Balandin, *J. Appl. Phys.* **97** (2005) 124313.
- [105] F. K. Shan, G. X. Liu, W. J. Lee, G. H. Lee, I. S. Kim, B. C. Shina and Y. C. Kim, *J. Cryst. Growth* **277** (2005) 284.
- [106] J. K. Furdyna, *J. Appl. Phys.* **64** (1988) R29.
- [107] A. H. Macdonald, P. Schiffer and N. Samarth, *Nat. Mater.* **4** (2005) 195.
- [108] H. Ohno, A. Shen, F. Matsukura, A. Oiwa, A. Endo, S. Katsumoto and Y. Iye, *Appl. Phys. Lett.* **69** (1996) 363.
- [109] T. Jungwirth, J. Sinova, J. Masek, J. Kucera and A. H. MacDonld, *Rev. Mod. Phys.* **78** (2006) 809.
- [110] S. von Molnár and D. Read, *J. Magn. Magn. Mater.* **242** (2002) 13.

- [111] S. A. Chambers, *Surf. Sci. Rep.* **61** (2006) 345.
- [112] S. J. Pearton, D. P. Norton, K. Ip, Y. W. Heo and T. Steiner, *Superlatt. Microstruct.* **32** (2003) 343.
- [113] I. Sakaguchi, S. Hishita and H. Haneda, *Appl. Surf. Sci.* **237** (2004) 358.
- [114] H. Zhu, J. Iqbal, H. Xu and D. Yu, *J. Chem. Phys.* **129** (2008) 124713.
- [115] T. Ghosh, M. Dutta, S. Mridha and D. Basak, *J. Electrochem. Soc.* **156** (2009) H285.
- [116] L. Ma, S. Ma, H. Chen, X. Ai and X. Huang, *Appl. Surf. Sci.* **257** (2011) 10036.
- [117] K. Samanta, A. K. Arora and R. S. Katiyar, *J. Appl. Phys.* **110** (2011) 043523.
- [118] J. Serrano, F. J. Manjon, A. H. Romero, A. Ivanov, M. Cardona, R. Lauck, A. Bosak and M. Krisch, *Phys. Rev. B* **81** (2010) 174304.
- [119] P. Singh, A. Kaushal and D. Kaur, *J. Alloy. Compnd.* **11** (2009) 471.
- [120] J. Wang, W. Chen and M. Wang, *J. Alloy. Compnd* **44** (2008) 449.
- [121] A. Dinia, G. Schmerber, V. P. Bohnes, C. Mény, P. Panissod and E. Beaurepaire, *J. Magn. Magn. Mater.* **286** (2005) 37.
- [122] H. J. Lee, S. Y. Jeong, C. R. Cho and C. H. Park, *Appl. Phys. Lett.* **81** (2001) 21.

- [123] Y. Z. Peng, T. Liew, W. D. Song, C. W. An, K. L. Teo and T. C. Chong, *J. Supercond.* **18** (2005) 97.
- [124] D. C. Kundaliya, S. B. Ogale and S. E. Lofland, *Nat. Mater.* **3** (2004) 709.
- [125] K. J. Kim and Y. R. Park, *Appl. Phys. Lett.* **81** (2002) 1420.
- [126] I. Ozerov, F. Chabre and W. Marine, *Mater. Sci. Eng. C* **25** (2005) 614.
- [127] M. Opel, K. W. Nielsen, S. Bauer, S. T. B. Goennenwein, J. C. Cezar, D. Schmeisser, J. Simon, W. Mader and R. Gross, *Eur. Phys. J. B* **63** (2008) 437.
- [128] R. P. Wang, G. Xu and P. Jin, *Phys. Rev. B* **69** (2004) 113303.
- [129] Y. M. Hu, C. Y. Wang, S. S. Lee, T. C. Han and W. Y. Chou, *Thin Solid Films* **519** (2010) 1272.
- [130] T. L. Phan, R. Vincent, D. Cherns, N. H. Dan and S. C. Yu, *Appl. Phys. Lett.* **93** (2008) 082110.
- [131] M. Ivill, S. J. Pearton, S. Rawal, L. Leu, P. Sadik, R. Das, A. F. Hebard, M. Chisholm, J. D. Budai and D. P. Norton, *N. J. Phys.* **10** (2008) 065002.
- [132] J. G. Ma, Y. C. Liu, R. Mu, J. Y. Zhang, Y. M. Lu, D. Z. Shen and X. W. Fan, *J. Vacuum. Sci. Tech. B* **22** (2004) 94.
- [133] Z. B. Gu, C. S. Yuan, M. H. Lu, J. Wang, D. Wu, S. T. Zhang, S. N. Zhu, Y. Y. Zhu and Y. F. Chen, *J. Appl. Phys.* **98** (2005) 053908.

- [134] P. Koidl, *Phys. Rev. B* **15** (1977) 2493.
- [135] S. Ramachandran, A. Tiwari and J. Narayan, *Appl. Phys. Lett.* **84** (2004) 5255.
- [136] G. G. Rusu, P. Gorley, C. Baban, A. P. Ramu and M. Rusu, *J. Opto. Adv. Mater.* **12** (2010) 895.
- [137] Y. C. Kong, D. P. Yu, B. Zhang and S. Q. F. Feng, *Appl. Phys. Lett.* **78** (2001) 407.
- [138] V. A. L. Roy, A. B. Djuri Sic, H. Liu, X. X. Zhang, Y. H. Leung, M. H. Xie, J. Gao, H. F. Lui and C. Surya, *Appl. Phys. Lett.* **84** (2004) 756.
- [139] H. J. Ko, Y. F. Chen, Z. Zhu, T. Hanada and T. Yao, *J. Cryst. Grow.* **208** (2000) 389.
- [140] H. Richter, Z. P. Wang and L. Ley, *Solid State Commu.* **39** (1981) 625.
- [141] M. S. Arnold, P. Avouris, Z. W. Pan and Z. L. Wang, *J. Phys. Chem. B* **107** (2003) 6599.
- [142] S. P. S. Porto and R. S. Krishnan, *J. Chem. Phys.* **47** (1967) 1009.
- [143] Y. M. Hu, C. Y. Wang, S. S. Lee, T. C. Han, W. Y. Choub and G. J. Chen, *J. Raman Spectroscopy* **42** (2011) 434.
- [144] F. J. Manjn, B. Mari, J. Serrano and A. H. Romero, *J. Appl. Phys.* **97** (2005) 053516.

- [145] X. B. Wang, C. Song, K. W. Geng, F. Zeng and F. Pan, *Appl. Surf. Sci.* **253** (2007) 6905.
- [146] J. F. Scott, *Phys. Rev. B* **2** (1970) 1209.
- [147] R. H. Kodama, S. A. Makhlof and A. E. Berkowitz, *Phys. Rev. Lett.* **79** (1997) 1393.
- [148] R. K. Singhal, M. Dhawan, S. Kumar, S. N. Dolia, Y. T. Xing and E. Saitovitch, *Physica B* **404** (2009) 3275.
- [149] P. Sharma, A. Gupta, F. J. Owensc, A. Inoued and K. V. Rao, *J. Magn. Magn. Mater.* **282** (2004) 115.
- [150] K. Potzger and S. Zhou, *Phys. Stat. Soli. B* **246** (2009) 1147.
- [151] ICSD. Number 086254
- [152] B. B. Li, X. Q. Xiua, R. Zhang, Z. K. Tao, L. Chen, Z. L. Xie, Y. D. Zheng and Z. Xie, *Mater. Sci. Semi. Proc.* **9** (2006) 141.
- [153] T. L. Barr, M. Yin and S. Varma, *J. Vac. Sci. Technol. A* **10** (1992) 2383.
- [154] Y. R. Jang, K. H. Yoo and S. M. Park, *J. Mater. Sci. Technol.* **26** (2010) 973.
- [155] B. Pandey, S. Ghosh, P. Srivastava, D. Kabiraj, T. Shripati and N. P. Lalla, *Physica E* **41** (2009) 1164.
- [156] K. T. Kim, G. H. Kim, J. C. Woo and C. I. Kim, *Surf. Coatng. Tech.* **202** (2008) 5650.

- [157] Y. Z. Yoo, *J. Appl. Phys.* **90** (2001) 4246.
- [158] S. V. Bhat and F. L. Deepak, *Solid State Commun.* **135** (2005) 345.
- [159] D. A. Schwartz, N. S. Norberg, Q. P. Nguyen, J. M. Parker and D. R. Gamelin, *J. Am. Chem. Soc.* **125** (2003) 13205.
- [160] K. Ando, H. Saito, Z. Jin, T. Fukumura, M. Kawasaki, Y. Matsumoto and H. Koinuma, *J. Appl. Phys.* **89** (2001) 7284.
- [161] J. Diouri, J. P. Lascaray and M. El Amrani, *Phys. Rev. B* **31** (1985) 7995.
- [162] C. Cheng, G. Xu, H. Zhang and Y. Luo, *Mater. Lett.* **62** (2008) 1617.
- [163] Y. R. Lee, A. K. Ramdas and R. L. Aggarwal, *Phys. Rev. B* **38** (1988) 10600.
- [164] R. Dingle, *Phys. Rev. Lett.* **23** (1969) 579.
- [165] F. H. Su, *J. Appl. Phys.* **100** (2006) 013107.
- [166] P. Dahan, V. Fleurov, P. Thurian, R. Heitz, A. Hoffmann and I. Broser, *Phys. Rev. B* **57** (1998) 9690.
- [167] P. K. Sharma, R. K. Dutta and A. C. Pandey, *J. Magn. Magn. Mater.* **321** (2009) 3457.
- [168] P. Parayanthal and F. H. Pollak, *Phys. Rev. Lett.* **52** (1984) 1822.
- [169] E. K. Koh, Y. J. Park, E. K. Kim, S. K. Min and S. H. Choh, *Phys. Rev. B* **57** (1998) 11919.
- [170] M. S. Park and B. I. Min, *Phys. Rev. B* **68** (2003) 224436.

- [171] Y. Gyu-Chul, W. Chunrui and P. Won Il, *Semicond. Sci. Technol.* **20** (2005) S22.
- [172] Z. Qiuxiang, Y. Ke, B. Wei, W. Qingyan, X. Feng, Z. Ziqiang, D. Ning and S. Yan, *Mater. Lett.* **61** (2007) 3890.
- [173] L. Yuzhen, G. Lin, X. Huibin, D. Lu, Y. Chunlei, W. Jiannong, G. Weikun, Y. Shihe and W. Ziyu, *J. Appl. Phys.* **99** (2006) 114302.
- [174] A. Hachigo, H. Nakahata, K. Higaki, S. Fujii and S. I. Shikata, *Appl. Phys. Lett.* **65** (1994) 2556.
- [175] H. Morkoc, S. Strite, G. B. Gao, M. E. Lin and B. Sverdlov and M. Burns, *J. Appl. Phys.* **76** (1994) 1363.
- [176] L. Spanhel and M. A. Anderson, *J. Am. Chem. Soc.* **113** (1991) 2826.
- [177] D. M. Bagnall, Y. F. Chen, M. Y. Shen, Z. Zhu, T. Goto and T. Yao, *J. Cryst. Growth.* **184** (1998) 605.
- [178] A. N. Andriotis and M. Menon, *Phys. Stat. Sol. B* **248** (2011) 2032.
- [179] G. Pei, C. Xia, S. Cao, J. Zhang, F. Wu and J. Xu, *J. Magn. Magn. Mater.* **302** (2006) 340.
- [180] Q. P. Zhong and E. Matijevic, *J. Mater. Chem.* **3** (1996) 443.
- [181] W. Lingna and M. Mamoun, *J. Mater. Chem.* **9** (1999) 2871.
- [182] D. W. Bahnemann, C. Kormann and M. R. Hoffmann, *J. Phys. Chem.* **91** (1987) 3789.

- [183] Z. Hui, Y. Deren, M. Xiangyang, J. Yujie, X. Jin and Q. Duanlin, *Nanotechnology* **15** (2004) 622.
- [184] J. Zhang, L. D. Sun, J. L. Yin, H. L. Su, C. S. Liao and C. H. Yan, *J. Mater. Sci. Lett.* **14** (2002) 4172.
- [185] W. J. Li, E. W. Shi, Y. Q. Zheng and Z. W. Yin, *J. Mater. Sci. Lett.* **20** (2001) 1381.
- [186] C. Y. Lee, T. Y. Tseng, S. Y. Li and P. Lin, *J. Appl. Phys.* **99** (2006) 024303.
- [187] S. Guo, Z. Du and S. Dai, *Phys. Stat. Sol. B* **246** (2009) 2329.
- [188] Z. X. Cheng, X. L. Wang, S. X. Dou, K. Ozawa, H. Kimura and P. Munroe, *J. Phys. D: Appl. Phys.* **40** (2007) 6518.
- [189] A. O. Ankiewicz, W. Gehlhoff, J. S. Martins, S. Pereira, S. Pereira, A. Hoffmann, E. M. Kaidashev, A. Rahm, M. Lorenz, M. Grundmann, M. C. Carmo, T. Trindade and N. A. Sobolev, *Phys. Stat. Sol. B* **246** (2009) 766.
- [190] Q. Ahsanulhaq, A. Umar and Y. B. Hahn, *Nanotechnology* **18** (2007) 115603.
- [191] M. Xiangyang, Z. Hui, J. Yujie, X. Jin and Y. Deren, *Mater. Lett.* **59** (2005) 3393.
- [192] A. I. Y. Tok, F. Y. C. Boey, S. W. Du and B. K. Wong, *Mater. Sci. Eng. B* **130** (2006) 114.

- [193] R. Viswanatha, S. Chakraborty, S. Basu and D. D. Sarma, *Phys. Chem. B* **110** (2006) 22310.
- [194] G. Clavel, N. Pinna and D. Zitoun, *Phys. Stat. Sol. A* **204** (2007) 118.
- [195] R. B. Bylsma, W. M. Becker, J. Kossut and U. Debska, *Phys. Rev. B* **33** (1986) 8207.
- [196] D. R. Gamelin, *J. Am. Chem. Soc.* **124** (2002) 15192.
- [197] P. V. Radovanovic and D. R. Gamelin, *Phys. Rev. Lett.* **91** (2003) 157202.
- [198] R. Elilarassi and G. Chandrasekaran, *J. Mater. Sci: Mater. Electron.* **22** (2011) 751.
- [199] H. Weakliem, *J. Chem. Phys.* **36** (1962) 2117.
- [200] L. Dai, X. L. Chen, W. J. Wang, T. Zhou and B. Q. Hu, *J. Phys. Condens. Matter.* **15** (2003) 2221.
- [201] H. Wang, H. B. Wang, F. J. Yang, Y. Chen, C. Zhang, C. P. Yang, Q. Li and S. P. Wong, *Nanotechnology* **17** (2006) 4312.
- [202] M. H. Huang, S. Mao, H. Feick, H. Yan, Y. Wu, H. Kind, E. Weber, R. Russo and P. Yang, *Science* **292** (2001) 1897.
- [203] X. Q. Meng, D. Z. Shen, J. Y. Zhang, D. X. Zhao, Y. M. Lu, L. Dong, Z. Z. Zhang, Y. C. Liu and X. W. Fan, *Solid State Commun.* **135** (2005) 179.

- [204] X. Liu, X. Wu, H. Cao and R. P. H. Chang, *J. Appl. Phys.* **95** (2004) 3141.
- [205] L. E. Greene, M. Law, J. Goldberger, F. Kim, J. C. Johnson, Y. Zhang, R. J. Saykally and P. Yang, *Angew. Chem.* **115** (2003) 3030.
- [206] N. Y. Garces, L. Wang, L. Bai, N. C. Giles, L. E. Halliburton and G. Cantwell, *Appl. Phys. Lett.* **81** (2002) 622.
- [207] H. J. Fan, R. Scholz, F. M. Kolb, M. Zacharias, *Appl. Phys. Lett.* **85** (2004) 4142.
- [208] H. J. Fan, R. Scholz, F. M. Kolb, M. Zacharias, U. Gcsele, F. Heyroth, C. Eisenschmidt, T. Hempel and J. Christen, *Appl. Phys. A* **79** (2004) 1895.
- [209] B. Lin, Z. Fu and Y. Jia, *Appl. Phys. Lett.* **79** (2001) 943.
- [210] Y. F. Mei, G. G. Siu, R. K. Y. Fu, K. W. Wong, P. K. Chu, C. W. Lai and H. C. Ong, *Nucl. Instrum. Methods Phys. Res. B* **237** (2005) 307.
- [211] L. Wu, Y. Wu, X. Pan and F. Kong, *Opt. Mater.* **28** (2006) 418.
- [212] Y. S. Wang, P. J. Thomas and P. OBrien, *J. Phys. Chem. B* **110** (2006) 21412.
- [213] Z. Wang, H. Zhang, L. Zhang, J. Yang, S. Yan and C. Wang, *Nanotechnology* **14** (2003) 11.
- [214] M. Koyano, P. Q. Bao, L. T. ThanhBinh, H. L. Hong, N. N. Long and S. I. Katayama, *Phys. Stat. Sol. A* **193** (2002) 125.

- [215] A. Chartier, P. D. Arco, R. Dovesi and V. R. Saunders, *Phys. Rev. B* **60** (1999) 14042.
- [216] F. J. Manjón, K. Syassen and R. Lauck, *High Press. Res.* **22** (2002) 299.
- [217] S. Koshihara, A. Oiwa, M. Hirasawa, S. Katsumoto, Y. Iye, C. Urano, H. Takagi, H. Munekata, *Phys. Rev. Lett.* **78** (1997) 4617.